University of Twente
Enschede - The Netherlands

MESA+
Institute for Nanotechnology

Development of Gadolinia Doped Ceria Electrolyte for IT-SOFC

University of Twente
Faculty of Science and Technology
Department of Chemical Engineering
Group of Inorganic Materials Science

Master of Science Thesis by Vasileios Besikiotis

Enschede 23 of May 2008

Graduation Committee:
Prof. Dr. Ing. D.H.A. Blank (Chairman)
Dr. B.A Boukamp (Supervisor)
Dr. A.J.A Winnubst
M. Sc. N. Hildenbrand (Co-Supervisor)

Preface

With this report I summarize the research that I carried out within the Inorganic Materials Science Group, from September 2007 until May 2008. The objective goal of my research was the development of Gadolinia doped Ceria Electrolyte for IT-SOFC. Regardless the achievement or no of the objective goal of my research, this is something that the Committee will decide, I achieved goals in a personal level. Unfortunately I can not put all these things in a few lines of text; however they can be summarized in the following lyrics by Pink Floyd

" ... A soul in tension this is learning to fly...."

The completion of my Master studies in the field of Chemical Engineering would not be possible without the help of specific people all these years which I acknowledge at the end of this Thesis. Nevertheless I would like to dedicate this work to my father's memory

Vasilis Besikiotis

Enschede, May 2008

This research is performed in close collaboration with ECN and is financially supported by SenterNovem. SenterNovem is an agency of the Dutch Ministry of Economic Affairs and promotes sustainable development and innovation, both within the Netherlands and abroad.

Summary

The ongoing research is in the field of fuel cells and more specifically in Intermediate Temperature Solid Oxide Fuel Cells (IT-SOFC). Oil price, global warming, and the human need for energy generators with maximum efficiency, have led to the development of fuel cells. Fuel cells offer several advantages compared with the conventional methods.

The electrolyte in solid oxide fuel cells serves as the medium through which oxygen ions travel and reach the anode where they oxidize hydrogen. This study describes three main different synthesis routes for the optimization of the electrochemical behaviour of gadolinia doped ceria electrolyte.

This project is dealing with the development of a synthesis route which can lead to lower cost and efficient behaviour of the material. The main cost effective process in the fabrication of the electrolyte is the high sintering temperature; therefore lowering the sintering temperature can lead to scaling up a process in a feasible way. Nevertheless lowering the sintering temperature has a more dramatic impact on the behaviour of the material. Low sintering temperatures lead to small grain size and hence low grain boundary resistance. Small grain boundary resistance indicates low activation energy and essentially higher conductivity. All these factors can lead to a material with high efficiency and low cost.

Chapter 1 is an introductory chapter to fuel cells. The fundamentals and the thermodynamics of fuel cells and as well the different types of fuel cells are described in this chapter.

Gadolinia doped ceria oxide is classified as a ceramic and in chapter 2 a theoretical background regarding ceramics is given. Also a brief description about the different main synthesis routes and the different characterization techniques are pointed out.

Chapter 3 is referring to literature and what has been done up to date from different research groups. In chapter 4 a detailed description of the synthesis routes that had been followed during this project is given.

Chapter 5 and 6 are the characterization chapters. In chapter 5 the characteristics of the powders and pellets are described. Chapter 6 gives an overview of the electrochemical performance of the pellets.

Table of Contents

Theoretical Part 11

Chapter 1-Introduction 11

1.1 Fuel cells *11*

1.2 Why fuel cells *12*

1.3 Types of fuel cells *12*
13.1 Proton Exchange Membrane Fuel Cells (PEMFC) 12
1.3.2 Alkaline Fuel Cells (AFC) 13
1.3.3 Phosphoric Acid Fuel Cells (PAFC) 13
1.3.4 Molten Carbonate Fuel Cells (MCFC) 13
1.3.5 Solid Oxide Fuel Cells (SOFC) 14
1.3.6 Direct Methanol Fuel Cells (DMFC) 14

1.4 Principles of Solid Oxide Fuel Cells (SOFC) *14*
1.4.1 Thermodynamics 14
1.4.2 Efficiency 15
1.4.2.1 Thermodynamic Efficiency 15
1.4.2.2 Electrochemical efficiency 15
1.4.2.3 Faradaic efficiency 16

1.5 Materials Used in SOFC *16*

1.6 Scope of this Master Thesis *17*

References *19*

Chapter 2- Theoretical Background 20

2.1 The Definition of Ceramics *20*

2.2 Powder preparation methods *21*
2.2.1 The solid-state powder preparation Method 21
2.2.2 The Co-Precipitation Method 22
2.2.3 Complexation 23
2.2.4 The Sol-Gel Method 23

2.3 Sintering and grain growth *24*
2.3.1 Sintering 24
2.3.1.1 Driving Force 24
2.3.1.2 Diffusion 26
2.3.1.3 Defects and Sintering 26
2.3.1.4 Impurities and dopants 27
2.3.2 Grain growth 27

2.4 Characterization Techniques *29*
2.4.1 Scanning Electron Microscopy (SEM) 29
2.4.2 X-ray Diffraction (XRD) 29
2.4.3 Laser Diffraction 30
2.4.4 Thermogravimetric Analysis (TGA) 31
2.4.5 Electrochemical Impedance Spectroscopy (EIS) 31

References *32*

Chapter 3-Literature Review 33

3.2 Ceria based Electrolytes for IT-SOFC *33*

3.3 $Ce_{1-x}Gd_xO2_{-\delta}$ *34*

3.4 Synthesis of Ce0.9Gd0.1O2-δ and characterization *35*

3.5 Sintering additives *37*

3.6 Electrochemical properties *39*

3.7 Conclusions *40*

References *41*

Experimental Part 43

Chapter 4-Preperation of powders and pellets 43

4.1 Introduction *43*

4.2 Citrate route *43*

4.3 Complexation *44*
4.3.1 Complexation Low Concentration 44
4.3.2 Complexation High Concentration 45

4.4 Nomenclature *47*

4.5 Overview *47*

Chapter 5- Characterization and Densification behavior 48

5.1 Introduction *48*

5.2 Powders and pellets prepared with the Citrate Route *48*
5.2.1 Characterization 48
5.2.2 Densification Behavior 50

5.3 Powders and Pellets prepared with the Complexation Method Low Concentration *51*
5.3.1 Addition of HNO_3-Characterization 51
5.3.2 Addition of HNO_3- Densification Behavior 53
5.3.3 Without HNO3-Characterization 55
5.3.4 Without HNO3- Densification Behavior 57

5.4 Powders and Pellets prepared with the Complexation High Concentration Method *58*
5.4.1 Characterization 58
5.4.1 Densification Behavior 60

5.5 Discussion *61*

5.6 Conclusions *63*

5.7 Recommendations *63*

References *64*

Chapter 6-Electrochemical Characterization 65

6.1 Introduction *65*

6.2 Electrochemical Performance of pellets prepared with the Citrate Route *66*

6.3 Electrochemical Performance of pellets prepared with the Complexation Low Concentration Route *69*

6.4 Electrochemical Performance of pellets prepared with the Complexation High Concentration Route *72*
6.4.1 With HNO3 72

6.4.2 Without HNO3 74
6.5 Discussion *77*
6.6 Conclusions *80*
6.7 Recommendations *80*
References *81*

Appendix A 82

Appendix B-Normalized Impedance Spectra 83

Appendix C 86

Acknowledgments 92

Theoretical Part

Chapter 1-Introduction

1.1 Fuel cells

A fuel cell is an electrochemical energy converter, which can continuously convert the chemical energy of a fuel and an oxidant to electrical energy by a process involving an essentially invariant electrode electrolyte system [1]. Figure 1.1 depicts the operation principle and the basic elements of a fuel cell with a proton-conducting electrolyte. The three main elements are the anode the cathode and the electrolyte. The anode is supplied with the fuel (in this case H_2) which is oxidized releasing electrons performing electrical work. Electrons then pass to the cathode where they reduce the oxygen into water at the electrode/ electrolyte interface.

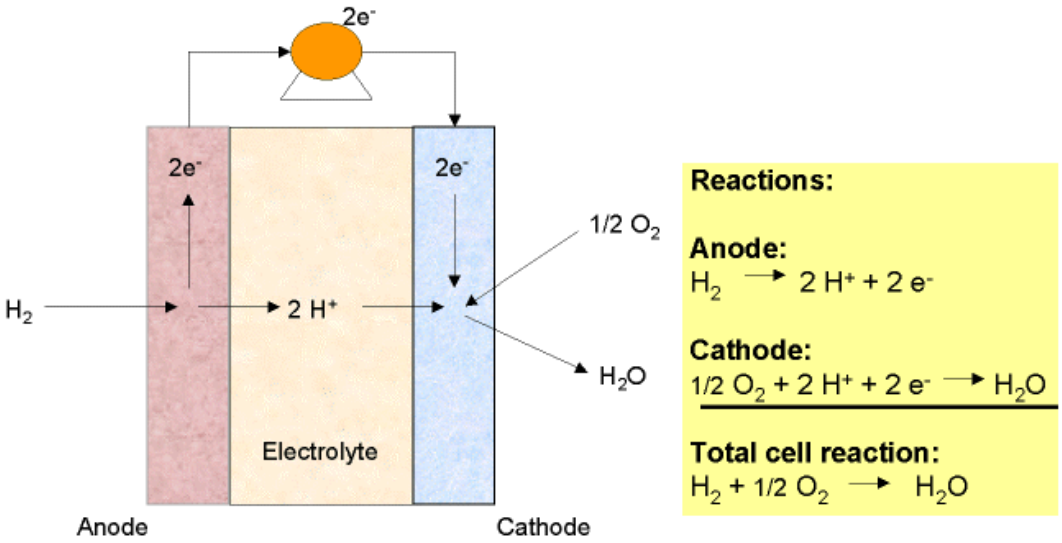

Figure 1.1 Operating principle of the fuel cell [2]

The electrolyte is the medium through which protons from the anode reach the cathode. Both anode and cathode should be porous in order to be permeable to gas.

1.2 Why fuel cells

Chemical energy can be converted to electrical energy via processes, which involve a conventional heating cycle, which is limited by the Carnot's cycle. Heat engines work according to the principle of indirect energy conversion, where heat is primarily produced then converted into mechanical energy and finally into electric energy. So in a conventional process the chemical energy of fossil fuels is converted to electrical energy after several steps comprising a chemical reactor, mechanical engines and electrical generators, where each step causes energy losses. Fuel cells can minimize these losses by converting chemical energy to electrical energy directly and without any Carnot cycle limitations.

Apart from the high efficiency of fuel cells, they also exhibit very low emissions, and especially the use of H_2 as fuel produces only water as by-product. Even at the high operating temperature of solid oxide fuel cells, 1000^{o}C, highly polluting nitrogen oxides are not produced, CO_2 is produced in reduced quantities, ashes and solid combustion products are not formed [1].

1.3 Types of fuel cells

Fuel cells are classified after the electrolyte they use as ion conducting medium, excluding the case of Direct Methanol Fuel Cells (DMFC), which is identified by the fuel that is using.

13.1 Proton Exchange Membrane Fuel Cells (PEMFC)

PEMFCs use a polymer membrane, perfluorosulfonic acid, as the electrolyte, and due to the acidic nature of the electrolyte, the ions transported are hydrogen ions (H^+). In that manner the fuel that is supplied to the system is hydrogen and oxygen or air as the oxidant.

In PEMFCs there are three critical points, the catalyst, the poisoning, and the water management [3]. PEMFCs operate at low temperature (60-100^{o}C) using acidic electrolyte. Therefore, noble metals are required for the catalyst layer. The cathode is the most essential electrode because catalytic reduction of oxygen is more difficult than catalytic oxidation of hydrogen.

The high activity of the catalyst has the disadvantage of the great affinity for carbon monoxide and sulfur products. These molecules strongly bind to the catalyst and inhibit hydrogen or oxygen from reaching it. Although poisoning from carbon monoxide can be prevented, this is cost ineffective since it requires individual treatment of each cell.

For the operation of PEMFCs the polymer membrane needs to be kept humid, since the conduction of ions in polymer membranes requires humidity.

Therefore the membrane should not be to dry because there will not be enough acid ions to carry the protons, but it should not be too wet because the pores of the diffusion layer will be locked and the reactant gases will not be able to reach the catalyst.

1.3.2 Alkaline Fuel Cells (AFC)

The electrolyte in AFCs is an aqueous solution of potassium hydroxide (KOH). The ions carried by the alkaline electrolyte are OH^- forming water at the anode electrode. AFCs exhibit high efficiency due to the fast kinetics allowed by the KOH electrolyte, since the oxygen reaction is much easier than the oxygen reduction in acidic fuel cells. The fast kinetics of AFCs allow the use of less expensive catalyst than platinum, such as silver or nickel.

AFCs operate over a wide range of temperature, from 80-230°C and pressure, from 2.2-45 atm. Although poisoning is also a problem in AFCs, since the hydroxide electrolyte has great affinity for carbon dioxide forming carbonate ions.

1.3.3 Phosphoric Acid Fuel Cells (PAFC)

PAFCs use phosphoric acid (H_3PO_4) as electrolyte in a liquid form. The electrolyte is acidic and conducts hydrogen ions. PAFCs operate above 42°C, which is the freezing point of H_3PO_4. Besides the low operating temperature of the stack, another advantage of PAFCs is the low cost of the electrolyte. However, the slow kinetics of the electrolyte, require expensive catalyst.

1.3.4 Molten Carbonate Fuel Cells (MCFC)

MCFCs use lithium potassium carbonate or lithium sodium carbonate in order to conduct ions. The conducted ions are carbonate ions (CO_3^{2-}) and the reaction mechanism is the following

Anode: $$H_2 + CO_3^{-2} \rightarrow H_2O + CO_2 + 2e^-$$

Cathode: $$\frac{1}{2}O_2 + CO_2 + 2e^- \rightarrow CO_3^{-2}$$

The operating temperature of MCFCs is from 500-800°C and CO_2 should be supplied at the cathode. MCFCs offer the advantage of low cost catalyst due to fast kinetics of the electrolyte, and the low sensitivity to poisoning. Although they need complex fuel cell system due to CO_2 cycling, additionally the electrolyte is very sensitive to corrosion.

1.3.5 Solid Oxide Fuel Cells (SOFC)

SOFCs use a ceramic membrane for the conduction of ions at temperatures above 600°C. SOFCs are classified to intermediate and high temperature solid oxide fuel cells. Intermediate temperature SOFCs (IT-SOFC) operate in the range of 600-800 °C, using ceria-doped rare earth (e.g. gadolinium) electrolytes. High temperature SOFCs use yttrium stabilized zirconia (YSZ) and operate in the range of 1000-1200°C.

1.3.6 Direct Methanol Fuel Cells (DMFC)

DMFCs use trifluoromethane sulfonic acid or a PEM as electrolyte. Instead of using H_2 or other fuel, they use methanol which is directly supplied to the cell. The major advantage of methanol is that it is liquid and therefore easy to store and distribute. DMFCs operate at 50-100°C and exhibit lower efficiency than the other fuel cell systems.

1.4 Principles of Solid Oxide Fuel Cells (SOFC)

1.4.1 Thermodynamics [5]

As already mentioned, SOFCs use a ceramic membrane as an electrolyte for the diffusion of oxygen ions through the electrolyte towards the anode. Figure 1.2 illustrates the configuration of a SOFC and the operation principle using H_2 as a fuel.

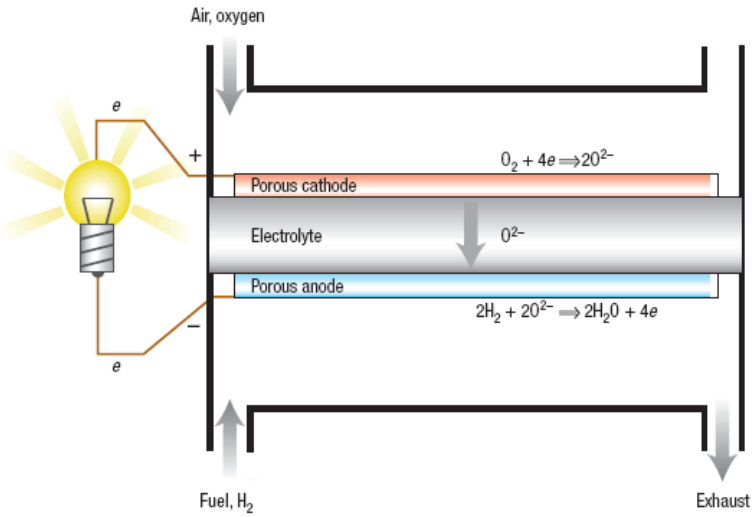

Figure 1.2 Operation principle of SOFC [4].

As it is depicted in figure 1.2 the core parts of a SOFC are the cathode, where the oxygen is supplied, the electrolyte which serves as the oxygen ion transport medium, and the anode where the fuel is supplied. Oxygen is reduced at the cathode to oxygen ions, which are incorporated into the solid electrolyte. Oxygen ions from the electrolyte oxidize the H_2 at the anode, forming water and free electrons.

The electrochemical difference between the anode and the cathode leads to a potential difference across the cell which corresponds to the Gibb's Free Energy ΔG^o of the oxidation reaction of H_2.

$$H_2 + \frac{1}{2}O_2 \rightarrow H_2O$$

$$U_0 = -\frac{\Delta G^0}{2F} + \frac{RT}{2F} \times \ln\left(\frac{\sqrt{p(O_2)_{cathode}}\, p(H_2)_{anode}}{p(H_2O)_{anode}}\right) \qquad (eq.1.1)$$

Where U_o is the potential difference in the fuel cell between the anode and the cathode, p is the partial pressure of the reacting species, T is the operating temperature, R is the gas constant and F is the Faraday constant.

1.4.2 Efficiency [6]

1.4.2.1 Thermodynamic Efficiency

In principle for an electrochemical energy converter the free-energy of the reaction may be totally converted to electrical energy, and the thermodynamic efficiency is given by equation 1.2

$$n_{th} = \frac{\Delta G^0}{\Delta H} = 1 - \frac{T\Delta S}{\Delta H} \qquad (eq.1.2)$$

Where n_{th} is the thermodynamic efficiency, ΔG^o is the Gibb's free-energy, ΔH is the change in enthalpy, and ΔS is the change in entropy.

1.4.2.2 Electrochemical efficiency

Electrochemical efficiency is a measure of the quality of a fuel cell, since cells of different designs, in which the same reaction with the same enthalpy occurs, might obtain different electrochemical efficiencies. Equation 1.3 describes the electrochemical efficiency

$$n_{el} = \frac{E_K}{E_0} \qquad (eq.1.3)$$

Where n_{el} is the electrochemical efficiency, E_K and E_o are the operating and standard electrode potential respectively.

1.4.2.3 Faradaic efficiency

The faradaic efficiency n_f is the ratio between the measured current (I) of the cell, over the theoretical expected current (I_m) based on the amount of reactants consumed, assuming that the overall reaction in the fuel cell proceeds to completion.

$$n_f = \frac{I}{I_m} \qquad (eq.1.4)$$

1.5 Materials Used in SOFC

The basic components of a SOFC, is the anode, the cathode and the electrolyte. The efficiency of a SOFC depends largely on certain features of these materials. The electrolyte should be dense (gas-tight) in order to separate the oxidant and fuel gases, and on the contrary, the anode and the cathode should be porous in order to allow the gas transport to the reaction sites. Additionally these materials should also exhibit stability in oxidizing and/or reducing environments, chemical compatibility with other components and conductivity. Table 1.1 summarizes the state of the art materials used up to date in SOFC [7].

Table 1.1 State of the art materials used in SOFC and relevant properties [7]

Component	*Composition*	*Specific Ionic Conductivity at 1000°C*	*Specific Electronic Conductivity at 1000°C*	*Conductivity depending on*
Anode	*Ni/YSZ*	-	*400-1000 S/m*	*Ni/YSZ particle size ratio; Ni content*
Cathode	$La_{1-x}Sr_xMnO_{3-\delta}$	10^{-8}-10^{-7} *S/m*	*6-60 S/m*	*Porosity; Sr content*
Electrolyte	$Y_2O_3ZrO_2$	*180 S/m*	10^{-15} *S/m*	*Density; Yttria content*

The materials referred in table 1.1 are used in the so-called High Temperature SOFC operating at around 1000^{o}C. The high operating temperature of these systems has certain disadvantages, such as degradation of the material at these high temperatures and the high operating cost of the system.

These two main drawbacks led to the investigation for the development of new materials that reveal high conductivity and stability at lower temperatures. Solid electrolytes based on doped cerium dioxide $Ce(Re)O_{2-\delta}$ (Re: rare-earth or alkaline-earth cations) are of considerable interest for potential use in SOFC due to the higher ionic conductivity with respect to stabilized zirconia at temperatures between 500-800 ^{o}C [8]. Apart from the electrolyte, extensive research is focusing on the cathode materials. A good electrochemical activity in contact with $Ce(Re)O_{2-\delta}$ is pointed out with $La_{0.8}Sr_{0.2}Fe_{0.8}Co_{0.2}O_{3-\delta}$ and $LaFe_{0.5}Ni_{0.5}O_{3-\delta}$, and $LaCoO_{3-\delta}/La_2Zr_2O_7$.

1.6 Scope of this Master Thesis

The aim of this project is the development of gadolinia doped ceria oxide electrolytes ($Ce_{0.9}Gd_{0.1}O_{2-\delta}$) through different synthesis routes that can lead to lower sintering temperatures and good electrochemical behaviour.

Up to date, the sintering temperature of $Ce_{0.9}Gd_{0.1}O_{2-\delta}$ is above 1500 ^{o}C without the addition of any sintering aids, such as transition metal oxides (TMOs). Addition of a sintering aid like lithium can lower the sintering temperature even to 800 ^{o}C [9], although there is a practical question, using such a volatile metal when it comes to commercialization of a synthesis route, since impurities are unavoidable and lithium does not have scavenging properties. Chapter 3 describes what has been done up to date with respect to different syntheses routes and the use of different sintering aids.

Therefore, there is an apparent need for the development of a synthesis route that can lead to low sintering temperatures and good electrochemical behaviour in order to make the production of SOFCs economically feasible. Additionally further lowering of the sintering temperature may make possible to co-sinter anode-electrolyte-cathodethree layer structure of SOFCs [10]. Sintering temperature is also related with the grain size. Decrease of sintering temperature leads to smaller grain size [10], leading to higher conductivities [11].For the achievement of this goal, three different syntheses routes compared.

For each route three different pellets are fabricated, one without the addition of a sintering aid and two with the addition of iron as a sintering aid. The major motivation for the use of iron as sintering agent was its scavenging effect, since impurities are unavoidable. Literature review showed that up to date iron is introduced as iron (III) oxide (Fe_2O_3) after the fabrication of the precursor powder via ball milling. Therefore the addition of iron as iron nitrate ($Fe(NO_3)_3 \cdot H_2O$)) during the synthesis of the precursor powder (*"in situ"*) was tested revealing promising results with respect sintering temperature and densification behaviour.

A new modified complexation method was tested. In this method the effect of the addition or not of nitric acid during the formation of the polymeric network where the precursor powder is dispersed was examined. Also the concentration of raw materials (ceria nitrate hexahydrate and gadolinia nitrate hexahydrate) was varied, revealing that for high concentration of raw materials the calcination step seems feasible, due to pyrolysis in such a way that carbonates and impurities decompose. However, the control of pyrolysis seems to be an obstacle, since an exothermic reaction is taking place releasing a big amount of energy and in that manner the obtained fine powder is hard to collect.

The characterization of the microstructure was made by using three different techniques, X-ray diffraction (XRD), Scanning Electron Microscopy (SEM), and particle size distribution using laser diffraction. Thermogravitational analysis (TGA) used in order to check the need of the calcination step for the powders that produced using high concentration of raw materials. The electrochemical performance of the electrolyte was tested by means of electrochemical impedance spectroscopy (EIS) under the whole range of operating temperature 500-800^{o}C of IT-SOFC.

References

[1] K.V Kordesch, J. C. T. Oliveira, *Ullmann's Encyclopedia of Industrial Chemistry*, *5th Edition, VCH*, **Vol. A 12** 55-53

[2] http://www.fz-juelich.de

[3] M. Ehsani, Y. Gao, S. E. Gay, A. Emadi, *Modern Electric, Hybrid Electric, and Fuel Cell Vehicles. Fundamentals, Theory, and Design. CRC Press 2005*

[4] Bernard A. Boukamp, *Nature Materials,* **vol. 2** (2003) 294-296

[5] P. Holtappels and U. Stimming, *The Handbook of Fuel Cells, Fundamentals, Technology and Applications,* Wolf Vielstich, Arnold Lamm, Hubert A. Gasteiger, Wiley **Vol. 1** 2003

[6] K. Kordesch. G. Simader, *Fuel Cells and their Applications, VCH, 1996*

[7] Arjen Giesbers, *Master Thesis, University of Twente, 2004*

[8] V. V. Kharton, F. M. Figueiredo, L. Navaro, E. N. Naumovich, V. Kovalevsky, A. A. Yaremchenko, A. P. Viskup, A. Carneiro, F. M. B. Marques, J. R. Frade, *Journal of Materials Science* **36** (2001) 1105-117.

[9] Jason D. Nicholas, Lutgard C. De Jonhe, *Solid State Ionics,* **178** (2007) 1187-1194

[10]C.Xia, M. Liu, *Solid State Ionics,* **152,** (2002) 423-430

[11] Y.-M. Chiang, E.B. Lavik, I Kosacki, H.L Tuller, J.Y. Ying, *Appl. Phys. Lett.* **69** (2), (1996) 185-187

Chapter 2- Theoretical Background

2.1 The Definition of Ceramics

In Greek *ceramic* (κεραμικό) is defined as something which is processed by heat. Therefore ceramics can be defined as solid compounds that are formed by the application of heat, and sometimes heat and pressure, comprising at least one metal and a nonmetallic elemental solid or a nonmetal, a combination of at least two nonmetallic elemental solids, or a combination of at least two nonmetallic elemental solids and a nonmetal [1].

Ceramics chemically are classified as inorganic compounds, and can be simple oxides, such as Magnesia (MgO) and alumina (Al_2O_3), where a metal, Mg or Al, is bonded to a nonmetal, O_2, or silicates such as kaolinite ($Al_2Si_2O_5(OH)_4$), or complex oxides such as barium titanate ($BaTIO_3$) and the superconducting material $YBa_2Cu_3O_{6+\delta}$ ($0 \leq \delta \leq 1$). In addition, there are nonoxides, including carbides, nitrides, borides, silicides and halides.

The interest of research in the past 50 years has been focused on the so called *advanced or functional ceramics* [2], which are ceramics with enhanced properties used for electrical, magnetic, electronic and optical applications.

Ceramics, as all materials, can be either crystalline or amorphous. The (micro) structure of a material determines its properties. There are two scales in which we can regard the structure of the ceramics, the first one, in atomic scale where the type of bonding and the type of structure, crystal or amorphous, play a significant role. The second type is at large scale which is referred as microstructure and determines the nature, quantity and distribution of the structural elements or phases in the ceramic.

The properties of ceramic materials can be divided in the properties which depend on the microstructure of the material and the intrinsic properties. The intrinsic properties of a ceramic are those properties that are characteristics of the material and are not affected by the microstructure (i.e. grain size, crystal orientation of grains), properties such as the melting point. On the other hand properties which are crucial for the engineering behavior of the ceramic can be tuned by the modification of the microstructure of the material, such as ferroelectricity, semiconduction, magnetism, coefficient of thermal expansion, which can also be classified as intrinsic properties.

Ceramics as class can be characterized as, hard, and prone to thermal shock, refractory, electrically and thermally insulative, nonmagnetic, chemically stable and oxidation resistant. Although there are deviations from these general characteristics, since by modifying their structure, can become electrically and thermally conductive, or even superconductive, and magnetic. So it is obvious that ceramics can cover a wide range of applications. In that manner *traditional ceramics* are used as structural building materials, refractories for furnace linings, sanitaryware, and insulators. Advanced ceramics due to their enhanced

and diverse properties can cover a wide and rapidly grown area of applications, ranging from ceramic engines to optical communications, electrooptic applications to laser materials, substrates in electronic circuits to electrodes in photoelectrochemical devices [1] and as electrolytes for solid oxide fuel cells. Figure 1.1 illustrates the important relationships in ceramic fabrication.

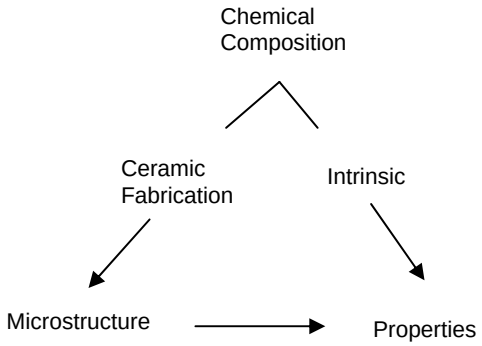

Figure 2.1 The important relationships in Ceramic fabrication [2]

2.2 Powder preparation methods

The need for ceramic materials for different applications and with different properties has led to the development of a significant variety of methods for preparing them. Therefore the method that should be chosen each time depends not only on the composition of the material but also on the form it is required for its proposed use. The description of all methods that are used is beyond the scope of this thesis, therefore consideration will be given to those that were used by the author, for the propose of his research. Emphasis will be placed on the *solid-state powder preparation method*, *sol-gel, co-precipitation and complexation*.

2.2.1 The solid-state powder preparation Method [3]

The simplest and most common method is the ceramic method, used both in industry and in the laboratory. In the ceramic method the heating of two non-volatile solids takes place in order to form the desired product. The first high temperature superconductors were obtained using this method.

Although the ceramic method encounters several disadvantages, high temperature is required (between 500-2000^{o}C) meaning high input of energy and sometimes may cause unstable phase or compound. Additionally diffusion of ions is not very fast, and this is because even by increasing the temperature in order the reaction to occur faster and diffusion of ions to take place, there is a plateau of temperature that could be reached, which is, as rule of thumb, the two-thirds of the melting temperature of the solids. Apart from ion diffusion

problems, even by grinding the materials carefully the particle size would only be reduced to around 0.1 μm which is still not enough.

The mathematical description of the solid-state preparation method can be given by simplifying the shape of the solid particles to spherical [11]. The *Carter relation* (equation 2.1) describes the time *t* of the reaction of a volume fraction *x* of a reactant *A* with radius *r*.

$$[1+(z-1)]^{2/3}+(z-1)(1-x)^{2/3}=z+2(1-z)\left(\frac{Kt}{r^2}\right) \qquad (eq.2.1)$$

Where *z* is the ratio of volume formed to volume consumed, and *K* is the apparent rate constant. The effect of temperature is expressed from an Arrhenius relation (equation 2.2). K_o is the pre-exponential factor that depends on the diffusion path length, and *Q* is the apparent activation energy for diffusion. However, even though the reaction is a function of diffusion and temperature, the temperature has greater influence an the rate constant K_o.

$$K=K_o\exp\left(\frac{-Q}{RT}\right) \qquad (eq.2.2)$$

Regarding the procedure of the method is rather simple. Firstly the grinding of the materials is taking place, where a homogenous mixture should be formed with small particle size of the grains, and then they are placed in a furnace to the desired temperature for several hours until the desired product is obtained.

It is quite common that the reaction mixture is often removed during the heating process and reground in order to bring the “fresh” surfaces in contact and so to speed up the reaction. Although homogenicity of the product is harder to achieve since as the reaction proceeds a layer of the ternary oxide is produced at the interface of the two crystals, and so ions have to diffuse through this before they react. Therefore the mixture has to be regrind and reheated until the desirable phase is reached.

2.2.2 The Co-Precipitation Method

In order to overcome some of the disadvantages of the ceramic method new methods were encouraged. Therefore the new techniques pioneered in order to bring the components of the reaction into more intimate contact or into contact at an atomic level, and so to reduce the diffusion path and the reaction could take place in lower temperatures.

Co-precipitation is used in order to obtain the starting materials, where a stoichiometric mixture of soluble salts of the metal ions is dissolved and then

precipitated as hydroxides, citrates, oxalates or formates. Then this mixture is filtered, dried and then heated to give the desired product [3].

2.2.3 Complexation [11]

In the complexation method the immobilization of the precursor solution is achieved by the formation of a viscous matrix in which the precursor is either dispersed or it forms a polymeric network. The important step during complexation is the fast dehydration at low temperature and pressure starting from a solution of cations and complexing agent. The final powder is obtained by the pyrolysis of the viscous solution. The advantages of this method are, versatility in the choice of materials, the good homogeneity and sinter reactivity of the resulting powders, and the ease to perform this method on lab scale.

2.2.4 The Sol-Gel Method

In sol-gel method, colloidal particles, dispersed in a suspension (a sol) undergo further reactions, which causes the colloidal particles to join together in a continuous network called a gel. The gel is dried, calcined, and in the case of powder milled [11].

The major drawback of the co-precipitation method is the fact that the stoichiometry of the precipitates may not be exact, in case one or more ions are left in the solution, whereas in sol-gel process the reactants never precipitate [3]. Initially the “sol” is prepared, which is basically a concentrated solution or colloidal suspension of the reactants, and finally is concentrated to form the “gel”, which is then heated to form the product.

The sol preparation can be either the dispersal of an insoluble solid or the addition of a precursor which reacts with the solvent to form a colloidal product. Then the sol is either treated or simply left to form the gel overtime by dehydrating and/or polymerizing, and finally the gel is heated in order to obtain the final product.

The final step of heating is of great importance because it removes the solvent, it decomposes anions, it allows rearrangement of the structure of the solid, and it allows crystallization to occur. Also sol-gel process overcomes the disadvantages of the ceramic method which are the time and temperature, since there is a decrease in the reaction time from days to hours and in the temperature, the decrease is of the order of few hundred degrees.

2.3 Sintering and grain growth

2.3.1 Sintering

Sintering can be defined as the final step of the formation of a ceramic, where it is converting from a powder to a dense solid under heat. The sintering process during the fabrication of a ceramic is of great importance since the obtained microstructure from this step defines the desired properties of the material. Solid state sintering is divided into three stages [11]. Initially the powder particles grow together and necks are formed at the interfaces, and some particle rearrangement may occur. In the second intermediate stage, the pores and particles form an intersecting network, and the density increases to 90-95%. Finally discrete pores are present which can only be removed by further grain growth (figure 2.2).

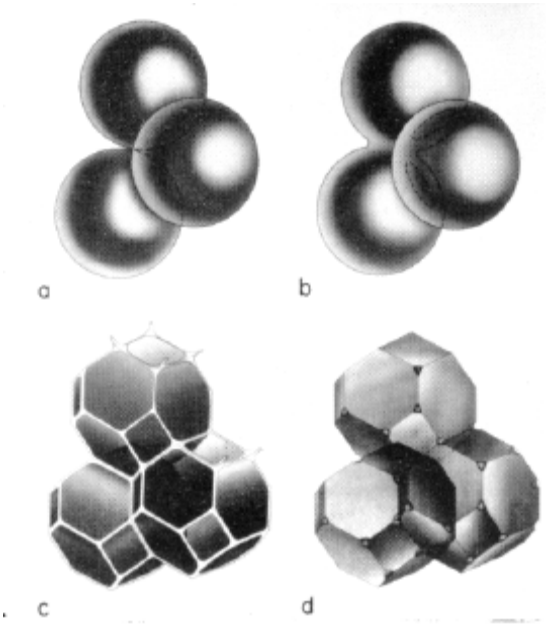

Figure 2.2 Sintering Stages (a) green Compact (b) neck formation (c) neck area formation and continuous, open per channels (d) final stage with close porosity [11]

2.3.1.1 Driving Force

Sintering can occur in the presence or absence of a liquid phase. In the case of *liquid-phase sintering* the compositions and firing temperatures are chosen in that manner that some liquid is formed during the process. In the absence of a liquid phase, the process is referred as *solid-state sintering* [1].

In order, sintering to occur there must be a decrease in the free energy of the system (Gibb's energy $\Delta G<0$) or a reduction of the surface [11]. The result of sintering is a decrease in surface area by elimination of solid-vapor or soli-solid interface described by equation 2.3, in the case where no second phases are present.

$$\Delta G = \Delta G_s + \Delta G_b = \gamma_s \Delta A_s + \gamma_b \qquad (eq.2.3)$$

Where ΔG is the change in Gibb's energy of the compact, γ_s and γ_b the interface (surface) energy, and ΔA_s and ΔA_b the change in surface area of the solid-vapor (s) and the solid-interface (b) respectively.

Regarding the curvature of the particle surface, in the absence of an external stress and a chemical reaction surface curvature provides the driving force for sintering. The effect of the curvature on sintering can be observed by assuming 1 mole of powder which consists of spherical particles with radius α, and then the number of particles is given by eq. (2.4)

$$N = \frac{3M}{4\pi\alpha^3\rho} = \frac{3V_m}{4\pi\alpha^3} \qquad (eq.2.4)$$

Where ρ is the density of the particles, which assumed to contain no internal porosity, M is the molecular weight, and V_m is the molar volume. The surface area of the system of particles is

$$S_A = 4\pi\alpha^2 N = 3V_m / \alpha \qquad (eq.2.5)$$

So if γ_S is the surface tension of the particles, then the surface free energy associated with the system of particle is

$$E_s = \frac{3\gamma_s V_m}{\alpha} \qquad (eq.2.6)$$

For γ_S = 1 J/m², α = 1μm, and V_m = 25 x 10^{-6} m^{-3}, then E_s = 75 J for one mole of material providing the driving force for sintering, which also represents the decrease of surface free energy of the system.

An externally applied pressure in the absence of a chemical reaction is the driving force for sintering when the pressure is applied on the system in a significant part of the heating process. In that case the contribution of the surface curvature on sintering is much smaller compared with that of the applied pressure. For 1 mole of particles the work done on the system is given by eq. 2.4 which represents the driving force for sintering:

$$W = p_\alpha V_m \qquad (eq.2.7)$$

Where $p\,\alpha$ is the applied pressure and V_m is the molar volume.

2.3.1.2 Diffusion

The driving force can be characterized as the motivation for sintering to occur although the main process for sintering to occur is the diffusion. The law that governs diffusion is Fick's law. The driving force for species to diffuse through a medium is a concentration gradient. Fick's 1st law describes the diffusion of species through a medium as function of distance, and states that the flux of the diffusing species is proportional to the concentration gradient, and occurs in the direction of decreasing concentration (eq. 2.8).

$$\mathbf{J} = -D\nabla C \qquad (eq.2.8)$$

Where D is the proportionality constant known as diffusion coefficient, and the flux $\boldsymbol{J}$ is a vector with components J_x, J_y, and J_z for Cartesian coordinates. When the concentration varies as function of time then the diffusion of species through a medium is described by Fick's 2nd law, which for Cartesian coordinates is described by eq.2.10.

$$\frac{\partial C}{\partial t} = \nabla D\nabla C \approx D\nabla^2 C \qquad (eq.2.9)$$

$$\frac{\partial C}{\partial t} = D\left(\frac{\partial^2 C}{\partial x^2} + \frac{\partial^2 C}{\partial y^2} + \frac{\partial^2 C}{\partial z^2}\right) \qquad (eq.2.10)$$

2.3.1.3 Defects and Sintering

Diffusion in solids takes place because of the presence of defects [2]. Diffusion of matter through the solid state is regulated by defects, which determine the path of matter transport, and furthermore they regulate the properties of the solid. Defects fall in two main categories *intrinsic* and *extrinsic defects,* and classified in three groups, the point defects, the planar and the line defects.

Intrinsic defects, also called stoichiometric defects are those where the chemistry of the crystal does not change. The three most common intrinsic defects are the *Schottky, Frenkel* and *anti-Frenkel defects*. On the contrary extrinsic defects are caused by external influences such as oxygen partial pressure, which can lead to nonstoichiometry, and impurities or dopants [2].

2.3.1.4 Impurities and dopants

Dopants are regarded as the ions that have been added to the material in controlled quantities (the concentration of dopant in the material is as low as a fraction of a mole per cent) in order to modify the microstructure during the firing process and further more the properties of the obtained material. On the other hand the term *impurities* is referred to the substances that are accidently incorporated in the material as a result of synthesis process.

As *donor dopants* are considered dopants in which the cation valence is greater than that of the host crystal, similarly *acceptor dopants* are those in which the cation valence is smaller than that of the host crystal.

A dopant can influence both the kinetic and thermodynamic factors during sintering process. A dopant can alter the grain boundary diffusion coefficient since the segregation of the dopant can alter the composition and structure of surfaces and interfaces and in that way also the surface diffusion coefficient as well the diffusion coefficient for the vapor phase can also be altered. In a thermodynamic prospective, a change in the surface energy γ_{sv} and in the grain boundary energy γ_{gb} occurs. Also the intrinsic grain boundary mobility can be altered when a dopant is added. Therefore it could be said that in principle a good dopant can alter many phenomena in a favorable way and few in an unfavorable way, although the theory behind these mechanisms is still unclear and the selection of dopants remains empirical.

2.3.2 Grain growth

Grain growth takes place in the final step of sintering where a coarsening of the microstructure by grain growth occurs. According to the law of conservation of matter the sum of the individual grain size must remain constant; therefore the increase of the average size of the grains is accompanied by the disappearance of some grains.

Grain boundaries usually formed between two or more grains which have different crystallographic orientations and discontinuities in atomic orientation and electronic potential [4]. Grain growth occurs as atoms or ions diffuse less than an interatomic distance to new positions. Thus one grain grows at the expense of another. As depicted in figure 2.4 the atoms move from the convex to the concave due to a chemical potential gradient difference, since the chemical potential of the atoms under the convex surface is higher than that of the atoms under the concave surface.

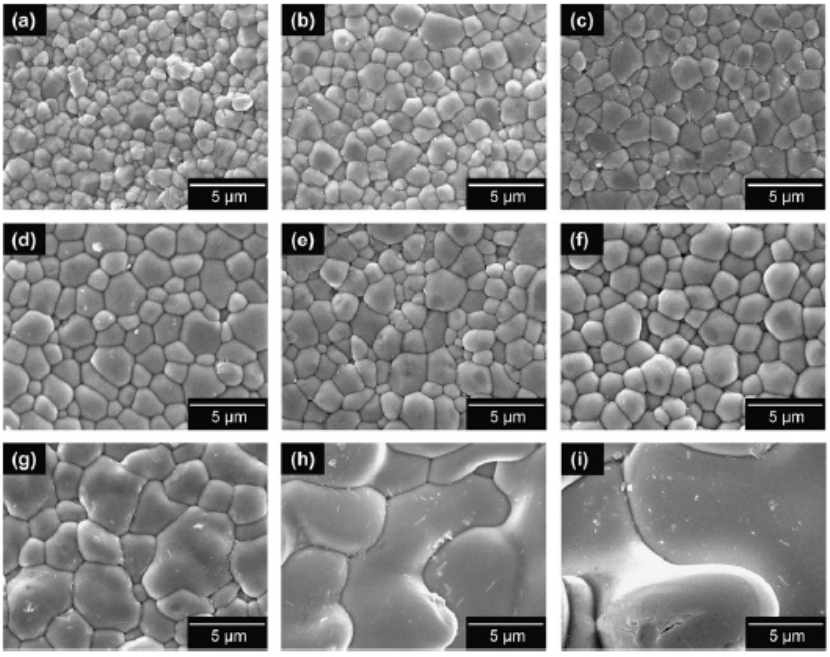

Figure 2.3 time evolution of microstructure by consumption of the smaller grains by the larger [5]

The atoms in the grain boundary have a higher energy than those in the bulk of the crystalline grain. In that manner as the driving force for this process is the decrease in grain boundary energy that results from a decrease in the grain boundary area.

Studying the process that leads to grain growth is essential since the grain size is a major factor that determines many of the properties of the material. When during grain growth the grain sizes and shapes occur within a fairly narrow range, and the distribution in grain sizes at later time is fairly similar to that at an early time except for a magnification factor, then grain growth is characterized as *normal*. On the other hand when a small number of grains grow very rapidly to sizes that are more than an order of magnitude larger than average in population, the growth is characterized as *abnormal*. This growth has a considerable effect on the mechanical properties of the material, since the walls of these large grains can pull away from porosities, leaving them trapped within them, which in turn limits the possibility of obtaining theoretical densities in reasonable times [1].

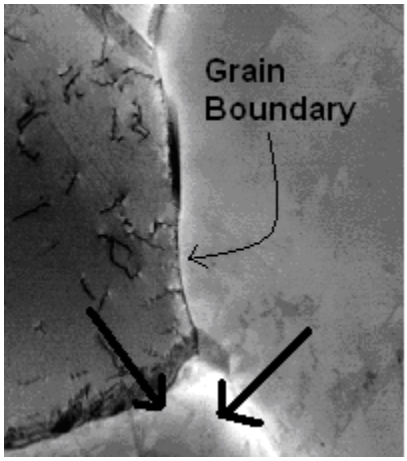

Figure 2.4 Grain boundaries, and the movement of the grain boundary toward the center of curvature

2.4 Characterization Techniques

2.4.1 Scanning Electron Microscopy (SEM)

Electron microscopy is used to study the structure, morphology, defects, and to determine the distribution of elements. A conventional microscope uses visible radiation (400-700 nm) and so cannot resolve images of objects, which are smaller than half the wavelength of light. On the contrary, electron microscopes allow resolution down to 0.1 nm [3]. The electron beam is produced by heating a tungsten filament, and focused by magnetic fields in a high vacuum.

In SEM, the electrons are rastered across the surface of the sample. Electrons reflected by the surface of the sample and emitted secondary electrons are detected to give a map of the surface topography of the sample.

2.4.2 X-ray Diffraction (XRD)

X-ray diffraction (XRD) is a versatile, non-destructive technique that reveals detailed information about the chemical composition and crystallographic structure of natural and manufactured materials [7].

X-rays are a form of electromagnetic radiation that have high energies and short wavelengths (in the order of the atomic spacing of solids) [8]. When an x-ray beam with wavelength λ impinges on a solid material at an angle θ, a portion

of this beam will be scattered in all directions by the electrons associated with each atom or ion that lies within the beams path. Diffraction will occur when the distance traveled by the rays reflected from successive planes differs by a complete number *n* of wavelengths (constructive interference).

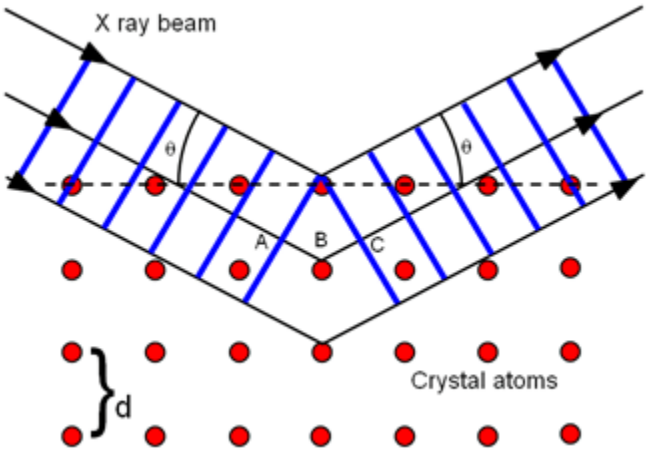

Figure 2.5 Diffraction of X-rays by planes of atoms [9].

By varying the angle θ, the Bragg's Law (equation 2.11) conditions are satisfied by different *d*-spacing in polycrystalline materials. Plotting the angular positions and intensities of the resultant diffracted peaks of radiation produces a pattern, which is characteristic of the sample [7].

$$n\lambda = 2d_{hkl}\sin\theta \qquad (eq.2.11)$$

If Bragg's law is not satisfied, then the interference will not be constructive in nature so as to yield a very low-intensity diffraction beam.

The magnitude of the distance, d_{hkl}, between two adjacent and parallel planes of atoms is a function of the Miller indices (*h, k, l*) as well as the lattice parameters (*a, b, c*). For example, for crystal structure that has cubic symmetry d_{hkl} is given by equation 2.12

$$d_{hkl} = \frac{a}{\sqrt{h^2 + k^2 + l^2}} \qquad (eq.2.12)$$

2.4.3 Laser Diffraction

Laser diffraction is one of the simplest methods to determine the particle size distribution. For particles larger than the wavelength of light, the light scatters

from the edge of the particle at an angle which is dependent on the size of the particle [6]. Larger particles scatter light at relatively smaller angles than light scattered from smaller particles. From observing the intensity of light scattered at different angles, the relative amounts of different size particles can be determine.

2.4.4 Thermogravimetric Analysis (TGA)

Thermal analysis methods investigate the properties of solids as function of temperature [3]. They are useful to determine phase changes, decomposition, loss of water or oxygen, and for constructing phase diagrams. In TGA the weight of a sample is monitored as function of temperature in an increased controlled uniform rate. The loss of water of crystallization or volatiles such as oxygen shows up as weight loss, and oxidation or absorption of gas shows up as a weight gain.

2.4.5 Electrochemical Impedance Spectroscopy (EIS) [10]

Electrochemical Impedance Spectroscopy (EIS) is a method of characterizing the electrical properties of materials and their interfaces with electronically conducting electrodes. The evaluation of the electrochemical behavior of electrolyte and/or electrode materials is done by applying voltage to the electrodes and observe the response. It is assumed that the properties of the electrode-material system are time-invariant and EIS is used to determine these properties.

There are three different types of electrical stimuli, which are used in EIS. First, in transient measurements a step function of voltage is applied at $t=0$ to the system and the resulting time-varying current $i(t)$ measured. A second technique that is used, is to apply a signal $v(t)$ composed of a random (white) noise to the interface and measure the resulting current. The third technique is to measure the impedance by applying a single frequency voltage or current to the interface and measuring the phase shift and amplitude, or real and imaginary parts, of the resulting current at that frequency.

EIS studies the intrinsic properties that influence the conductivity of an electrode-material system. There are two categories of parameters that can be derived from an EIS spectrum. The first category is the parameters that are related only to the material it self such as, conductivity and dielectric constant. The second class of parameters are the ones which are related with the electrode-material interface, such as absorption-reaction rate constants and diffusion coefficient of neutral species in the electrode itself.

References

[1] Michel Barsoun, *Fundamentals of Ceramics*, The McGraw Hill Companies, Inc. 1997

[2] M. N. Rahaman *Ceramic Processing and Sintering*, Marcel Dekker Inc, 1995

[3] Lesley E. Smart and Elaine A. Moore, *Solid State Chemistry "An Introduction"*, 3rd Edition, CRC Taylor and Francis Group, 2005

[4] Hroaki Yanagida, Kunihiko Koumoto, Masaru Miyayama, *The Chemistry of Ceramics,* Wiley and Maruzen, 1996

[5] C. Sangsubun, A. Watcharapasorn, S. Jiansirisomboon , *Current Applied Physics **8** (2008) 61–65*

[6] http://www.jobinyvon.com

[7] http://www.panalytical.com

[8] William D. Callister, *Materials Science and Engineering An Introduction,* Wiley 7th Edition 2007

[9] http://www.iop.org

[10] Evgenij Barsoukov, J. Ross Macdonald, *Impedance Spectroscopy Theory, Experiment, and applications,* Wiley 2nd Edition 2005.

[11] Louis Winnubst, *Ceramic Processing and Microstructures Lecture Nores,* University of Twente 2007

Chapter 3-Literature Review

3.1 Introduction

An intensive investigation has been done to reduce the operating temperature of SOFC down to 800-500^{o}C. As it will be discussed later, there are two main reasons why research is directed towards this direction, ceria oxide electrolytes are the most promising ones for this range of temperatures due to their high ionic conductivity.

In order to introduce oxygen vacancies different dopants have been used, such as gadolinia, samaria, and yttria, with gadolinia being the most suitable. The sintering temperature of gadolinia doped ceria electrolytes is above 1500^{o}C, therefore in order to reduce the sintering temperature sintering agents, such as transition metal oxides, have been used managing to drop the sintering temperature down to 800^{o}C.

Depending on the type and amount of dopant, ceria oxide electrolytes reveal different electrochemical properties. Sintering agents can also influence the electrochemical behavior of ceria oxide electrolytes, since they have an effect on the electrical conductivity and impurities (scavenging effect [11]).

3.2 Ceria based Electrolytes for IT-SOFC

Up to date SOFC using YSZ as an electrolyte operate in the temperature regime of 900-1000 ^{o}C. Apart from the high efficiency of stacks using YSZ, which theoretically can reach the 100%, the high operating temperature is not cost effective in two ways. Primarily at such high temperatures degradation of the material occurs, and secondly the overall system cost is high. Therefore the need for an optimum trade-off between performance and life time of the stack and as well the reduction of the overall cost of the system, led to the development of fluorite-type oxide electrolytes $Ce(Re)O_{2-\delta}$ (Re: rare-earth or alkaline-earth cations).

In order for the new material to be successful, it should combine high ionic conductivity, high electronic resistance and mechanical stability. Steele [6] classified three different operating temperature regimes (500-700^{o}C, 700-900^{o}C, 900-1000^{o}C) in accordance with the selection of the components that compose SOFC, and defined as Intermediate Temperature (IT) the 500-700^{o}C regime.

$Ce_{1-x}Re_xO2_{-\delta}$ (Re: Gd^{+3} or Sm^{+3} and x=0.10-0.20) is the material with the potential to reduce the operation temperature to 500-700 ^{o}C, since at this temperature regime it still reveals high oxide ion conduction. However, the main

disadvantage of doped $CeO_{2-\delta}$ is the relatively easy reducibility at low oxygen partial pressures. This effect leads to a reduction of the electronic resistance, and possible mechanical failure of the material, due to large oxygen chemical potential gradient [1-5].

3.3 $Ce_{1-x}Gd_xO2_{-\delta}$

For most SOFC applications sufficient oxygen ion conductivity should exceed 10^{-1} S cm^{-1} [5]. Oxygen vacancies can be introduced by the incorporation of aliovalent cations (Re_2O_3) to the lattice of the fluorite oxide system. Kilner and Steele have extensively reviewed the parameters of eq. 3.1

$$\sigma T = A^{\left(-\frac{Ea}{kT}\right)} \qquad (eq.3.1)$$

where σ ionic conductivity, A is a pre-exponential term, and E_a is the activation energy, concluding that the concentration of free vacancies is function of temperature and is difficult to select optimal dopant concentration. Although thermodynamic investigations suggested that at intermediate temperatures it becomes easier the reduction of Ce^{+3} to Ce^{+4} as the concentration of Re_2O_3 is increased.

The activation energy is equal to the sum of enthalpy of motion ΔH_m and enthalpy of association ΔH_a. For intermediate temperatures ΔH_a should be as small as possible, and Butler et al. [7] suggested that the association values can be correlated with the ionic radii of the dopant ions (Gd^{+3}, Sm^{+3}, Y^{+3}). The minimum value for ΔH_a is observed when the radius of the dopant is closely to Ce^{+4}. Taking in account critical radii for which the volume of the host lattice is not influenced, Gd^{+3} seems to be the most ideal dopant.

There is an extensive investigation in literature regarding the different concentration of Gd^{+3} in CeO_2 lattice. According to Steele [3] one of the main effects of the percentage of dopant that is used, is its contribution to the grain boundary conductivity. Impurities, and especially SiO_2, are unavoidable since they can be introduced very easily to the electrolyte matrix during processing and particularly from furnace refractories during high-temperature sintering. Contamination with impurities causes a decrease to the ionic conductivity in the grain boundaries. Impurities may also segregate to electrode-electrolyte three-phase boundary regions and increase the effective electrode resistance. Comparison of impure $Ce_{0.9}Gd_{0.1}O_{2-\delta}$ (CGO10) and $Ce_{0.8}Gd_{0.2}O_{2-\delta}$ (CGO20) revealed that CGO20 has higher grain boundary conductivity [3]. Although the lattice conductivity is higher for pure CGO10, and an intrinsic grain boundary contribution can not be detected above 500^{o}C.

Kharton et al., [1] reported for CGO10 better stability in reducing atmospheres with respect to CGO20 at atmospheres below ~730°C making CGO10 more appropriate for IT-SOFC application. However Kharton et al., [1] suggested that the incorporation of small amounts of praseodymium oxide into CGO20 might improve its stability in reduced oxygen pressures, but the difference between electrolytic domain boundaries of the praseodymium oxide incorporated in CGO20 and CGO10 were insignificant.

3.4 Synthesis of $Ce_{0.9}Gd_{0.1}O_{2-\delta}$ and characterization.

Different synthesis routes lead to different powder characteristics such as particle size, particle size distribution, shape, state of agglomeration, and chemical composition. In literature there is a variety of different synthesis routes in for the fabrication of CGO10.

C. C. Chen et al., [18] prepared $Ce_{0.8}Sm_{0.2}O_{2-\delta}$ thin films from polymeric precursors by using ethylene glycol and metal nitrates solutions. Ethylene glycol was oxidized by nitric acid and formed oxalic acid which reacted further with ethylene glycol and formed a polyester which chelated to a homogenous distribution of the required metal cations, and then spin-coated on the substrate. With this method C. C. Chen et al., [18] managed to prepare inexpensively a dense and crack-free ceramic thin film.

M. Greenblatt et al., [20] also examined the properties of $Ce_{1-x}Sm_xO_{2-x/2}$ (x=0-0.30) solid electrolytes prepared with a different sol-gel method than C. C. Chen et al., [18]. The appropriate quantities of starting materials coprecipitated with ammonium hydroxide at pH=10, after being dissolved separately in water. The precipitation was controlled by addition of HNO_3, and the transformation from sol-to-gel occurred over a period of 1-2 days. After heat treatment at 1000°C the crystallite size that they obtained was varying between 24 and 40 nm, depending on the concentration of Sm. Due to the small crystallite size the sintering temperature reduced to 1400°C from 1650°C which is required for the corresponding materials prepared by conventional solid state methods.

T. J. Huang et al., [21] managed to sinter samaria doped ceria electrolyte at 1300°C by a modified sol-gel method achieving 98% relative density. According to Readey et al., [22] the sintering behavior is very sensitive to the gel dealing solvent, since hard agglomerates might form when the precipitated gels are washed with water, or on the contrary very soft agglomerates might be formed when the gels are washed with ethanol. T. J. Huang et al., [21] concluding that that the agglomerate strength is the dominant factor for the final sintering density, they claimed that by washing the precipitated gel with octanol prevents interaction between particles and in that manner inhibiting the formation of hard agglomerates and thus soft agglomerates are formed leading to very high relative density values after sintering even at 1300°C.

K. Huang et al., [19] used a sol-gel process similar to C. C. Chen et al., [18] in order to synthesize dense $Ce_{0.9}Gd_{0.1}O_{2-\delta}$ and compared it with sample prepared with the conventional ceramic method. Pellets prepared with the later method exhibited pores, and the grain size was between 1-5 μm, making ball milling unavoidable, in order to break up the interpenetrating network of grains and pores, in order to achieve a dense ceramic. On the contrary, powder which produced with the sol-gel method yields more spherical particles, with average diameter of 0.25 μm. The product was calcined at 700°C, and then sintered at 1586°C for 6 hr exhibiting relative density 99%.

Ji_Guang Li et al., [24] fabricated nanocrystalline CeO_2 via carbonate precipitation method, using ammonium carbonate as the precipitant and cerium nitrate hexahydrate as the cerium source. They reported that the molar ratio of ammonium carbonate:Ce^{+3} affects significantly the precursor properties and spherical nanoparticles can be produced only when the range of molar ratio is between 2 and 3. In that manner they proved that the importance of precipitant, in order to obtain nanosized and spherical particles, since using the same method but urea as precipitant neither nanosized nor spherical particles are obtained [25], [26]. A. I. Y. Tok et al., [27] used the same method, and as a dopant Gadolinia nitrate with the molar ratio between ammonium carbonate and Ce^{+3}/Cd^{+3} being 2.5 they were able to obtain spherical nanoparticles.

J. Van Herle et al., [23] fabricated (Y, GD, Sm)-doped ceria electrolytes with oxalate coprecipitation without any milling step, and obtaining pellets with 97% relative density sintered at 1300°C. They reported that the improved sintering characteristics of the resulting powder are due to the dewatering step with ethanol of the resulting precipitate. The obtained powders have average particle sizes of 0.5 to 0.7 μm without milling. Although their claim about avoiding the milling step should be reconsider since milling leads to narrower particle size distribution and uniform shape.

T.S Zhang et al., [17] prepared $Ce_{0.9}Gd_{0.1}O_{2-\delta}$ dense electrolytes by carbonate coprecipitation reporting that this route yields powders with weak agglomeration and uniform spherical particle shape. They also observed that the calcination temperature has a significant influence on the densification behavior and as well to the final relative density. They defined as optimal calcination temperature 800°C since below 700°C they observed an expansion at 1250°C during sintering. The powders that calcined at 800°C for 2 hr have a mean crystallite size of 25 nm with spherical and narrow size distribution. Addition of $Fe(NO_3)$•9H2O 0.5 at% into the calcined powders via wet chemical method reduced the sintering temperature to 1200°C obtaining pellets with 98% relative density.

3.5 Sintering additives

Herring C. in 1950 in his publication regarding the effect of change of scale on sintering phenomena [8], defined as sintering any change in shape which a small particle of uniform composition undergoes when held at high temperature. When there is no external pressure such changes are driven by surface tension, since the surface free energy decreases as the particles grow together, and he suggested four scaling laws that govern the sintering process, among them was lattice diffusion. In a crystal the diffusive flux of matter is proportional to the local gradient of the chemical potential of the diffusing substance. As pointed out by Jason D. Nicholas et al., [9] the increase of one of the terms of eq. 3.2 with the addition of dopants, in principle should lower the sintering temperature. Therefore, for small particle size, densification occurs primarily via grain-boundary diffusion.

$$J = MC\nabla\mu \qquad (eq.3.2)$$

Where J is the flux of atoms along the grain boundary, M is the atomic mobility along the grain boundary, C is the vacancy concentration, and μ is the gradient of chemical potential which is the driving force for sintering.

There are different sintering additives used through literature, and there is an extensive work done concerning the influence of Transition Metal Oxides (TMOs) to the sintering behavior of the electrolyte. The most effective one seems to be Fe_2O_3.

Kleinlogel C. and Gauckler L.J [10] investigated the addition of small amounts (1-5 mol-%) of Co, Cu, Mn, Fe and Ni oxides. With addition of Co, Cu, and Ni sintering was effective at all temperatures above 850°C whereas Fe and Mn-oxides were effective above 1050°C. Cobalt oxide addition as low as 0.5 mol-% exhibit effective densification and the rate of densification increased with the increase of the sintering aid concentration, although when the concentration was exceeding the 5 mol-% the shrinkage rate was reduced and densification was hindered.

Zhang T. S. et al., [11] reported that electrolytes without TMOs are more porous than those with TMOs and that even though the undoped are sintered at higher temperatures the doped ones exhibit larger grain size. In that manner addition of TMOs as sintering agents makes feasible the reduction of sintering temperature promoting densification and grain growth for Gadolinia doped Ceria electrolytes. They also reported that the addition of MnO_2 and Fe_2O_3 has only little effect on pure CGO20 grain boundary conductivity, where on the contrary a slight decrease was observed with the addition of cobalt oxide.

An interesting observation by Zhang T. S. et al [11] is that the addition of 0.5 at.% of Co or Mn oxide led to a further deterioration in the grain boundary conductivity of impure CGO20, where in contrast the grain boundary conductivity was improved with small addition of Fe_2O_3.

Impurities are unavoidable and the predominant constituent of the grain boundary region is SiO_2. As already mentioned above, impurities can be introduced during processing, and especially from furnace refactoring during the high temperature sintering, leading to low ionic conductivity in the grain boundary region. Zhang T. S. et al., in a later publication [12] reported that for SiO_2 contamination, CuO, CoO or MnO_2 are unsuitable as sintering additives, since they promote the propagation of SiO_2 at the grain boundaries. On the contrary Fe_2O_3 can be used more effectively as a sintering aid since it can function as a grain boundary scavenger and clean the grain boundaries from SiO_2 impurities, and in that manner improving the grain boundary conductivity.

Apart from TMOs other metals such as Li^{+}, Al^{+3}, and Bi^{+3} have been used as sintering agents. Joon-sin Lee et al., [13] investigated the effects of alumina addition on sintering behavior of Gadolinia doped Ceria electrolyte, where they reported that both sintered density and grain size increased with increasing Al_2O_3 content up to 2 mol-% and decreased with Al_2O_3 content above 3 mol-%. Indicating that Al_2O_3 additions within the solubility limit (2 mol-%) accelerated the densification remarkably and promote the grain boundary mobility, although there where no indication about the sintering temperature and no electrochemical data regarding the ionic conductivity of the electrolyte.

V. Gil et al., [14] investigated the effect of small amount (0.2-2.0 wt. %) of Bi_2O_3 on the sintering behavior and microstructural development of commercial CGO10. They observed a reduction of sintering temperature in the order of 250-300^{o}C compared to the undoped CGO10, and an increase of the average grain size of the doped CGO10 samples when they where doped with up to 1.0 wt. %. Although the sintering temperature still remained relatively high (1400^{o}C) .

J.D. Nicholas and L. C De Jonghe [9] reported a record-low sintering temperature (800^{o}C) when they added 3 mol-% of lithium as a sintering agent. They introduced the use of Vegard's slope as a tool for the prediction and evaluation of sintering agents for Gadolinia doped Ceria electrolytes. Claiming that using Vegard's slope, eq. 3.3.

$$X = (0.0220 r_i + 0.00015 z_i) \qquad (eq.3.3)$$

where r_i is the difference in ionic radii between the sintering agent and Ce^{+4} in 8-fold coordination, and z_i is the difference in charge between the sintering agent and Ce^{+4} , it should be possible to identify which sintering agent could be used in order to achieve low sintering temperatures. Indeed, the solubility of a sintering agent in CGO is inversely proportional to the square of its "Vegard's Slope", therefore the effectiveness of a sintering agent is a matter of forming a beneficial second phase and/or its ability to improve the CGO near grain boundary atomic flux.

3.6 Electrochemical properties

The efficiency of an electrolyte used in SOFC stacks is determined by the amount of oxygen ion conductivity. B. C. H. Steele [5] reported that for most applications, oxygen ion conductivities greater than 10^{-1} S cm^{-1} are required for IT-SOFC. The electrical transport behavior of CGO is described by eq. 3.1, B. C. H. Steele in a later publication [3] compared the ionic conductivity of CGO10, CGO20, Ce0.9Sm0.1O2-δ, and $Ce_{0.9}Y_{0.1}O_{2-\delta}$, in three different temperatures 500°C, 600°C and 700°C, observing that at 500°C CGO10 yields the highest ionic conductivity and for the temperatures of 6000C 700°C the highest ionic conductivities is being obtained by $Ce_{0.9}Y_{0.1}O_{2-\delta}$.

Table 3.2 Ionic Conductivity for selected electrolyte compositions [3]

Composition	*σ, 500°C (S cm⁻¹)*	*σ, 600°C (S cm⁻¹)*	*σ, 700°C (S cm⁻¹)*
$Ce_{0.9}Gd_{0.1}O_{2-\delta}$	*0.0095*	*0.0253*	*0.0544*
$Ce_{0.9}Sm_{0.1}O_{2-\delta}$	*0.003*	*0.0090*	*0.0200*
$Ce_{0.9}Y_{0.1}O_{2-\delta}$	*0.0087*	*0.0344*	*0.1015*
$Ce_{0.8}Gd_{0.2}O_{2-\delta}$	*0.0053*	*0.0180*	*0.0470*

Kleinlogel C. and Gauckler L.J [15] investigated the electrochemical properties of nanosized ceria solid solutions by adding small amounts (<5 mol-%) of Co_3O_4. They did not obtain any Co_3O_4 rich grain boundary layer which might block ionic conduction, although when they varied the $p(O_2)$ they observed that for lower values of $p(O_2)$ the material becomes a mixed ionic-electronic conductor due to partial reduction of Ce^{+4} to Ce^{+3}.

D. P. Fagg et al., [16] investigated the effect of TMOs in p-type electronic transport in CGO and concluded that CGO containing small amounts (~2 mol-%) of Cu, Co and Fe oxides exhibit similar conductivity values with pure CGO. In later publication T. S. Zhang et al., [11] reported that the additions of Fe and Mn oxide had very small effect on the grain boundary behavior while the addition of Co oxide exhibited a slight decrease in the grain boundary conductivity compared to pure CGO, indicating as well a small decrease in the lattice conductivity, probably due to the dissolution of TMOs in CGO crystallites.

T. S. Zhang et al., [17] performed impedance measurements on CGO10 loaded and unloaded with Fe_2O_3 0.5 at. % and reported that, with the addition of iron (III) oxide the grain boundary arc much smaller that that from the unloaded CGO10 (figure 3.1). Unloaded CGO10 exhibits smaller grain boundary conductivity because of SiO_2 impurities forming a thin layer on the grain boundaries prohibiting the oxygen ionic transport. On the contrary CGO10 loaded with Fe_2O_3 exhibits smaller grain boundary arc, indicating higher grain boundary ionic conductivity, this result verifies their previous observation [11] of scavenging effect on SiO_2 of Fe_2O_3. Additionally the addition of the iron (III)

oxide has no effect on the lattice conductivity, since the arc for both loaded and unloaded CGO10 are identical, and this is due to the very low solubility of Fe_2O_3 in ceria-based solid solutions.

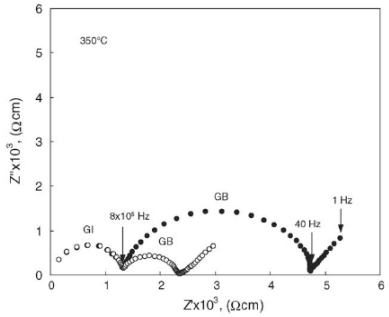

Figure 3.3. Impedance spectra taken at 350^0C in air (•) unloaded and (○) loaded with 0.5 at. % Fe_2O_3 [17].

3.7 Conclusions

CGO 10 seems to be the most promising electrolyte for IT-SOFC. The ionic radii of Gd^{+3} is closer to the ionic radii of Ce^{+4} keeping in that manner the enthalpy of association ΔH_α as small as possible hence the activation energy low. CGO 10 according to Steele [3] performs better electrochemically with respect to CGO 20, revealing higher lattice ionic conductivity, and better stability in reducing atmospheres below 730°C according to Kharton [1].

Regarding sintering agents, the use of lithium oxide seems tempting, however lithium is quite volatile. On the other hand, since impurities are unavoidable, the scavenging properties of iron make it the most practical agent for use with respect to the rest TMOs. Different iron concentrations have been tested, where 0.5 a.t. % and 1 a.t % revealed the best results, and this is because when iron exceeds 1 a.t %, an increase to the electronic conductivity was observed [17]. In that manner for the purpose of this project, the use of gadolinia as a dopant with ratio Ce:Gd=0.9:0.1 and iron 0.5 at% was chosen.

References

[1] V. V. Kharton, F. M. Figueiredo, L. Navaro, E. N. Naumovich, V. Kovalevsky, A. A. Yaremchenko, A. P. Viskup, A. Carneiro, F. M. B. Marques, J. R. Frade, *Journal of Materials Science* **36** (2001) 1105-117.

[2] B.C.H Steele, *Journal of Materials Science* **36** (2001) 1053-1068.
129
[3] B.C.H Steele, *Solid State Ionics* **129** (2000) 95-110

[4] M. Sahibzada, B.C.H Steele, K. Zheng, R.A Rudkin, I.S Metlcalfe, *Catalysis Today* **38** (1997) 459-466

[5] B.C.H Steele, *Materials Science and Engineering*, **B13** (1992) 79-87

[6] B.C.H Steele, *Br Ceram. Proc.* **56** (1996) 151

[7] V. Butler, C.R.A Catlow, B.E.F Fender, J.H. Harding, *Solid State Ionics* **8** (1983)

[8] Herring C. *Journal of Applied Physics*, **21** (1950) 301-303

[9] Jason D. Nicholas, Lutgard C. De Jonhe, *Solid State Ionics,* **178** (2007) 1187-1194

[10] C. Kleinlogel, L. J. Gauckler, *Advanced Materials,* 13 **14** (2001) 1081-1085

[11] T. S. Zhang, J. Ma, Y.J. Leng, S. H. Chan, P. Hing, J. A. Kilner, *Solid State Ionics,* **168** (2004) 187-195

[12] T. S. Zhang, J. Ma, Y.J. Leng, Z. M. He, *Journal of Crystal Growth,* **274** (2005) 603-611

[13] Joon-Sin Lee, Kwang-Hoon Choi, Bong-Ki Ryu, Byoung-Chul Shin, Il-soo Kim, *Ceramics International,* **30** (2004) 807-812

[14] V. Gil, J. Tartaj, C. Moure, P. Duran, *Journal of the European Ceramic Society,* **27** (2007) 801-805

[15] C. Kleinlogel, L. J. Gauckler, *Solid State Ionics,* **135** (2000) 567-573

[16] D. P. Fagg, V. V. Kharton, J. R. Frade, *Journal of Electroceramics,* **9** (2002) 199-207

[17] T. S. Zhang, J. Ma, L. H. Luo, S. H. Chan, *Journal of Alloys and Compounds,* **422** (2006) 46-52

[18] C.C Chen, M. M. Narsallah, H. U. Anderson, *J. Electrochem. Soc.,* **140** (1993) 3555-3560

[19] K. Huang, M. Feng, J. B. Goodenough, *J. Am. Ceram. Soc.,* **81** (1998) 357-362

[20] W. Huang, P. Shunk, M. Greenblatt, *Solid State Ionics,* **100** (1997) 23-27

[21] G. B. Jung, T. J. Huang, M. H. Huang, C. L. Chang, *Journal of Materials Science,* **36** (2001) 5839-5844

[22] M. J. Readey, R. R. Lee, J. W. Halloran, A.H. Heuer, *J. Amer. Ceram. Soc.* **73** (1990) 1499-1503

[23] J. Van Herle, T. Horita, T. Kawada, N Skai, H. Yokokawa, M. Dokiya, *Solid State Ionics,* **86-88** (1996) 1255-1258

[24] Ji-Guang Li, Takayasu Ikegami, Yarong Wang, Toshiyuki Mori, *J. Am. Ceram. Soc.,* **85 (9)** (2002) 2376-2378

[25] E. Matijevic, W. P. Hsu, *J. Colloid Interface Sci.,* **118 (2)** (1987) 507-523

[26] M. Akinc, D. Sordelet, *Adv. Ceram. Mater.,* **2 (3A)** (1987) 232-238

[27] A. I. Y. Tok, L. H. Luo, F. Y. C. Boey, *Materials Science and Engineering A,* **383** (2004) 229-234

Experimental Part

Chapter 4-Preperation of powders and pellets

4.1 Introduction

The present project is focusing on the development of gadolinia doped ceria electrolyte used in SOFC. For the achievement of this goal, three different synthesis routes were tested, and from each route, three different pellets fabricated. One pellet composed from pure ceria and gadolinia without the addition of any sintering agent, one with the addition of iron oxide as sintering agent with ball milling, and one with the addition of iron nitrate *"in situ"* during the synthesis of gadolinia doped ceria electrolyte.

4.2 Citrate route

For the preparation of the raw powder with the citrate coprecipitation route, high purity (99.5%) $Ce(NO_3)_3 \cdot 6H_2O$ and $Gd(NO_3)_3 \cdot 6H_2O$ were used, supplied from Alfa Aesar. As coprecipitation medium citric acid was used. The preparation procedure is described schematically in figure 4.1. $Ce(NO_3)_3 \cdot 6H_2O$ and $Gd(NO_3)_3 \cdot 6H_2O$ 0.8M and 0.09M respectively, were dissolved in distilled water with the addition of 1.45M of citric acid. For the *"in situ"* addition of iron as a sintering agent, 0.07 grams of $Fe(NO_3)_3 \cdot 9H_2O$ were added at this stage.

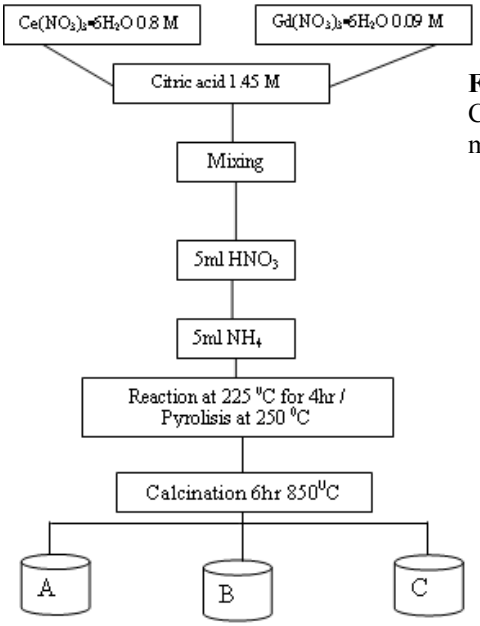

Figure 4.4 Citrate route. A: Pure CGO 10, B: 0.5 Fe at % with ball milling, C: 0.5 Fe at. % *"in situ"*

The mixture of nitrates and citric acid was dissolved in 5ml of HNO_3 the pH of the solution was regulated with the addition of 5 ml of NH_4OH dropwise. The reaction took place for ~4 hr at 225°C, the obtained material was pyrolized at 250°C, and then calcined for 6 hr at 850°C. The obtained product was ball milled and then pressed into pellets, using uniaxial and isostatic press. For the pellets in which iron(III) oxide used as a sintering agent, after ball milling 0.5 at% of Fe_2O_3 was added via ball milling.

4.3 Complexation

Two modified complexation routes were tested, one with low concentration of ceria and gadolinia nitrates, and one with high. For both of the routes the effect of addition of HNO3 was examined.

4.3.1 Complexation Low Concentration

Figure 4.3 describes schematically two different routes, with and without the addition of HNO_3. The starting materials, 0.62M of $Ce(NO_3)_3 \cdot 6H_2O$ and 0.07M of $Gd(NO_3)_3 \cdot 6H_2O$ were mixed in molar ratio Ce:Gd=0.9:0.1 with 40ml ethylene glycol and 10 ml HNO_3 (in the case where HNO_3 was used) using water as a solvent. The reaction took place over night at 80°C, the obtained viscous solution was dried at 130°C. Drying time depends on the addition or no of HNO_3. When HNO_3 is added, it oxidizes the ethylene glycol converting it to oxalic acid (figure4.2) and the formed polyester allows homogenous chelation of metal ions. In that manner, there is an amount of cross-linking in the polymeric precursor. The drying time for the precursor is ~12hr, while on the contrary when HNO_3 is not added the drying time is ~3-4hr. For the pellets that are prepared with the *"in situ"* method, the sintering agent was added in the first step with the nitrates.

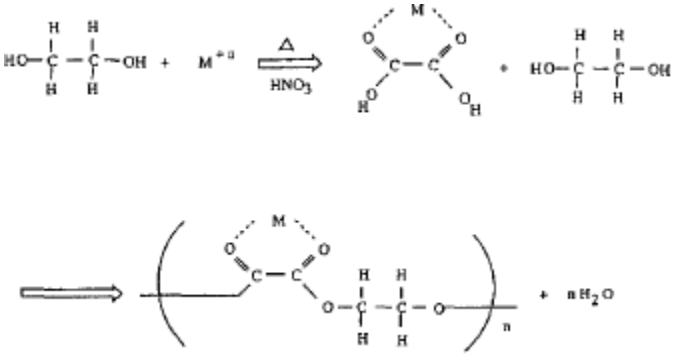

Figure 4.5 Reaction Mechanism for ethylene glycol with HNO_3

After drying, the obtained material was grinded and then calcined for 6hr at 700°C. After the calcination step the powders were ball milled, with an additional ball milling step for the pellets in which Fe_2O_3 was incorporated. For the fabrication of the pellets, a uniaxial and an isostatic press were used.

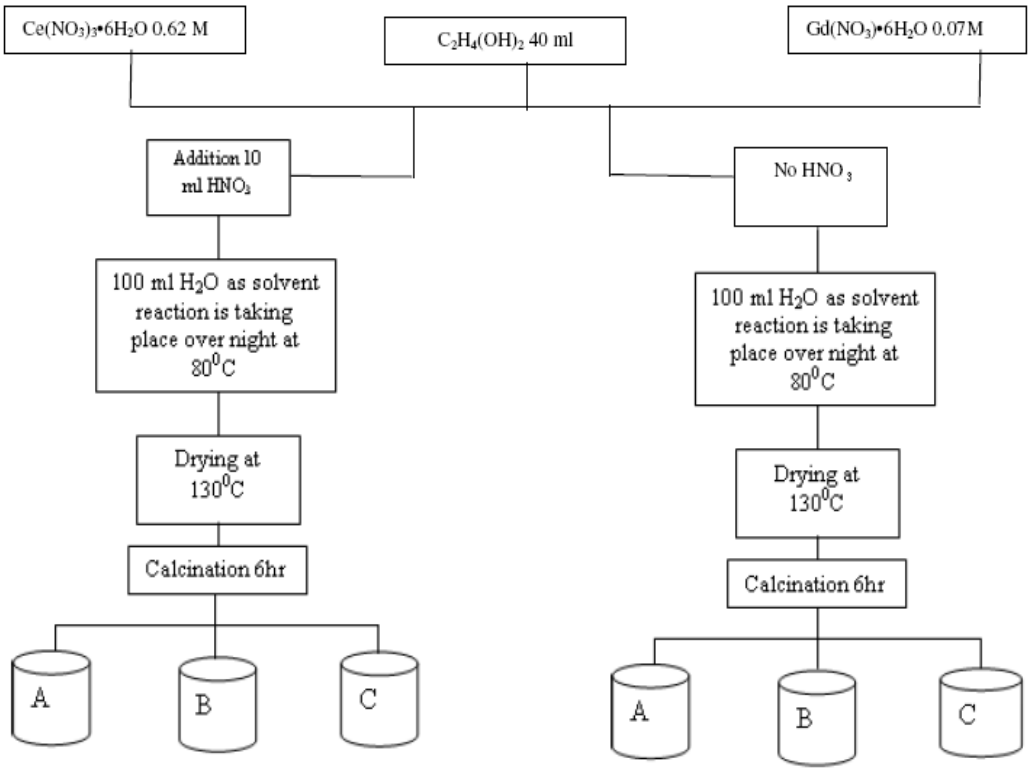

Figure 4.3 . Complexation Low Concentration A: Pure CGO 10, B: 0.5 Fe at % with ball milling, C: 0.5 Fe at. % *"in situ"*

4.3.2 Complexation High Concentration

In the high concentration complexation route (figure 4.4), the concentration of $Ce(NO_3)_3•6H_2O$ and $Gd(NO_3)_3•6H_2O$ increased by a factor of 3. Due to the increase of the concentration of nitrates during the drying process ignition occurred burning all the carbonates and impurities according to the TGA graph (figure 4.5) indicating that the calcination step can be avoided. However, because of the difficulty to control the ignition process during drying pellets with *"in situ"* incorporation of iron were not fabricated. Pellets of pure CGO 10 and pellets with the addition of Fe_2O_3 prepared as previously.

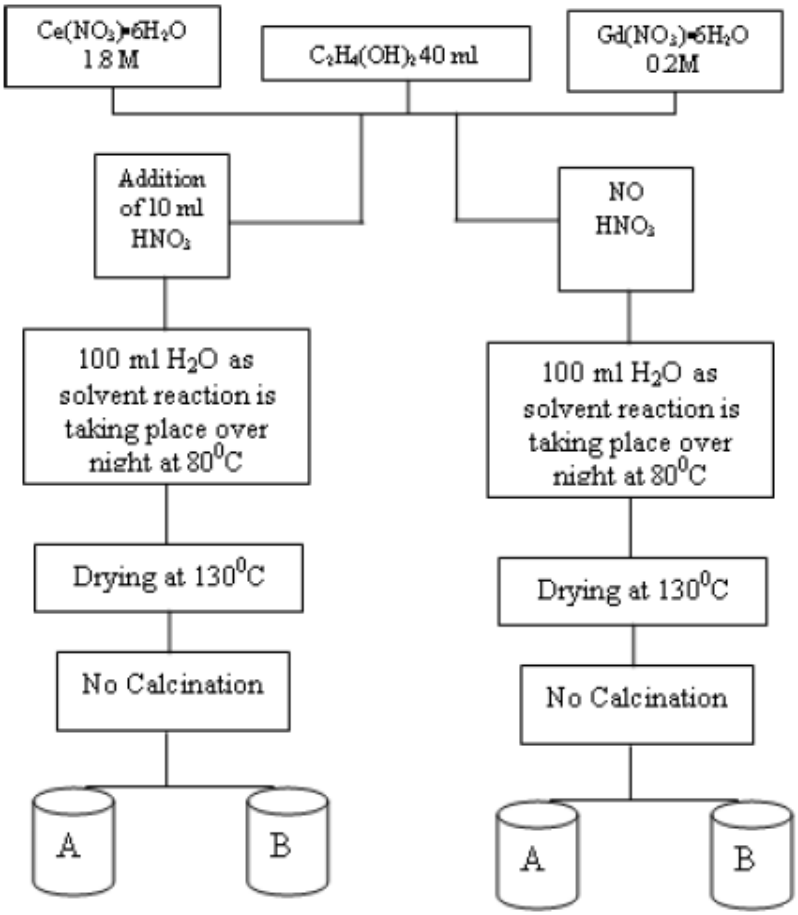

Figure 4.4 Complexation High Concentration A: Pure CGO 10, B: 0.5 Fe at % with ball milling, C: 0.5 Fe at. % *"in situ"*

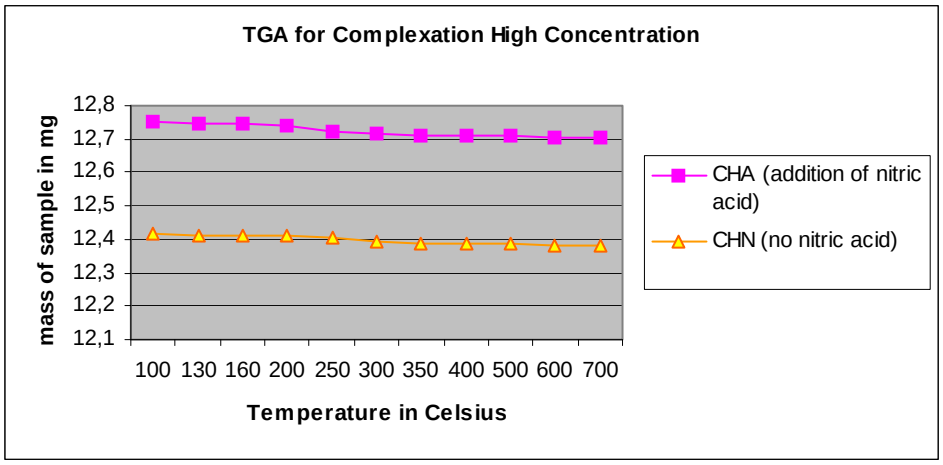

Figure 4.5 TGA for the Complexation route with high concentration of $Ce(NO_3)_3 \cdot 6H_2O$ and $Gd(NO_3)_3 \cdot 6H_2O$. CHA stands for Complexation High Concentration Addition of HNO_3, CHN stands for Complexation High Concentration No HNO_3

4.4 Nomenclature

Due to the large amount of pellets that have been prepared each pellet was named after the synthesis routes and the addition or not of iron. Therefore, for the citrate route the pellets have the code name CR (**C**itrate **R**oute). In the same manner, pellets prepared via the Complexation Low concentration method with the addition of HNO_3 are identified as CLA (**C**omplexation **L**ow concentration **A**ddition of HNO_3). If HNO_3 is not added then N (**N**o HNO3) replaces A, in this case pellets are identified as CLN. Similarly, H (**H**igh concentration of nitrates) replaces L when the synthesis route is the Complexation High Concentration method. Letters A, B, or C after the underscore bar indicate the addition and the way of addition of iron. A is for pure CGO10, B is for CGO10 with 0.5 at.% of iron via ball milling, and C is when iron was introduced as a nitrate "in situ". Therefore, as an example, the code name CLN_C stands for pellet which was prepared with the **C**omplexation **L**ow concentration method with **N**o HNO_3, and the iron was introduced as a nitrate *"in situ"*.

4.5 Overview

A schematic overview of the three different routes with the code name of each pellet is depicted in figure 4.6.

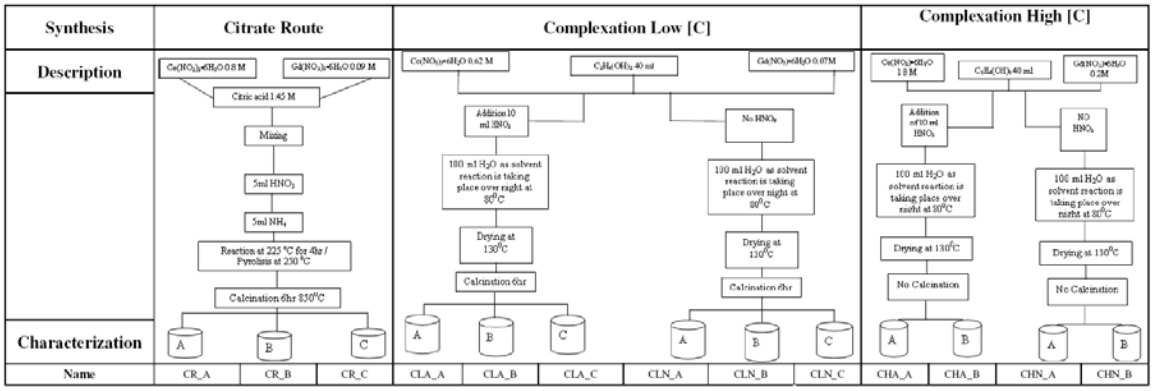

Figure 4.6 Synthesis Overview

Chapter 5- Characterization and Densification behavior

5.1 Introduction

The characterization of the crystal phase of the samples performed using x-ray diffraction (XRD) with Cu Kα radiation. The crystallite size calculated using Scherrer Equation (eq. 5.1) on the (111) and (220) diffraction peaks.

$$D = \frac{K\lambda}{B\cos\theta} \qquad (eq.5.1)$$

Where D is the crystallite size, λ the x-ray wavelength, B the full width at half maximum (FWHM) of the diffraction peak, θ the diffraction angle, and K is the Scherrer's constant. FWHM includes errors originated from noises and the apparatus conditions, such as the slit width of the x-ray diffractometer.

The distribution and the size of the particles of the powders were calculated using laser diffraction (Mastersizer 2000 Malvern). The morphology of the samples and the degree of densification was observed under scanning electron microscopy (SEM), and the mean grain diameter calculated with the intersect method [7] from the SEM pictures. The relative density of the pellets was calculated using Archimedes method in water.

5.2 Powders and pellets prepared with the Citrate Route

5.2.1 Characterization

The crystal phase has been analyzed by XRD after calcination at 850°C for 6hr. In figure 5.1 the XRD pattern of pellet prepared with the citrate route is depicted confirming the fluorite structure of the powder.

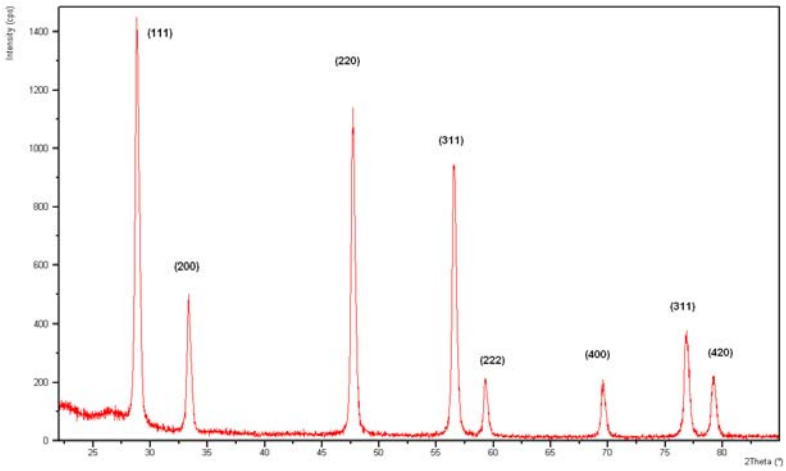

Figure 5.1 XRD diffractogram of CGO10 prepared with the citrate route at 850^0C

When 0.5 at % of iron added *"in situ"* in the material, no significant shift observed in the diffractogram as it is depicted in figure 5.2, without any second phase of iron being apparent.

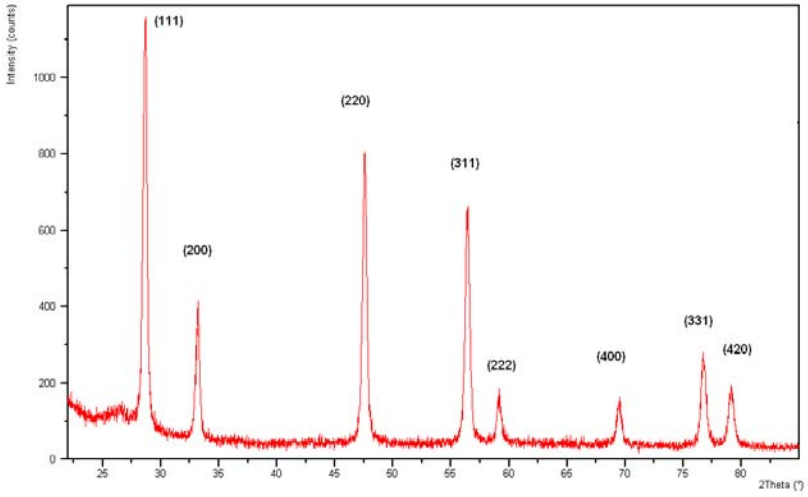

Figure 5.2 XRD diffractogram of CGO10 0.5 at % Fe *"in situ"* prepared with the citrate route at 850^0C

However according to Winnubst et. al, [1] when iron is introduced by ball milling no second phase will be shown in the diffractogram since the amount of iron is too small to be detected by means of x-ray diffractometry. This might explain the absence of iron introduced *"in situ"* in the material from the diffractogram. Table 5.1 gives the crystallite size D of the powders using Scherrer's formula and the mean particle size D_p calculated with laser diffraction.

Laser diffraction measurements for both powders with pure CGO10 and those in which iron introduced *"in situ"* made before milling. Figure 5.3 shows that there is a narrower particle size distribution with smaller mean particle size, for the powder in which iron introduced via ball milling, as it is expected due to the ball milling step.

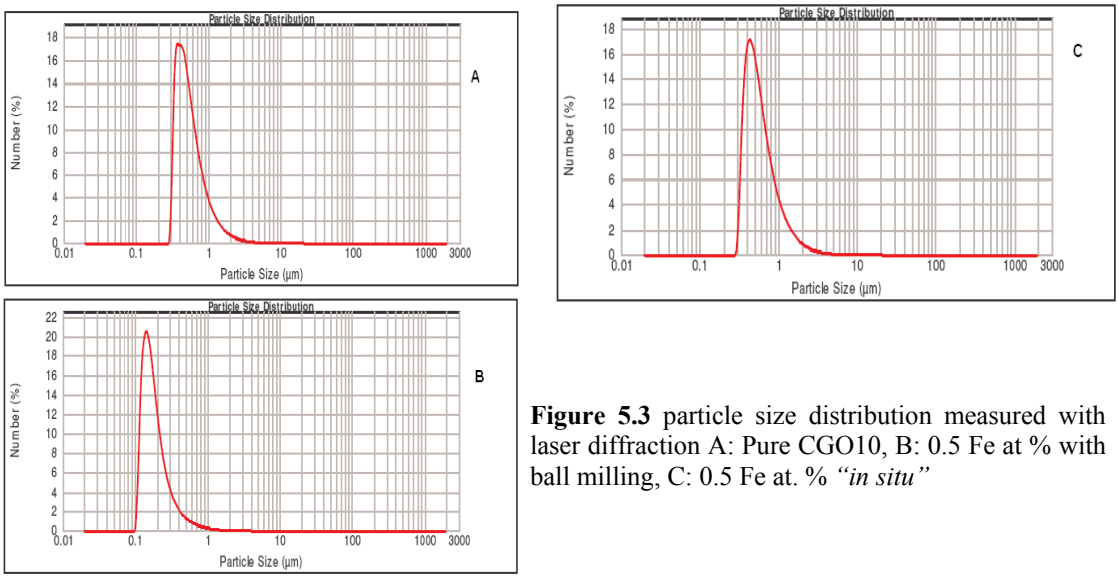

Figure 5.3 particle size distribution measured with laser diffraction A: Pure CGO10, B: 0.5 Fe at % with ball milling, C: 0.5 Fe at. % *"in situ"*

5.2.2 Densification Behavior

Previous studies indicated that small amounts (usually <2 wt%) of Fe_2O_3 are effective in promoting densification of gadolinia doped ceria electrolytes [2]. On the contrary, loading the samples with more than 2 wt. % is ineffective, due to an increase in electronic conductivity [3].

In figure 5.4 the relative density as function of temperature is plotted. The comparison between the three pellets reveals that iron has a significant influence on the densification rate. When iron is added pellets are dense at lower temperature with higher rate.

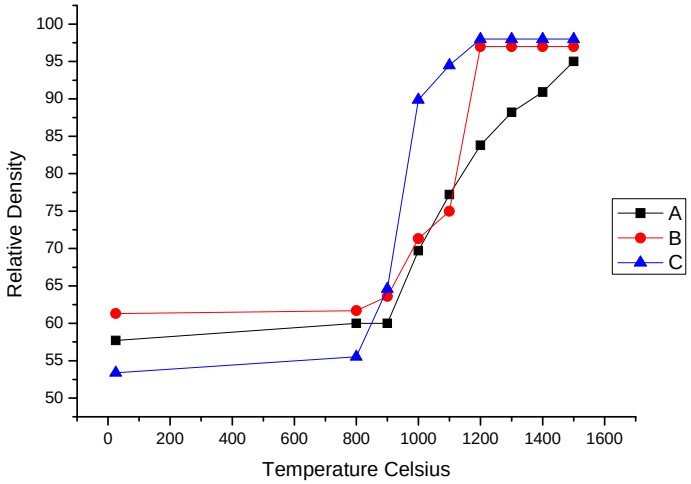

Figure 5.4 Relative density vs. sintering temperature. A: Pure CGO10, B: 0.5 Fe at % with ball milling, C: 0.5 Fe at. % *"in situ"*

When iron is added *"in situ"* pellets started sintering at lower temperature (800°C), and approximately with the same rate as when iron was added by ball milling. Pellets prepared with the *"in situ"* method had relative density 98%, calculated with Archimedes method in water, while pellets in which iron introduced by ball milling were 97% dense, both at 1200°C. Showing that when iron is introduced during the preparation of the powder using $Fe(NO_3)_3 \cdot 9H_2O$ affects positively the sintering behavior of the material. Pure CGO10 pellets were 95% dense at 1500°C, starting sintering above 900°C with lower rate than pellets in which iron was introduced.

The SEM pictures in figure 5.5 show the effect of sintering temperature on density and grain growth. For the samples in which iron introduced, nearly fully dense material can be obtained at 1200°C, whereas the pure CGO10 is more porous.

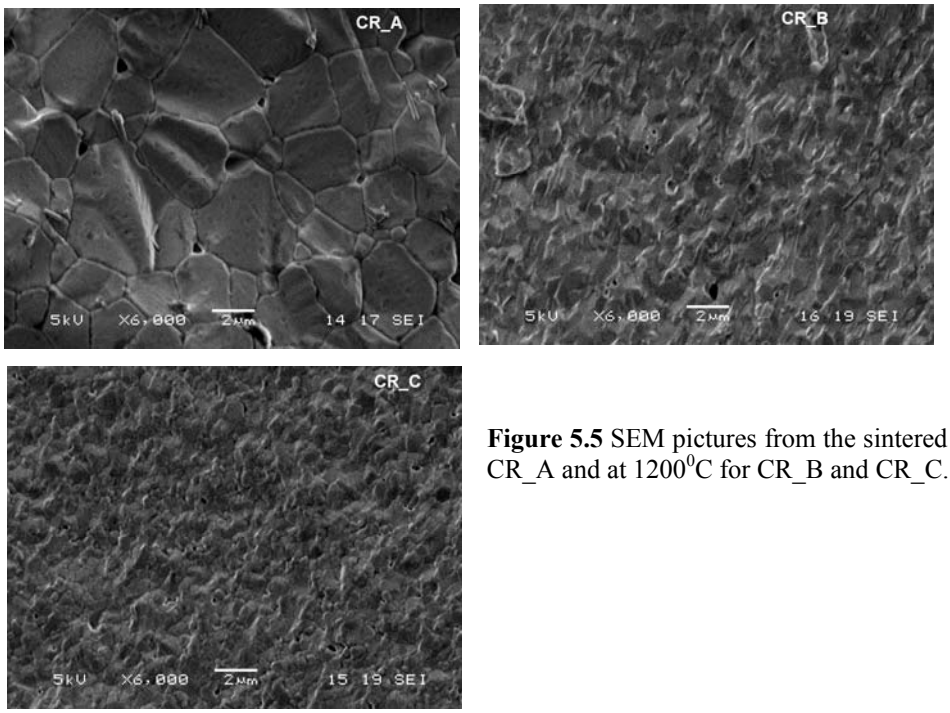

Figure 5.5 SEM pictures from the sintered pellets at 1500^0 for CR_A and at 1200^0C for CR_B and CR_C.

Table 5.1 Crystallite size D calculated using Scherrer's Formula, and the mean particle size D_p, and the grain diameter D_g after sintering

Composition	*D (nm)*	*D_p (µm)*	*D_g (µm)*
Pure CGO10	20	0.5	2.3
Addition 0.5 at % Fe with ball milling	20	0.14	0.45
"in situ" addition of 0.5 at % Fe	25	0.5	0.22

5.3 Powders and Pellets prepared with the Complexation Method Low Concentration

5.3.1 Addition of HNO_3-Characterization

As it is depicted in the XRD diffractogram of the powders prepared without the addition of HNO_3, broad peaks with low intensity observed indicating very small crystallite size, 7 nm (table 5.6) calculated with Schrerrer's formula.

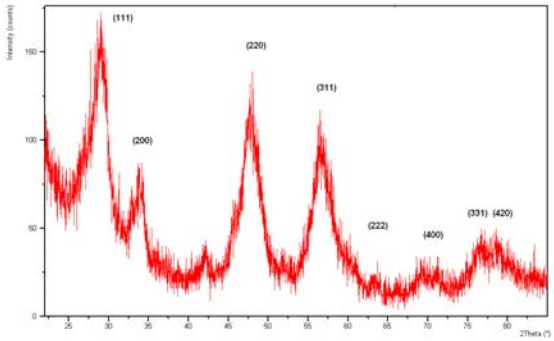

Figure 5.6 XRD diffractogram of CGO10 prepared with the addition of HNO_3 and calcined at 700^0C

On the contrary, higher intensities and narrower peaks obtained when the iron introduced *"in situ"* during the preparation of the powder. Figure 5.7 depicts the XRD diffractogram of the powder prepared with the addition of iron *"in situ"* and calcined at 700°C, being in accordance with the fluorite structure. The crystallite size of the powders was 13 nm.

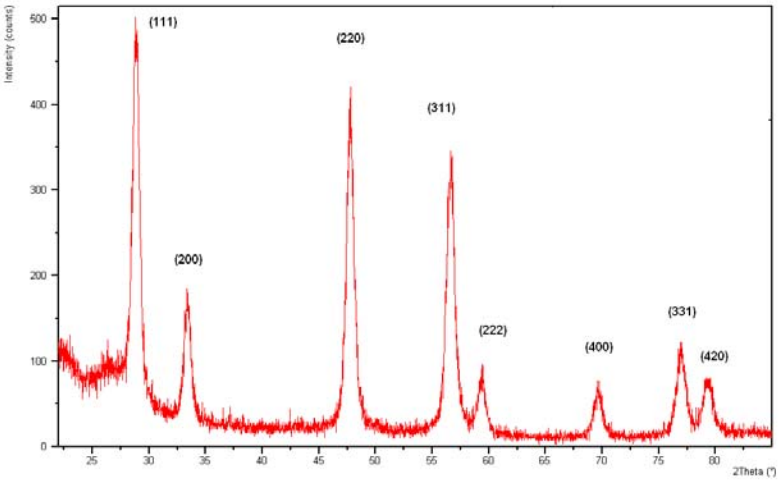

Figure 5.7 XRD diffractogram of CGO10 prepared with the addition of HNO_3 and "in situ" addition of 0.5 at% Fe, and calcined at 700^0C

Laser diffraction measurements (Figure5.8) revealed that all three powders prepared with the addition of HNO_3 have similar particle size distribution, with the powder in which iron introduced by ball milling having mean particle size of 0.18 μm. Which was expected due to the extra ball milling step

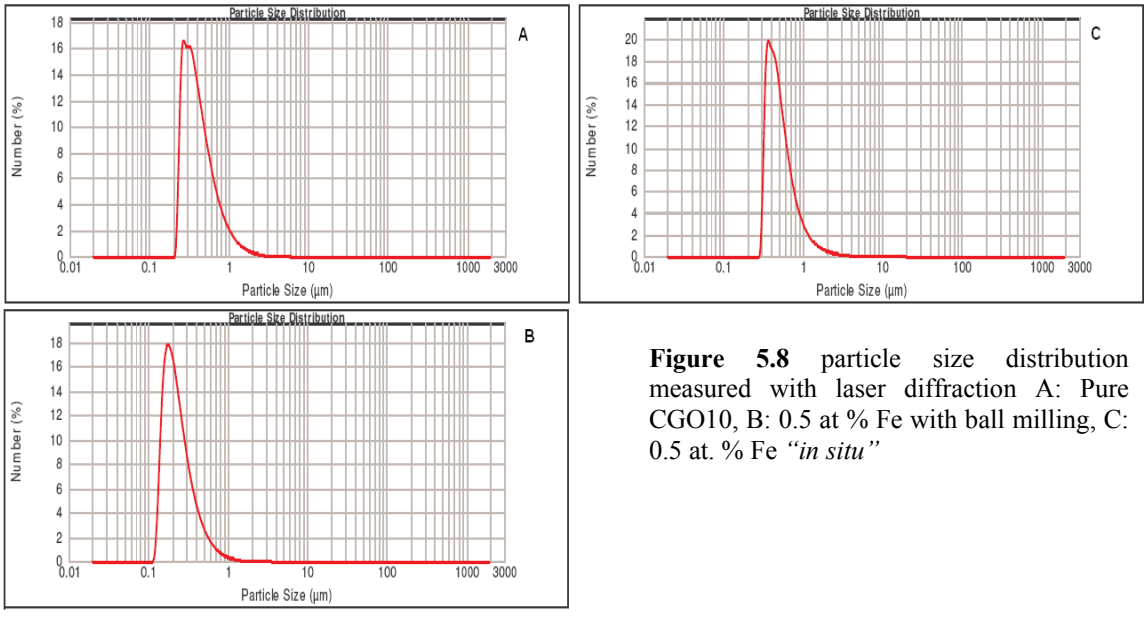

Figure 5.8 particle size distribution measured with laser diffraction A: Pure CGO10, B: 0.5 at % Fe with ball milling, C: 0.5 at. % Fe *"in situ"*

5.3.2 Addition of HNO_3- Densification Behavior

From the graph in figure 5.9 it can be seen that pure pellets and the ones in which iron was introduced via ball milling seem to start sintering faster than pellets which prepared with the *"in situ"* method, and below 1000°C they were ~95% dense. However, the pellets after sintering were cracked.
Cracks might be because of the uniaxial press during pressing introducing stresses locally. In that, manner particles aligned across one axes were more compact than the rest revealing an inhomogeneous distribution of stresses around the pellet. Indicating that the fabrication of thin films with this method is promising since high densities could be obtained at temperatures lower than 1000°C without the addition of a sintering agent.

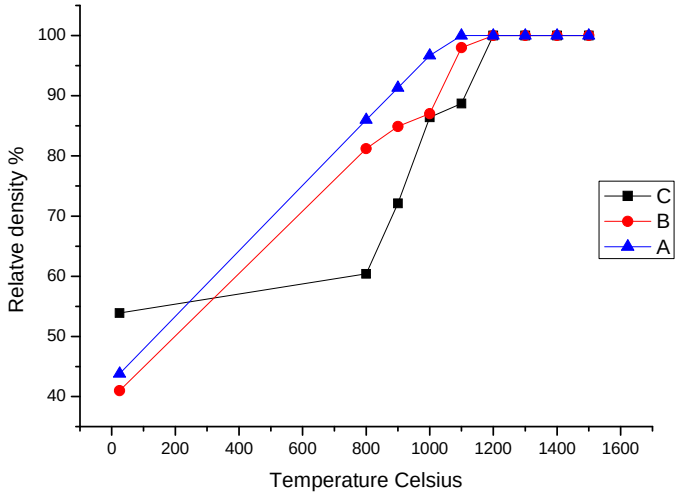

Figure 5.9 Relative density vs. sintering temperature. A: Pure CGO10, B: 0.5 Fe at % with ball milling, C: 0.5 Fe at. % *"in situ"*

When iron introduced *"in situ"* no cracks were observed after sintering, indicating that the bigger crystallites of the powder make pressing easier. The pellets started sintering at 800°C and at 1200°C they were 100% dense according the Archimedes Method.

SEM pictures were taken after thermal etching of the pellets focusing on the cross section. The SEM pictures in figure 5.10 verify the calculated high density of the material and the narrow grain size distribution with mean grain size of 0.4 μm and 0.46 μm for pure CGO10 and CGO10 with iron second phase introduced via ball milling respectively. A possible assumption that one could made from the comparison of the SEM pictures from figure 5.10 with the ones from figure 5.5, is that higher calcination temperatures might lead larger grains after sintering. Since the thermogravimetric analysis graph in figure 5.11 shows that above 250°C no significant change occurs to the weight of the powder,

indicating lower calcination temperature than 850°C which is used in the citrate route.

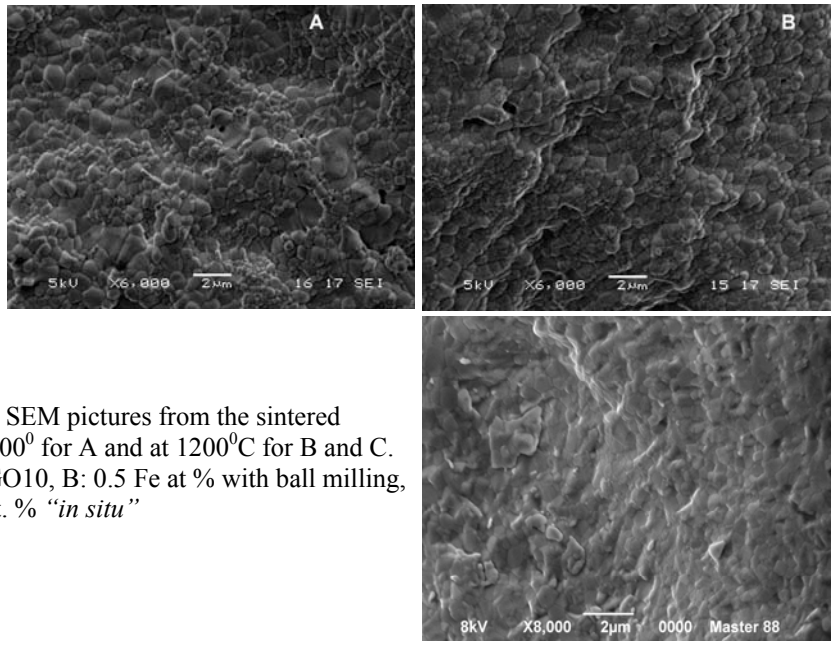

Figure 5.10 SEM pictures from the sintered pellets at 1300^0 for A and at 1200^0C for B and C. A: Pure CGO10, B: 0.5 Fe at % with ball milling, C: 0.5 Fe at. % *"in situ"*

Table 5.2 Crystallite size D calculated using Scherrer's Formula, and the mean particle size D_p, and the grain diameter D_g after sintering

Composition	*D (nm)*	*D_p (µm)*	*D_g (µm)*
Pure CGO10 (CLA_A)	7	0.5	0.4
Addition 0.5 at % Fe with ball milling (CLA_B)	6	0.18	0.46
"in situ" addition of 0.5 at % Fe (CLN_C)	13	0.4	0.45

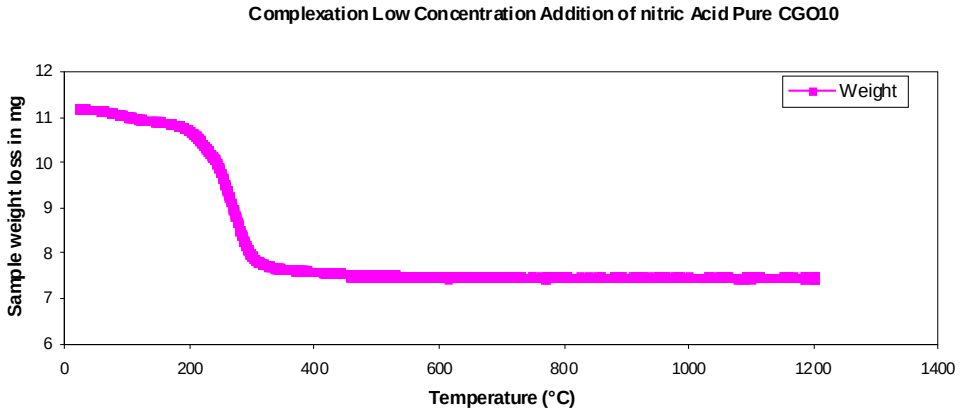

Figure 5.11 TGA for pure CGO10 powder prepared with the low complexation method without the addition HNO_3.

5.3.3 Without HNO3-Characterization

Comparison between XRD diffractogram of powders prepared without HNO_3 figure 5.12 and powders prepared with HNO_3 figure 5.6 reveal an effect of the HNO_3 on the crystal phase of the powder. However low intensities are observed and the crystallite size is slightly smaller, 5 nm.

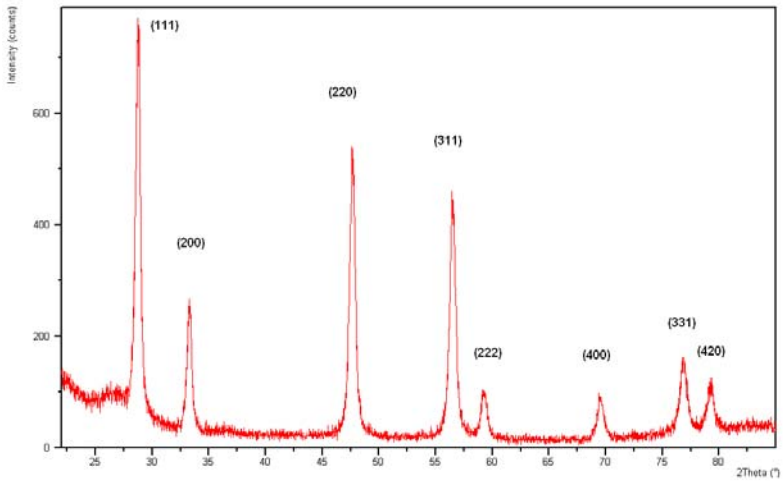

Figure 5.12 XRD diffractogram of CGO10 prepared without the addition of HNO_3 and calcined at 700^0C

On the contrary, when the powders prepared with the *"in situ"* method, the addition or not of HNO_3 does not seem to affect the crystallite size. The obtained powders from the *"in situ"* method without the addition of HNO_3 had the same crystallite size with the ones prepared with HNO_3, 13 nm. The XRD diffractogram in figure 5.13 confirms the fluorite structure of the material.

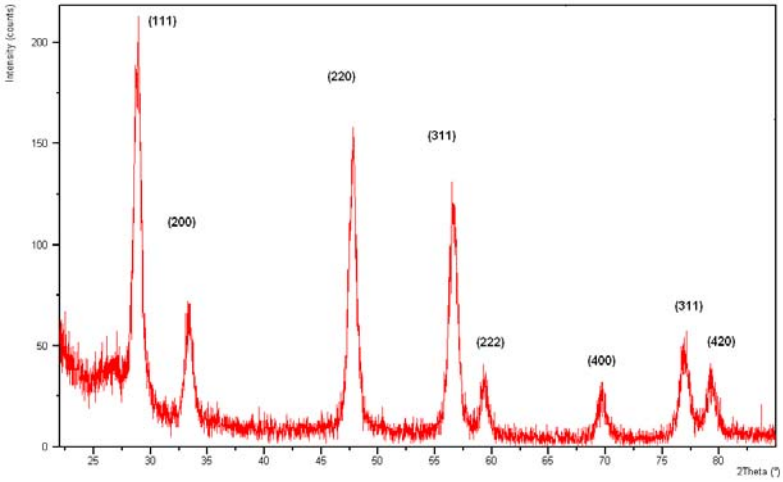

Figure 5.13 XRD diffractogram of CGO10 prepared without the addition of HNO_3 and "in situ" addition of 0.5 at.% Fe, calcined at 700^0C

Laser diffraction measurements revealed that the addition of HNO_3 might have a significant effect on the mean particle size of the powders. Especially in the cases of pure CGO10 and the one with the *"in situ"* addition of iron, the reduction in size of the mean particle size was more than 50%. As it is depicted in figure 5.14 narrower distributions of particle size achieved when HNO_3 was not used with respect when HNO_3 was used. The mean particle size for pure CGO10 was 0.2 μm, 0.12 μm for the powders with 0.5 at% Fe introduced via ball milling and 0.18 μm, for powders in which iron added with the *"in situ"* method (Table 5.3).

Table 5.3 Crystallite size D calculated using Scherrer's Formula, the mean particle size D_p, and the grain diameter D_g after sintering

Composition	*D (nm)*	*D_p (μm)*	*D_g (μm)*
Pure CGO10 (CLN_A)	5	0.2	0.38
Addition 0.5 at % Fe with ball milling (CLN_B)	5	0.12	<<0.38
"in situ" addition of 0.5 at % Fe (CLN_C)	13	0.18	<<0.38

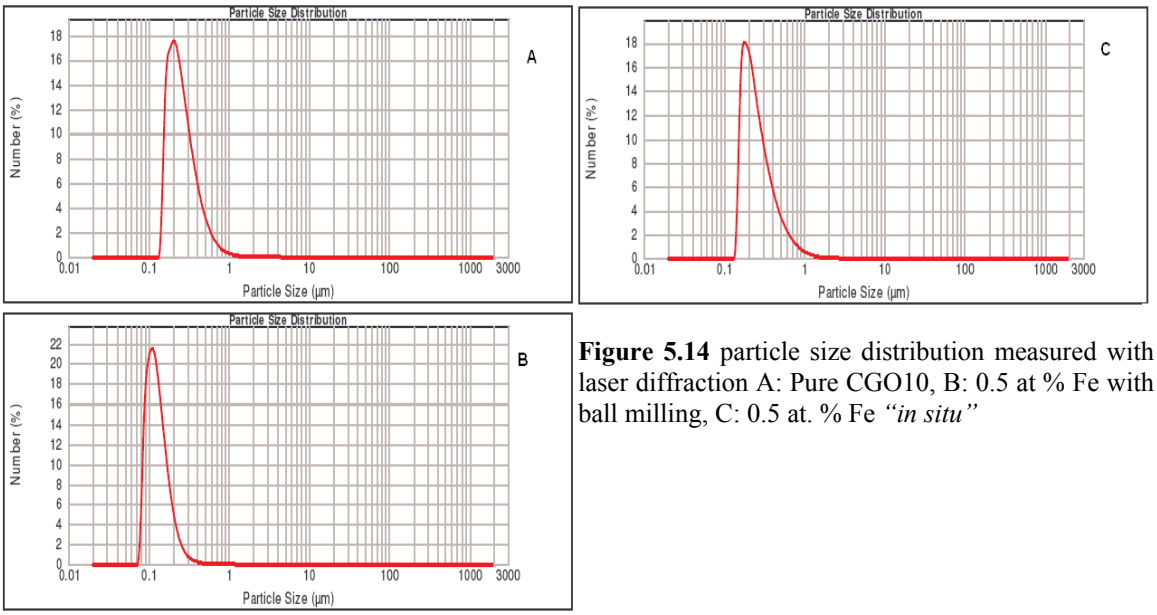

Figure 5.14 particle size distribution measured with laser diffraction A: Pure CGO10, B: 0.5 at % Fe with ball milling, C: 0.5 at. % Fe *"in situ"*

5.3.4 Without HNO3- Densification Behavior

When iron was added *"in situ"* the sintering temperature dropped down to 1100°C, a hundred degrees less from what is reported in literature up to date (see chapter 3), for the case in which iron is added as sintering agent. The densification behavior of the pellets prepared with three different routes is depicted in figure 5.15. All of them started sintering above 800°C, temperature much higher from the temperature in the case when HNO_3 was added, however all pellets after sintering did not reveal any cracks.

Comparison between pellets in which iron was incorporated via ball milling and *"in situ"* shows that when iron was incorporated as a nitrate, materials with relative density of 97% at 1100°C can be obtained. In contrast, when iron was introduced as oxide via ball milling less dense materials, 94% relative density, at higher temperature, 1200°C, obtained.

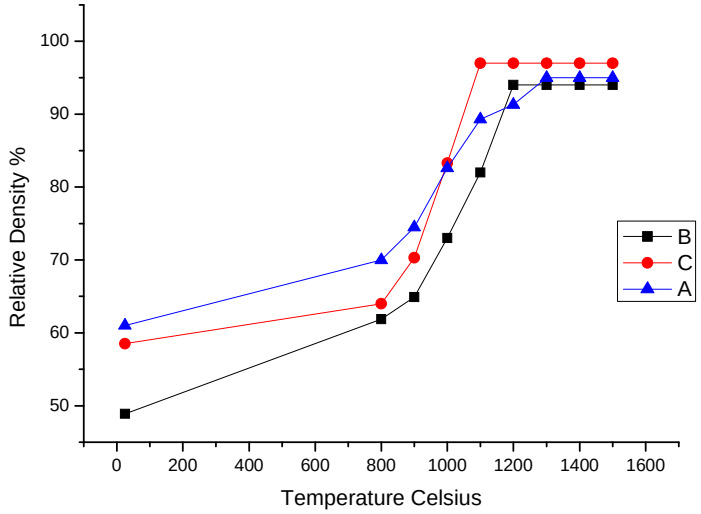

Figure 5.15 Relative density vs. sintering temperature. A: Pure CGO10, B: 0.5 Fe at % with ball milling, C: 0.5 Fe at. % *"in situ"*

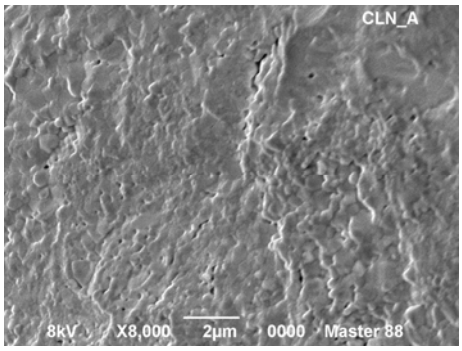

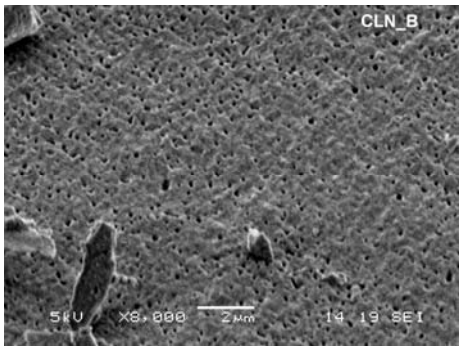

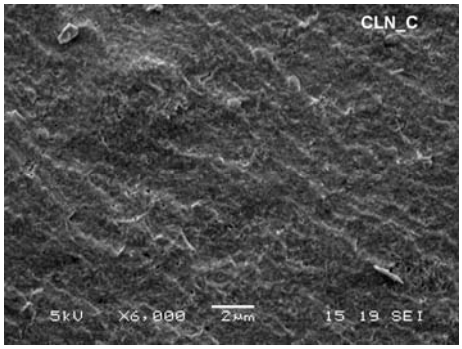

Figure 5.16 SEM pictures from the sintered pellets at 1300^0 for CLN_A, 1200^0C for CLN_B, and 1100 for CLN_C.

5.4 Powders and Pellets prepared with the Complexation High Concentration Method

5.4.1 Characterization

The XRD measurements for powders prepared with the complexation high concentration method with or without HNO_3, seem to verify the assumption that the calcination step could be avoided, due to pyrolysis during the drying step, proved by the thermal decomposition behavior of the powder measured by means of TGA (figure 4.4).

The XRD difractograms in figure 5.17 confirms the fluorite structure of the precursor powder for both synthesis routes (with or without HNO_3). The crystallite size, calculated from the broadening of the peaks, is in both cases 29 nm.

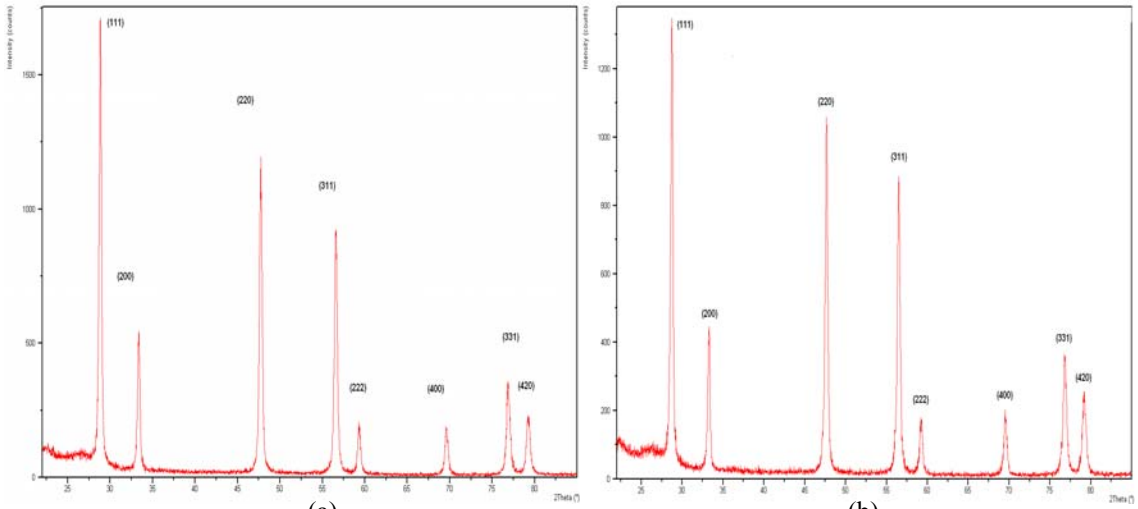

Figure 5.17 XRD diffractograms of CGO10 prepared with and without HNO_3 . (a) with HNO_3 (b) without HNO_3.

The addition of HNO_3 did not affect significantly the mean particle size of the powders (table 5.6), however powders obtained with the addition of HNO_3 exhibited broader particle size distribution before milling, and narrower after milling when iron was introduced (Figure 5.18).

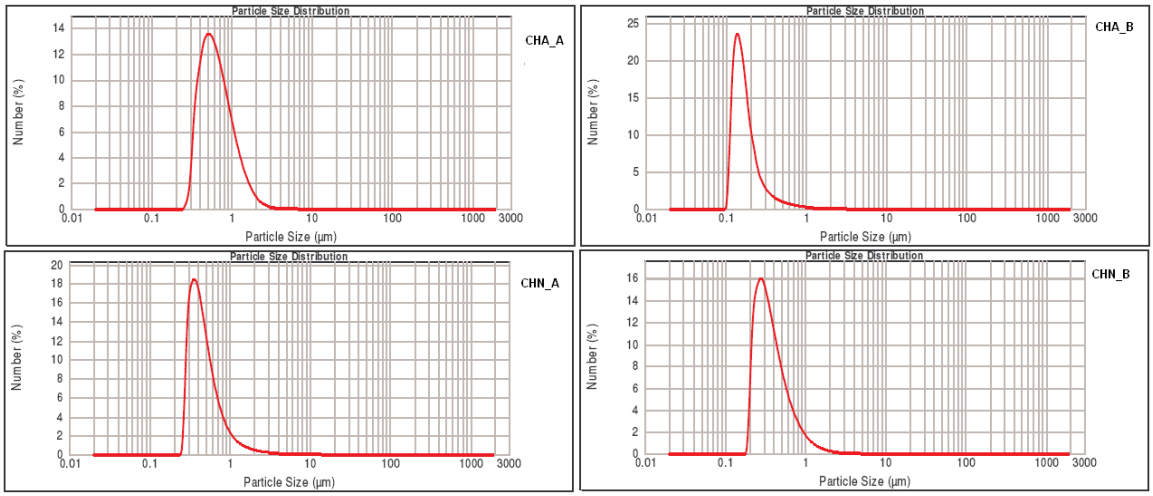

Figure 5.18 particle size distribution measured with laser diffraction CHA_A with HNO_3 pure CGO10, CHA_B with HNO_3 and addition of Fe_2O_3. CHN_A no HNO_3 pure CGO10 CHN_B no HNO_3 with Fe_2O_3

5.4.1 Densification Behavior

Pellets that were prepared with the addition of HNO_3 exhibited relative density of 97% at 1300°C, temperature lower by 200°C from what is reported in literature for pure CGO10 [4]. The addition of 0.5 at% Fe via ball milling enhanced the sintering behavior of the material. In that manner highly dense pellets with relative density 99%, calculated with the Archimedes method, at 1200°C obtained.

Table 5.4 Crystallite size D calculated using Scherrer's Formula, the mean particle size D_p, and the grain diameter D_g after sintering

Composition	*D (nm)*	*D_p (μm)*	*D_g (μm)*
With HNO_3 pure CGO10 (CHA_A)	29	0.5	0.51
With HNO_3 addition 0.5 at % Fe with ball milling (CHA_B)	29	0.15	0.41
Without HNO_3 pure CGO10 (CHN_A)	29	0.4	1.4

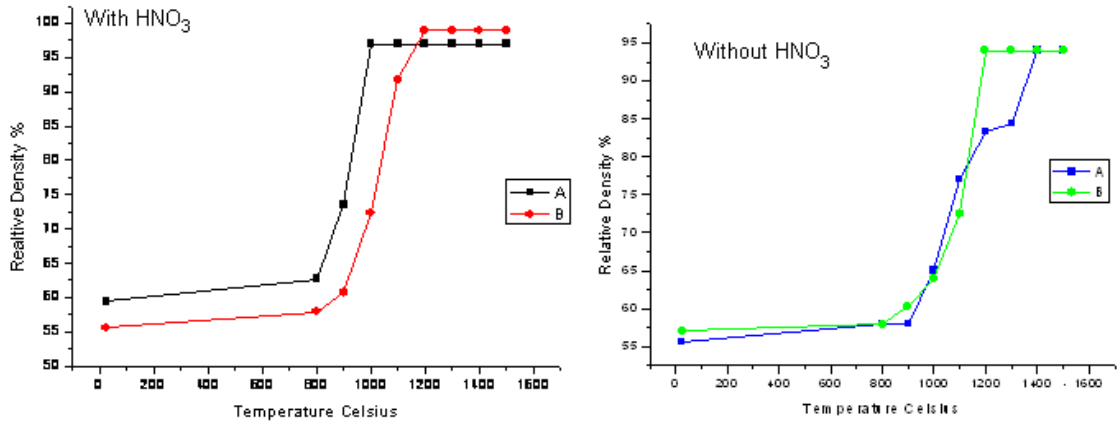

Figure 5.19 Relative density vs. Temperature. A: pure CGO10 , B: addition of 0.5 at% Fe

Comparison of the two graphs in figure 5.19 reveals the significant contribution of iron in achieving higher densities in lower temperature for both cases (with and without HNO_3) separately. The SEM pictures in figure 5.20 verify the high density of the pellets prepared with the addition of HNO_3. Additionally pellets prepared with HNO_3 had much smaller grain size after sintering at 1300°C of factor ~3 (Table 5.4). Pellets prepared without HNO_3 exhibit more porous morphology (94% relative density) sintered at 1500°C.

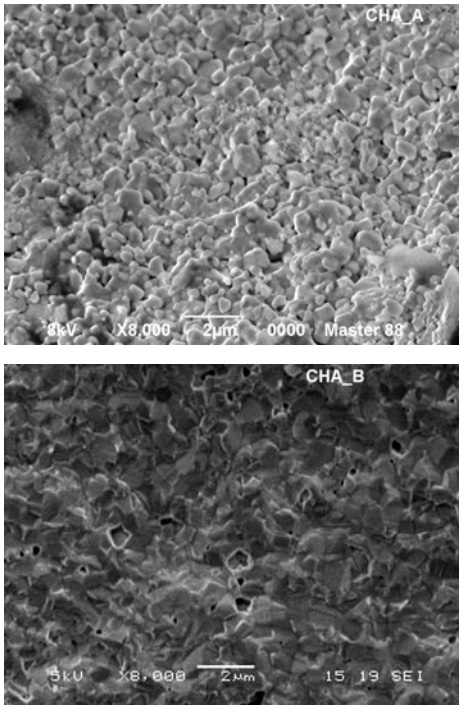

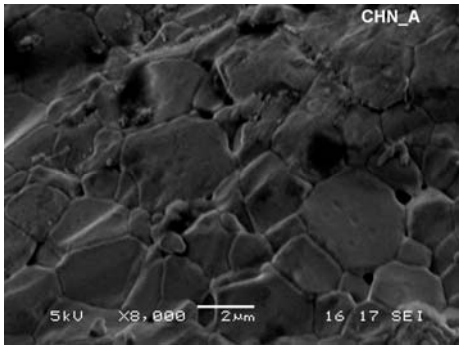

Figure 5.20 SEM pictures of CHA_A, CHA_B, and CHN_A

5.5 Discussion

Pellets which prepared via the citrate route and iron was incorporated *"in situ"* exhibited higher density with respect to the ones in which iron introduced via ball milling (98% and 97% relative density respectively) at the same temperature 1200°C, indicating that iron is better dispersed in the matrix of the material when it is added *"in situ"* enhancing the densification of the pellet. The same behavior of iron was also observed during the Complexation Low Concentration method with or without HNO_3, depicting a significant contribution of iron to the densification behavior of the material when it was added as $Fe(NO_3)_3 \cdot 9H_2O$.

A reasonable explanation for this behavior could be that when iron was introduced via ball milling it might dispersed inhomogenously forming iron oxide clusters in the material matrix. In that manner, less dense or less homogenously dense material was obtained, as it is depicted in the SEM pictures in figure 5.10.

A solid conclusion about the way in which iron was dispersed in the material before and after sintering can be made with Transition Electron Microscopy (TEM) pictures.

The addition of HNO_3 influenced the density of the pellets and the sintering temperature. Regardless the concentration of $Ce(NO_3)_3 \cdot 6H_2O$ and $Gd(NO_3)_3 \cdot H_2O$ pellets in which HNO_3 was added had higher density than those without HNO_3. Especially in the case where low concentration of ceria and gadolinia nitrates was added, pellets with relative density 100% obtained. However, in the case where low concentration of nitrates and no HNO_3 was added, pellets sintered at 1100°C, with relative density 97%, while for pellets in which HNO_3 was added the lowest sintering temperature was 1200°C.

M.M Nasrallah et. al. [5] fabricated thin films of $(CeO_2)_{0.8}$ (SmO1.5) 0.2 via sol-gel, reported that HNO_3 oxidizes the ethylene glycol converting it to oxalic acid (figure 5.21) and the formed polyester allows homogenous chelation of metal ions. In that manner, there is a small amount of cross-linking in the polymeric precursor films. Accordingly dense and homogenous films with uniform shrinkage obtained. Similarly, the same process is taking place-obtaining powders with narrow particle distribution, enhancing their densification behavior upon sintering with the addition of iron *"in-situ",* figure 5.8c.

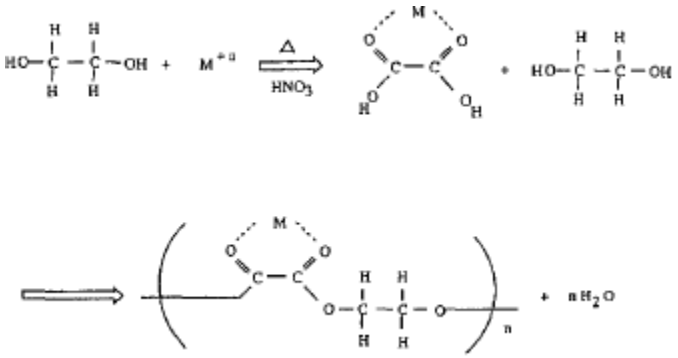

Figure 5.21 Reaction Mechanism for ethylene glycol with HNO_3 [5].

Comparison of grain sizes after sintering of powders which were calcined at 850°C (citrate route) and at 700°C (complexation low concentration method with and without HNO_3) reveals a calcination temperature dependence on the grain size of the pellet. A better comparison could be made for powders prepared with the same method and calcined at different temperatures.

5.6 Conclusions

Pellets, which prepared with the new modified *"in situ"* incorporation of iron revealed in all cases relative densities higher than 97% at low temperatures, as 1100°C, with grain size much smaller than 0.38 μm. In the case of the citrate route, pellets prepared with the *"in situ"* method sintered at 1200°C, the same temperature as when iron was introduced via ball milling, however the obtained grain size was two times smaller, 0.46 μm, while in the case of ball milling the obtained size was 0.9 μm.

When the low complexation method was used, regardless the additions of iron, high relative densities, as 100%, were obtained. Dramatically the sintering temperature of unloaded with iron CGO10 dropped to 1300°C, temperature which is lower more than 200°C from what is reported in literature. Pellets prepared with the low complexation method exhibited grain size of~0.4 μm, while in literature [6] the reported value for pure CGO10 sintered at 1350°C is 1 μm. The *"in situ"* incorporation of iron reveals crack free pellets with high density up to 100%, and at low temperature as 1100°C.

The addition of HNO_3 seems to contribute in obtaining high density materials, however in the case were iron is not introduced *"in situ"* pellets with cracks were obtained. No calcination step prior sintering seems feasible, in the case of the high concentration complexation method, however a better control of the drying process should be further investigated.

5.7 Recommendations

The foregoing research revealed promising results for the *"in situ"* introduction of iron, however a better understanding of the way in which iron is incorporated in the material is required. The XRD patterns are not sufficient for the detection of any second phase of iron oxide due to the very small amount of iron. SEM micrographs only provide information regarding the topology and the surface composition of the material. However, transmission electron microscopy (TEM) could provide a more clear view since the electron beam in TEM projects all information on the mass it encounters in a two-dimensional image.

Additionally electron dispersive x-ray analysis (EDAX) could provide elemental analysis of the samples. Plotting of the lattice constant versus the amount of iron oxide, where any decrease in lattice constant would suggest an increasing amount of dissolved Fe_2O_3 [1]. The fabrication of thin films using the low complexation method with the addition of HNO_3 acid seems promising due to the high density of the material at low temperature and consequently small grain size, since pressing is problematic leading to cracks. Finally a further investigation of the correlation between calcination and sintering temperature with grain size is required, the plots 6.15 and 6.16 in Chapter 6 depict a trend between sintering temperature and grain size.

References

[1] M.J. Verkek, A.J.A Winnubst, A.J. Burggraaf, *Journal of Materials Science,* **17** (1982) 3113-3122

[2] T.S Zhang, J. Ma, L.H. Luo, S.H. Cha, *Journal of Alloys and Compounds,* **422** (2006) 46-52

[3] T.S Zhang, P. Hing, H. T Huang, J.A. Kilner, *Journal of Materials Science,* **37** (2002) 997

[4] K. Huang, M. Feng, J .B. Goodenough, *J. Am. Soc.* **81** (1998) 357-362

[5] C.C Chen, M.M. Nasrallah, H.U. Anderson, *J. Electrochm. Soc.,* **140,** (1993) 3555-3559

[6] C.R. Xia, M.L. Liu, *Solid State Ionics,* **152** (2002) 423-430

[7] William D. Callister, *Material Science and Engineering an Introduction*, 7th Edition, Wiley 2007

Chapter 6-Electrochemical Characterization

6.1 Introduction

The electrochemical performance of the samples was measured by means of Electrochemical Impedance Spectroscopy (EIS). Pellets of 5.85 mm diameter and 2.27 mm thickness were cut from the sintered pellets. Pellets were mechanically polished with SiC and diamond paste. Gold electrodes were applied on both sides of the pellets by sputtering and painting. Prior to sputtering, pellets were cleaned with ethanol in ultrasonic bath, since surface impurities can cause loss of adhesion when samples are heated during measurements [1]. The sputtered gold electrodes had thickness of 300 nm, after sputtering gold paste was painted. The paste was dried for 10 min at 150°C and fired for 20 min at 600°C.

The electrochemical impedance was measured in two-electrode geometry (figure 6.1). Gold was chosen as electrode, because gold is rather inert with respect to the dissociative absorption of oxygen, since the performance of oxygen-ion conducting devices depends not only on the (partial-) ionic conductivity of the bulk oxide but also on the rate of exchange of oxygen at the ambient/solid-oxide interface [2]. The choice of electrode also depends on the temperature of investigation.

The frequency dispersion (100 kHz-10 Hz) was measured with a Solartron 1255 Frequency Response Analyzer (FRA) in combination with a differential amplifier in order to increase the input impedance of the FRA. The pellet with the deposited Au was placed between solid gold electrodes.

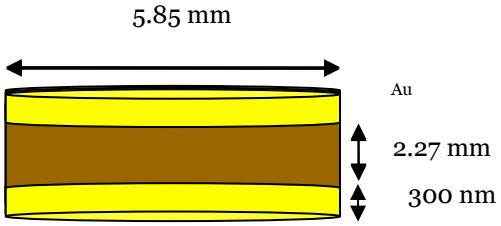

Figure 6.6 Two-electrode geometry using Au as counter electrode

Validation of the impedance data performed using a Kramers-Kronig transformation test program [3], and analyzed using the software package "Equivalent Circuit" [4]. For all the measurements, the obtained chi K-K-squared ($\chi^2_{K\text{-}K}$) value was much smaller than 10^{-6} (most of the times in the order of 10^{-7} and 10^{-8}) validating the accuracy of the data.

Initially the electrodes were heated at 800°C and the impedance was measured under nitrogen conditions (O_2< 10ppm), and then it was compared with the measurement under ambient conditions. Comparison of the impedance plots showed that the ionic resistance remained virtually constant, when the electrode resistance was significant larger in nitrogen than air. This indicates that electronic conduction is so small that can not be detected.

Impedance measurements as function of temperature were performed under ambient conditions by decreasing the temperature from 800°C to 211°C with steps of 50°C.

The impedance spectrum of an ionic conductor contains the contribution from the grains, the grain boundary, and the electrode-electrolyte interface which can be simplified by three arcs as shown in figure 6.2 [5]. The appearance of these three semicircular arcs in a complex impedance spectrum means that the equivalent circuit foe the specimen can be represented as three parallel *R-C* elements in series as shown in figure 6.2 (b) [6].

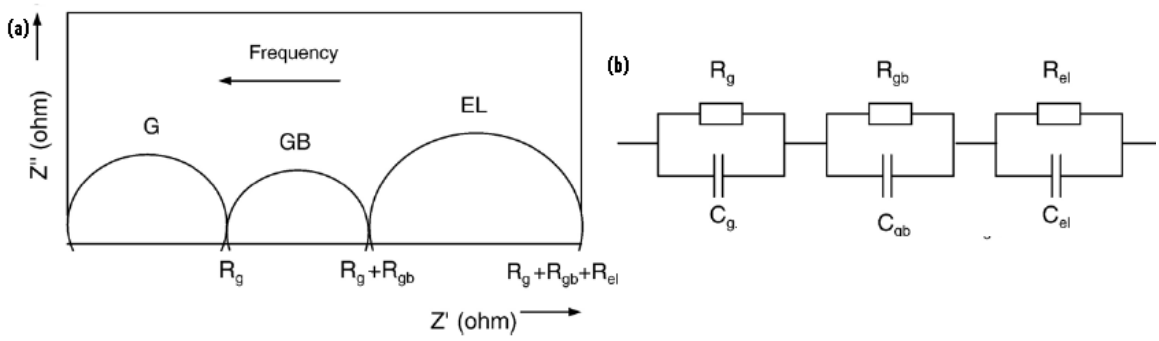

Figure 6.2 An idealized impedance spectra (a) and the equivalent circuit (b) R_g and C_g are the resistance and capacitance for the grain, R_{gb} and C_{gb} represent the impedance and capacitance for the grain boundary, and R_{el} and C_{el} represent the impedance and capacitance for the electrode [5].

However not all these arcs can be observed, depending on the nature of the sample and the conditions of the experiment [5]. The three arcs can be identified clearly at below 300°C, temperature much lower than the operation temperature of the material. The normalized impedance spectra at 300°C and 600°C under standard conditions for all synthesis routes are given in Appendix B. It should be mentioned, that in the present chapter an overview of the impedance measurements is presented, the reproducibility of the results will be conducted in a further step.

6.2 Electrochemical Performance of pellets prepared with the Citrate Route

The normalized impedance spectra at 600°C in figure 6.3 of CR_A, CR_B, and CR_C indicate no grain boundary resistance for CR_B and CR_C and a relative small grain boundary arc for CR_A, with grain boundary resistivity 237 Ω×cm. This behavior can be explained firstly by the scavenging property of iron and secondly by the small grain size of CR_B and CR_C (0.9 and 0.46 μm respectively) with respect to CR_A (2.2 μm)

The total activation energy (figure 6.4) of CR_A is 86.7 kJ/mol value slightly higher than the reported values in literature [7], indicating that the grain boundary contribution dominates, even though the lattice activation energy is 52

kJ/mol value much lower than the reported value in literature [7] (69.5 kJ/mol). For CR_B the total activation energy (figure 6.5) is equal with the grain activation energy, due to the absence of grain boundary contribution (figure 6.3). the obtained value of activation energy is 74.3 kJ/mol, value which is in good accordance (taking in account the error estimation) with literature (74.3 kJ/mol). However, when pellets prepared via the *"in situ"* method a decrease observed in the total activation energy, and the obtained value is 72.7 kJ/mol.

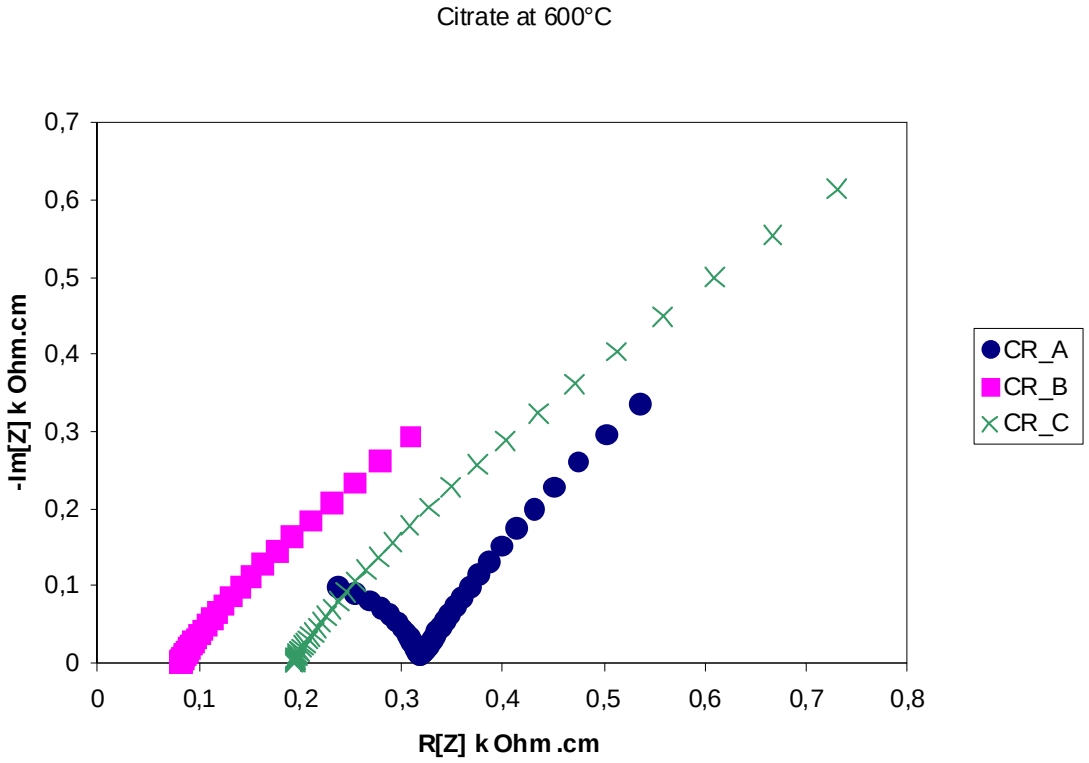

Figure 6.3 Normalized impedance spectra for CR_A, CR_B, and CR_C at 600^0C, for CR_B and CR_C only the electrode response is observed

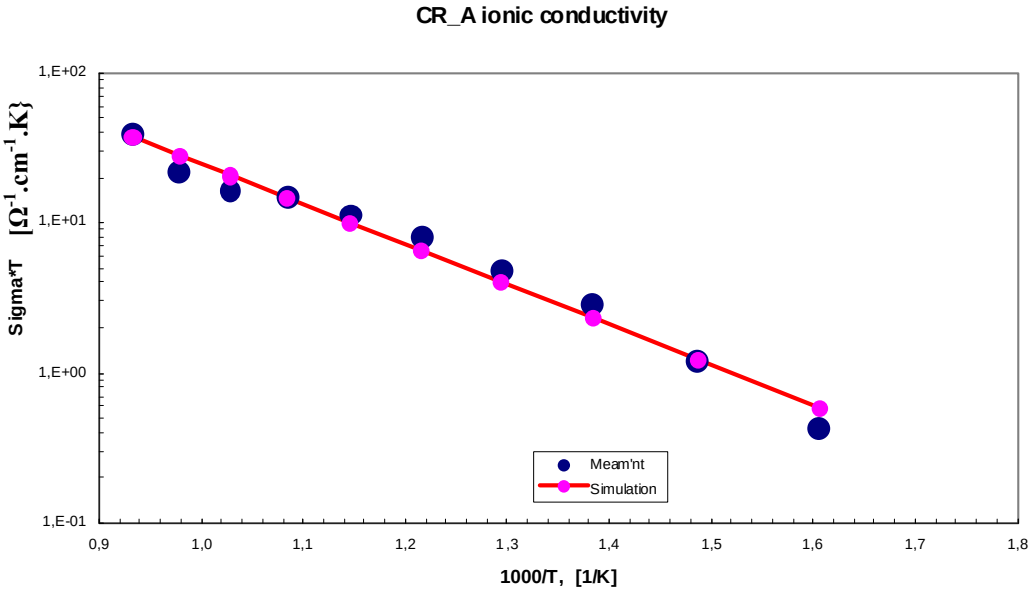

Figure 6.4 Temperature dependence of the ionic conductivity of CR_A

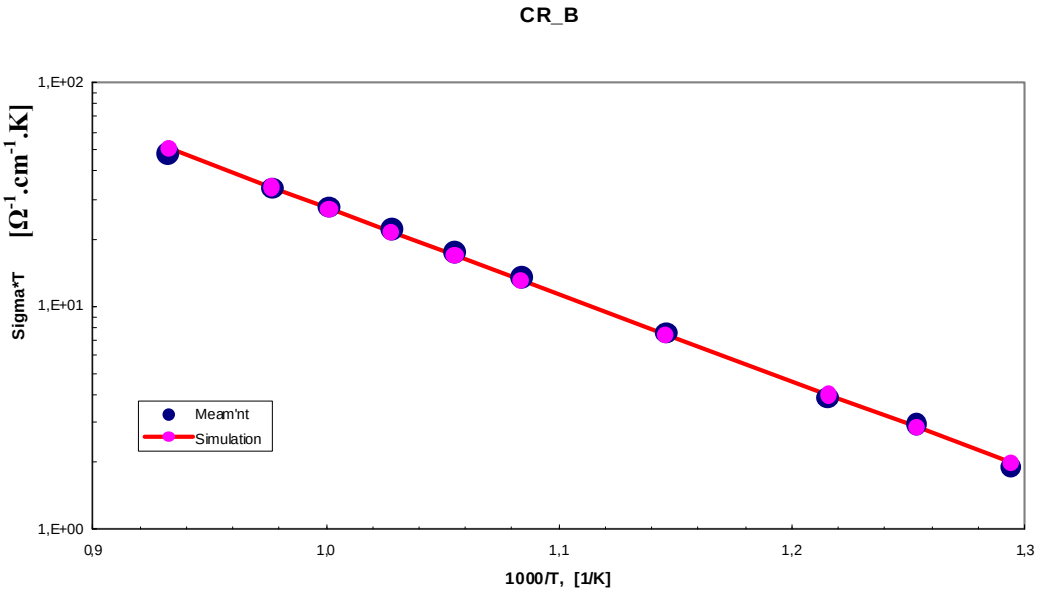

Figure 6.5 Temperature dependence of ionic conductivity of CR_B

CR_A exhibited total conductivity at 600°C of 6×10^{-3} S/cm value which is lower when it is compared with the values in [11] and [7] where the obtained conductivities are 1.67×10^{-2} S/cm and 1.47×10^{-2} S/cm respectively, but higher

with respect to the value in [12] which is 3.63×10^{-3} S/cm. A possible explanation for this behavior of CR_A, is the slightly increased total activation energy with respect the values in literature [7] and [11] and lower than [12]. When 0.5 at. % of Fe incorporated via ball milling (CR_B) the ionic conductivity was significantly improved with respect to CR_A, the obtained value is 8.76×10^{-3} S/cm. Despite the agreement in activation energy of CR_B with the value in [7], CR_B still exhibited lower total conductivity than the values in [7] and [11]. The results seem reasonable when one compares the grain size of the pellets in [11] sintered at 1250°C being 0.5 μm, where the obtained grain size of CR_B is 0.9 μm sintered at 1200°C.

Table 6.1 Activation Energies [a] and total conductivities [b]

Composition	*Relative density*	*Sintering Temp[c]*	*E_t (kJ/mol)*	*Literature (kJ/mol)*	*E_t*	*σ_t (S/cm)*	*Literature σ_t (S/cm)*
CR_A	95%	1500°C	86.8	82[7] 57.8[11]		6×10^{-3}	0.0147[7] 1.67×10^{-3}[11]
CR_B	97%	1200°C	74.3	74.3[7]		8.76×10^{-3}	0.0202[7]
CR_C	98%	1200°C	72.7	74.3[7]		7.82×10^{-3}	0.0202[7]

[a] The total activation energies E_t were measured in the temperature range of 600-800^{0}C
[b] The total conductivities σ_t were measured at 600^0 and compared with literature values [7] and [11]for the same temperature regime
[c] All samples were sintered for 6h

6.3 Electrochemical Performance of pellets prepared with the Complexation Low Concentration Route

Due to the cracking of the pellets that were prepared with the low concentration complexation method with HNO_3 only pellet CLA_C was tested since it revealed no cracks with the *"in situ"* incorporation of iron. CLA_C pointed out similar electrochemical behavior with the pellets in which HNO_3, indicating no significant contribution of HNO_3 to the electrochemical behavior of the material. The total activation energy is 72.8 kJ/mol value smaller than the reported in literature [7], figure 6.6 depicts the total conductivity vs. the temperature for CLA_C.

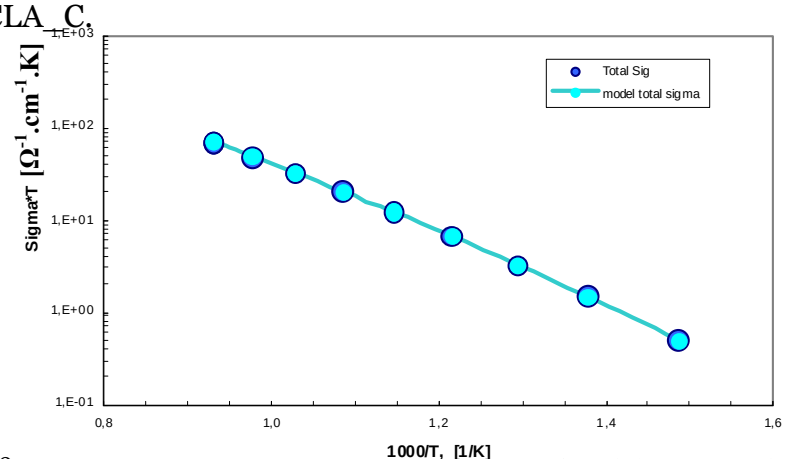

Figure 6.6 Arrhenius plot of CLA_C from 400-800^{0}C

The Arrhenius plot of the total ionic conductivity is given in figure 6.7. The total activation energy for CLN_A and CLN_C is almost identical. The activation energy of CLN_A is 72.1 kJ/mol and the activation energy for CLN_C is 73.7 kJ/mol. These values are smaller than what is reported in literature [7], around 82 kJ/mol for pure CGO10 and 74 kJ/mol for 0.5 at. % Fe-CGO10. CLN_B revealed 122 kJ/mol activation energy. This value is much higher from what is reported in literature and with respect to CLN_C and CLN_A.

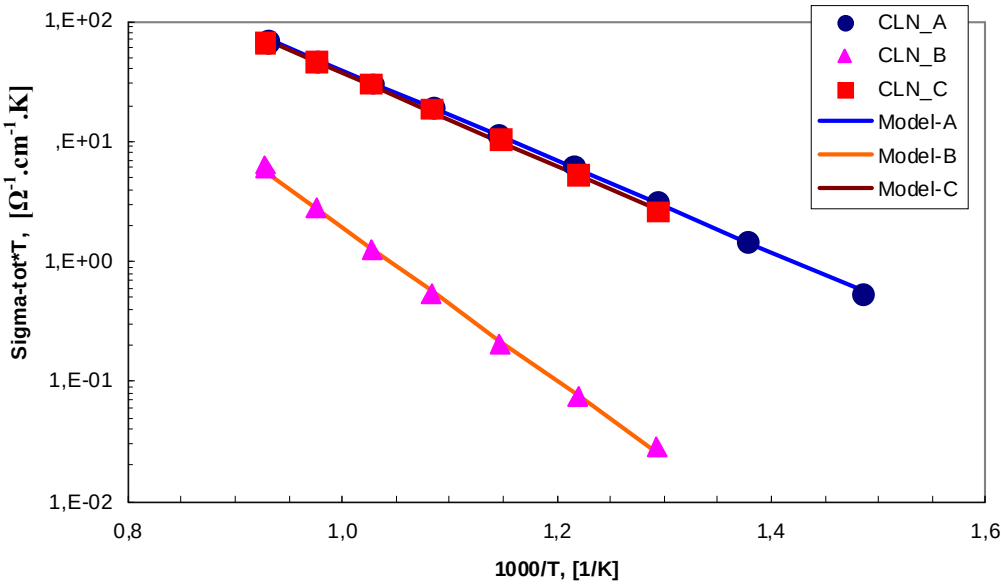

Figure 6.7 Arrhenius plot of the total conductivity of CLN_A, CLN_B, and CLN_C

Despite the significantly lower activation energy of CLN_A and CLN_C with respect to the values reported in literature, the total conductivity is not higher. For CLN_A the total conductivity at 600°C is 0.013 S/cm and the reported value in literature [7] is 0.0147 S/cm. The difference is even higher for the case of CLN_C where the obtained value at 600°C is 0.012 S/cm and the referred value in literature [7] is 0.0202 S/cm. In the case of CLN_B the total conductivity is very low as expected due to the very high activation energy, the obtained total conductivity at 600°C is 2.3×10^{-4} S/cm.

The normalized impedance spectrum in figure 6.8 reveals that at 600°C there is a significant grain boundary resistance for CLN_B while for CLN_A and CLN_C is negligible. One could expect that CLN_B and CLN_C should have similar behavior, since in both case 0.5 at. % Fe was added. On the contrary CLN_C reveals identical behavior with CLN_A. A reasonable assumption for the behavior of CLN_A could be the small percentage of impurities, something that should also apply for CLN_B, since is the same starting powder.

According to H.L. Tuller [8] absence of grain boundary arc indicates small grain size. This assumption comes in accordance with the SEM micrographs in chapter 5 (figure 5.16). The calculated grain size for CLN_A, using the intersect method [13] is 0.38 *μm,* while the reported value in literature [7] for pure CGO10

is 2.2 *μm*. Careful observation of the SEM micrographs in figure 5.16 shows a rather more porous morphology for CLN_B when it is compared with CLN_A and CLN_C, indicating that when iron is added *"in situ"* (CLN_C) more homogenous incorporation of the iron can be obtained. This indication will be determined in a further step by transmission electron microscopy (TEM).

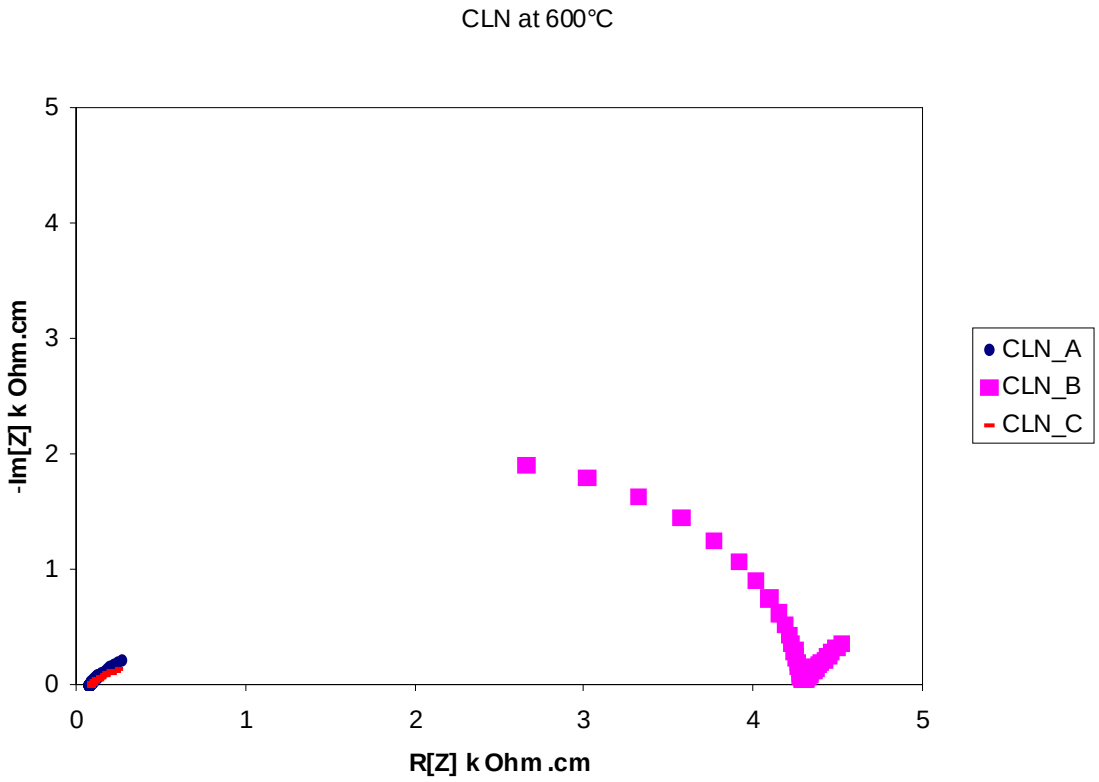

Figure 6.8 Normalized impedance spectra for CLN_A, CLN_B, and CLN_C at 600^0C.

Table 6.3 Activation Energies [a] and total conductivities [b]

Composition	*Relative density*	*Sintering Temp.*[c]	E_t *(kJ/mol)*	*error (kJ/mol)*	*Values in [7] E_t (kJ/mol)*	σ_t *(S/cm)*	*Values in [7] σ_t (S/cm)*
CLN_A	95%	1300°C	72.1	±0.7	82	0.013	0.0147
CLN_B	94%	1200°C	122	±1.2	74.3	2.3×10^{-4}	0.0202
CLN_C	97%	1100°C	73.7	± 2.2	74.3	0.012	0.0202
CLA_C	100%	1200	72.8		74.3	0.014	0.0202

[a] The total activation energies E_t were measured in the temperature range of 600-800^0C

[b] The total conductivities σ_t were measured at 600^0 and compared with literature values [7] for the same temperature regime

[c] All samples were sintered for 6h

6.4 Electrochemical Performance of pellets prepared with the Complexation High Concentration Route

6.4.1 With HNO3

Figure 6.9 depicts the Arrhenius plot of grain, grain boundary, and total activation energy for both CHA_A and CHA_B. For CHA_A the total activation energy is 72.6 kJ/mol, value lower than the values in literature [7] (82 kJ/mol). The total activation energy of CHA_B is 82.6 kJ/mol, quite high with respect to literature [7]. The plot in figure 6.4x reveals that for low temperatures there is a considerable deviation in the total activation energy for CHA_ and CHA_B, while in high temperatures the total activation energies for both samples matches. This behavior is because of the negligible grain boundary contribution in temperatures above 500°C [9], and as it is depicted in the normalized impedance spectra in figure 6.10, the grain boundary arc of CHA_B is much higher compared to the grain boundary arc of CHA_A verifying this assumption.

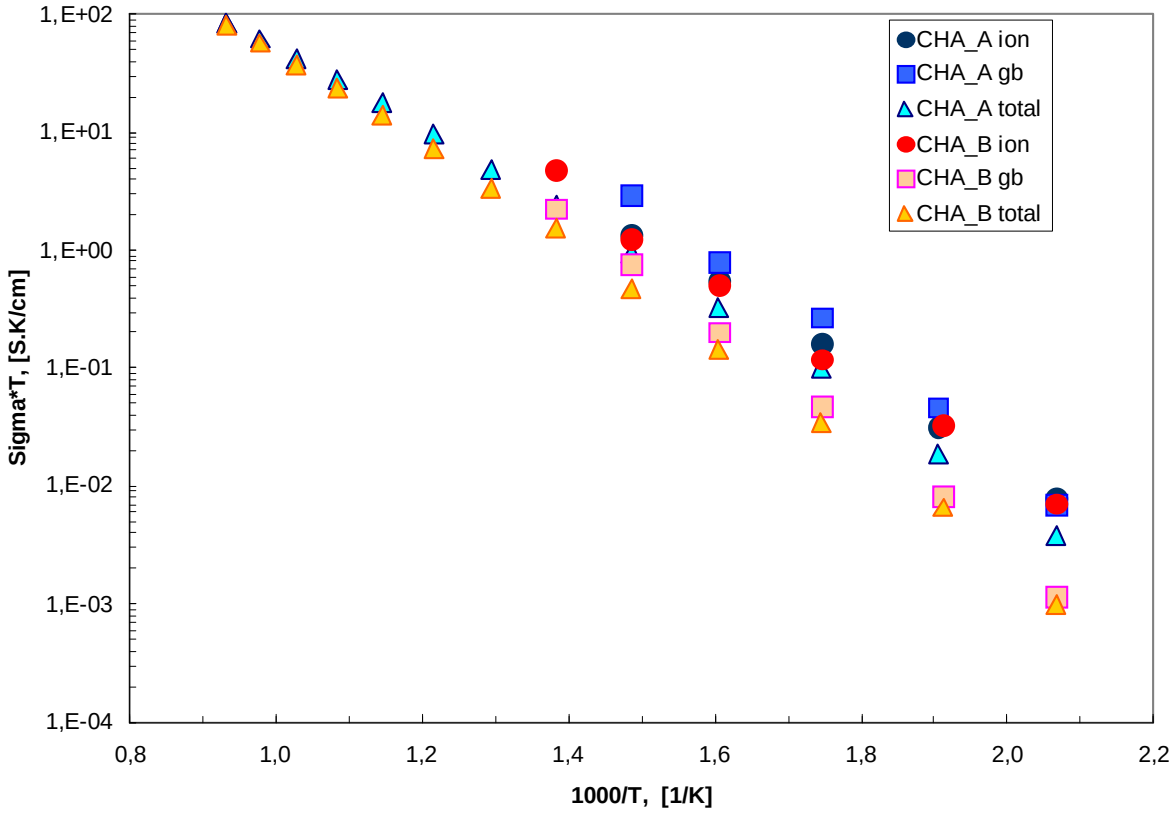

Figure 6.9 Arrhenius plot of conductivities CHA_A and CHA_B

The grain size of CHA_A calculated with the intersect method is 0.51 μm exhibiting total conductivity of 0.02 S/cm, value higher than what is reported in [7] where the total conductivity is 0.0147 S/cm and the grain size is 2.2 μm. The grain boundary conductivity of CHA_A is higher by a factor of 10 compared to literature [7], indicating the influence of the grain size on the grain boundary resistance. Absence of grain boundary arc indicates small grain size [8], as it is depicted in the normalized impedance spectra in figure 6.10, the grain boundary arc of CHA_A is smaller than the arc in [7] figure 6.10 (b).

In the case of CHA_B, the grain size is almost six times smaller than the size of the sample reported in [7]. Despite the smaller size of the grains in CHA_B, the arc of the grain boundary resistance in the normalized impedance spectra in figure 6.10(a) is much larger than the arc in figure 6.10(b) [7]. A reasonable explanation for this result could be the fact that since the powder that was used for the fabrication of CHA_B was not the same as with CHA_A, impurities might be introduced in one of the pellet preparation steps. This assumption can be verified from the very small grain boundary conductivity of the pellet as it is shown in table 6.4.

Table 6.4 Activation Energies [a] and conductivities [b]

Composition	E_g *(kJ/mol)*	E_{gb} *(kJ/mol)*	E_t *(kJ/mol)*	σ_g *(S/cm) 350°C*	σ_{gb} *(S/cm) 350°C*	σ_t *(S/cm) 600°C*
CHA_A [c]	77.8 (69.46)[7]	94.2 (91.66)[7]	72.6 (82)[7]	8.79×10^{-4} (9.96×10^{-4})[7]	1.28×10^{-3} (3.23×10^{-4})[7]	0.02 (0.0147)[7]
CHA_B [c]	74 (69.46)[7]	92.3 (87.8)[7]	82.6 (74.3)[7]	2.08×10^{-4} (9.98×10^{-4})[7]	8.28×10^{-5} (1.27×10^{-4})[7]	0.016 (0.0202)[7]

[a] The activation energies for grains E_g, grain boundaries $E_{gb,}$ and total E_t, were measured in the temperature range of 211-400^{0}C. The compared values in literature [7] are in the temperature range of 211-400^{0}C for E_g, and $E_{gb,}$ and 250-700^{0}C for E_t

[b] The total conductivities σ_t were measured at 600^0 and compared with literature values [7] for the same temperature regime. The grain conductivities σ_g and the grain boundary conductivities σ_g were measured at 350^{0}C and compared with the values in [7] for the same temperature regime

[c] All samples were sintered for 6h, CHA_A at 1300^{0}C and CHA_B at 1200^{0}C, prior sintering **no** calcination step took place. Grain size of CHA_A is 0.51 μm and for CHA_B 0.81μm

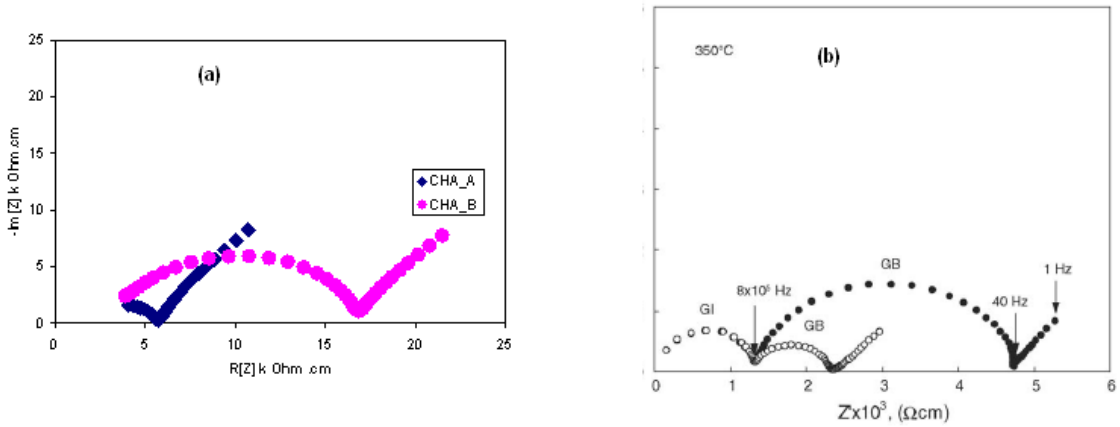

Figure 6.10 (a) Normalized impedance spectra for CHA_A and CHA_B at 300^{0}C (b) Normalized impedance spectra for pure CGO10 (•) and 0.5 at. % Fe-CGO10 (o) at 350^{0}C from literature [7]

6.4.2 Without HNO3

Figure 6.11 depicts the normalized impedance spectra for the samples prepared via the high concentration complexation route without the addition of HNO_3 and no calcination step prior sintering. CHN_A reveals a significant grain boundary resistance where on contrary, when HNO_3 was added (CHA_A) Appendix B no grain boundary resistance obtained. On the contrary, CHN_B and CHA_B seem to behave similarly as it is depicted in figures 6.10 and Appendix B, indicating no significant effect of HNO_3 on the electrochemical behavior of the loaded with Fe samples.

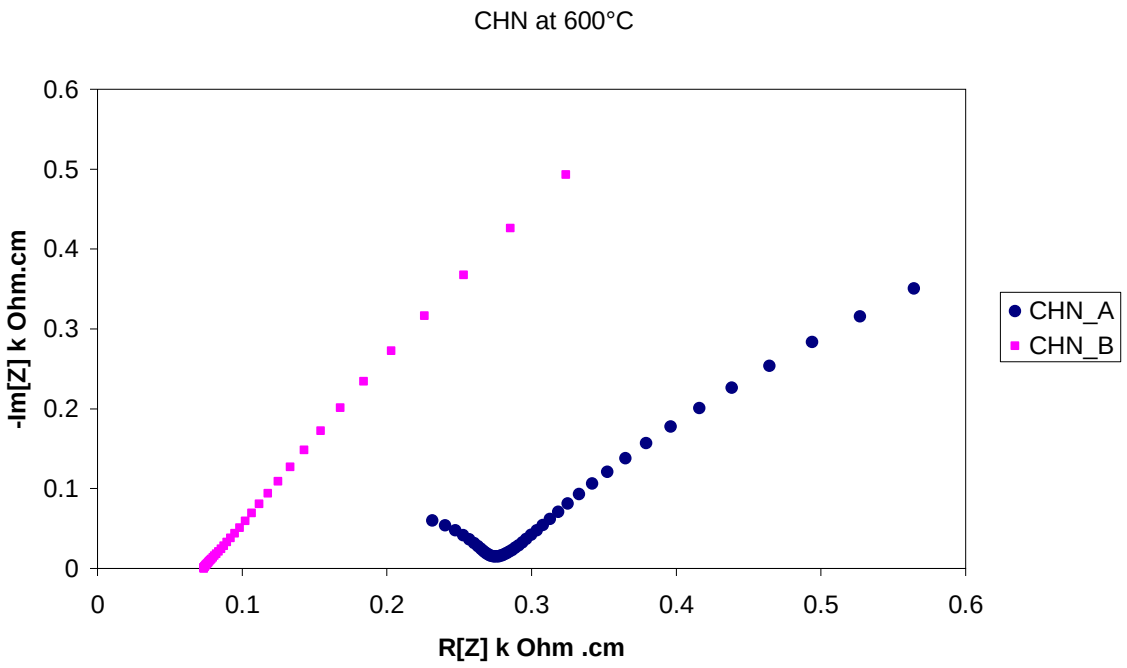

Figure 6.11 Normalized impedance spectra of CHN_A and CHN_B at 600^0C

The Arrhenius plot in figure 6.12 reveals that for temperatures above 600°C CHN_A and CHN_B behave identically, despite the lower activation energy of CHN_B (86 kJ/mol), they have comparable values of total conductivity, table 6.5. CHN_A revealed high total and grain boundary activation energy compared to CHA_A, due to the three times larger grain size. Also the total conductivity is much lower at 600°C with respect to CHA_A, apparently due to the very high activation energy.

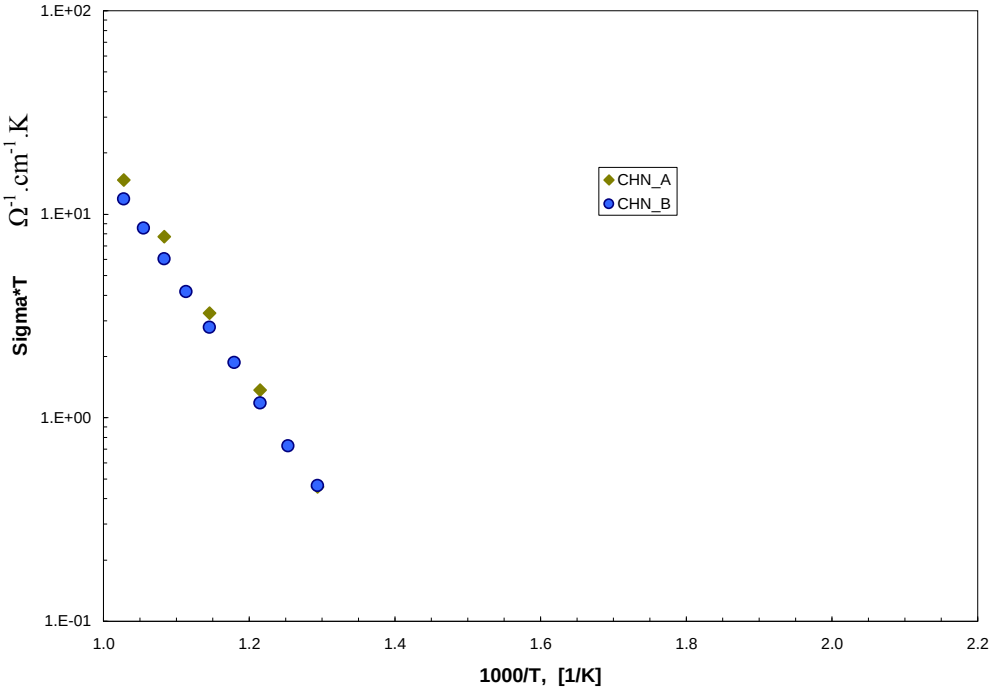

Figure 6.12. Arrhenius plot of the total activation energy of CHN_A and CHN_B at 600^0C

Table 6.5 Activation Energies [a] and conductivities [b]

Composition	*Sintering Temp.*	*Densit*	E_g *(kJ/mol)*	E_{gb} *(kJ/mol)*	E_t *(kJ/mol)*	σ_t *(S/cm) 600°C*
CHN_A [c]	1500°C (1300°C)[d]	94% (97%)[d]	56 (77.77)[d]	165 (94.21)[d]	105.1 (72.6)[d]	3.74×10^{-3} (0.02)[d]
CHN_B [c]	1200°C (1200°C)[d]	94% (99%)[d]	72.6 (73.97)[d]	97.29 (92.28)[d]	86 (82.63)[7d]	3.18×10^{-3} (0.016)[d]

[a] The activation energies for grains E_g, grain boundaries $E_{gb,}$ and total E_t, were measured in the temperature range of 500-800^0C . The compared values with CHA_A and CHA_B are in the temperature range of 211-400^0C.

[b] The total conductivities σ_t were measured at 600^0 and compared with CHA_A and CHA_B for the same temperature regime.

[c] All samples were sintered for 6h, prior sintering **no** calcination step took place

[d] Values of CHA_A and CHA_B

Despite the comparable total activation energy of CHN_B with CHA_B, the total conductivity of CHN_B is much lower. A clearer conclusion could be made by the comparison of the grain size of each sample.

6.5 Discussion

For pellets prepared with the citrate route there is an apparent trend of correlation between grain size and total activation energy (figure 6.15). The *"in situ"* incorporation of iron seems to inhibit the further growth of grain size and suppressing the grain boundary resistance at the operation temperature of IT-SOFC.

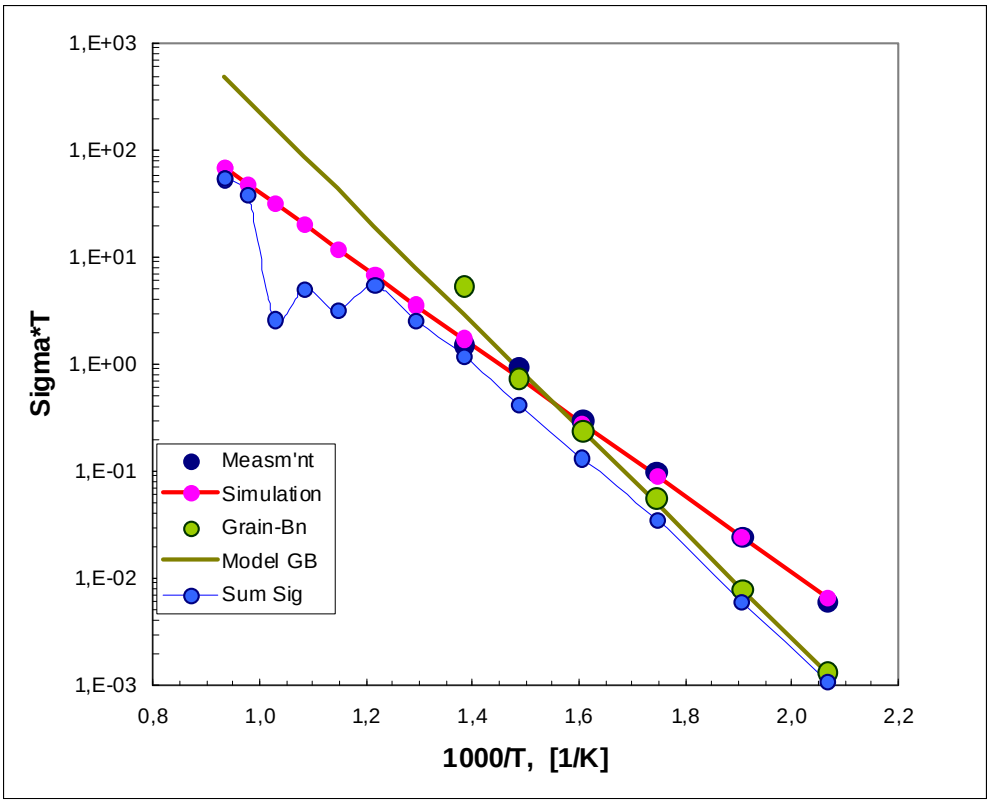

Figure 6.13 Ionic behavior of CR_C

The graph in figure 6.13 depicts the ionic behavior of CR_C. It is clear that the measurement data of ionic and total conductivity (at temperatures above 600°C) coincide with the simulation model. However, at lower temperatures there is a significant deviation between the total and grain boundary conductivity from the model, while grain boundary conductivity coincides with the total conductivity indicating that at low temperatures grain boundary resistance is dominant. Despite the fact that grain boundary resistance is dominant at low temperatures, the grain size of CR_C (0.46 μm) is much lower than CR_A (2.2 μm) and CR_B (0.9 μm) therefore conductivity is higher and activation energy is lower.

When complexation low concentration method was used for the preparation of the samples, CLN_A and CLN_C behaved similarly making clear that for pellets that sintered at temperatures below 1300°C due to the small grain size, exhibit the same ionic behavior. This assumption can be verified with the comparison of all pellets that sintered in this temperature regime (Appendix A). Observation of the Arrhenius graph in figure 6.14 shows a good match of the ionic behavior of CLN_C (CLN_C-2 is almost half of the size thinner than CLN_C-1) with pellets that prepared without *"in situ"* introduction of iron or without iron.

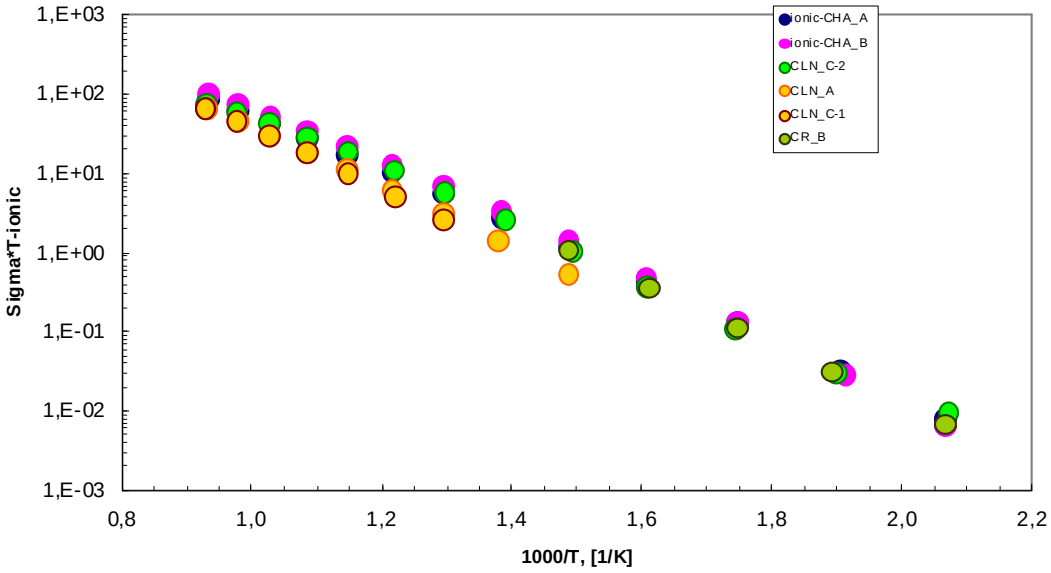

Figure 6.14 Ionic conductivities vs. temperature for different pellets

The assumption that one can make from this behavior, is that iron is not incorporated in the grains of the material, since if this was the case a significant increase to the electronic conductivity would be expected. Additionally the low grain boundary resistance and the low activation energy verify the scavenging property of iron. Grain size and sintering temperature also play an important role for the case of the high concentration complexation method as it is depicted in figure 6.15 where it is clear that for high sintering temperatures large grain size is observed. It is also clear that for the same temperature regimes (i.e. 1200°C) different grain size can be obtained, indicating the significant role of the synthesis route that is followed and the clear contribution of iron when is added *"in situ"*.

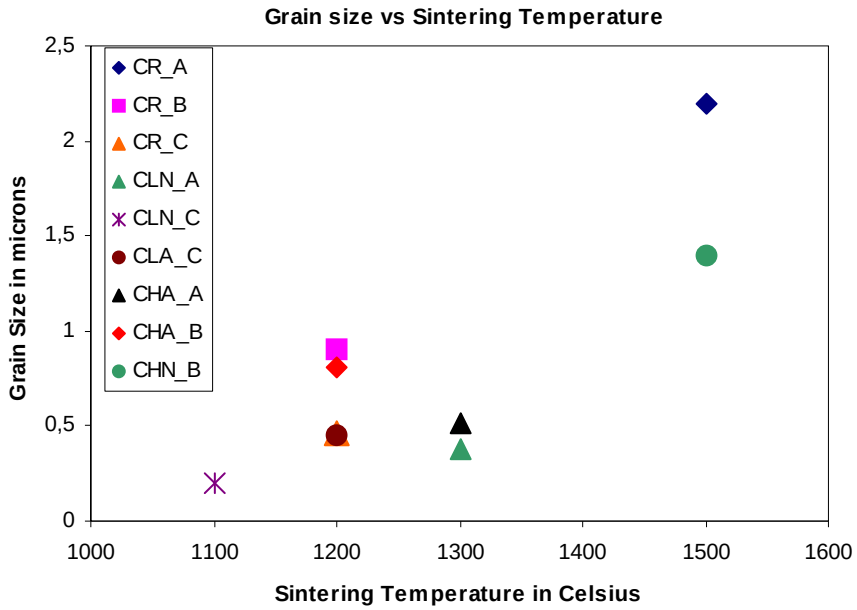

Figure 6.15 Relation of sintering temperature with grain

Figure 6.16 comes in accordance with figure 6.15, where large grains obtained at high sintering temperatures reveal high resistance at 600°C, and comparison with the graphs in Appendix B points out that grain boundary resistance is dominant. On the contrary at low sintering temperatures and especially when iron is introduced with the *"in situ"* (1100 °C) small grain size is obtained and very small resistance, and at the operation temperature of the IT-SOFC (600°C) the grain boundary contribution is negligible (Appendix B).

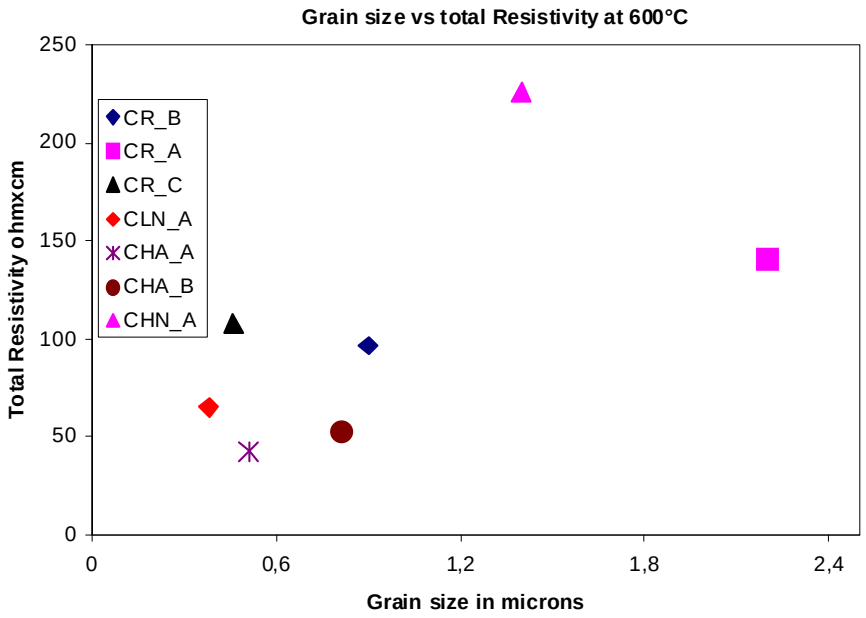

Figure 6.16 Relation of sintering temperature with grain size and resistivity

6.6 Conclusions

The electrochemical characterization of the pellets revealed the feasibility of the *"in situ"* introduction of iron into the precursor material without any increase of the electronic conductivity. The preceding research also verified the correlation between electrochemical performance of the material with the sintering temperature and furthermore with the grain size. Electrochemical data for the pellets in which no calcination step introduced prior sintering, state good performance of the material compared with literature, especially when HNO_3 was introduced. However, with the present data solid conclusion of the role of HNO_3 can not be made yet.

6.7 Recommendations

As already stated in the beginning of this chapter, the present electrochemical data are an overview, due to time limitations, of the foregoing research, therefore the reproducibility of these data has to be verified. Despite the satisfactory results of the new modified method of incorporation of iron in the material, from the impedance measurements, tranmission electron microscopy (TEM) micrographs will verify the assumption that iron is not incorporated in the lattice of the grain. Therefore CLN_C should be compared with CLN_B, CLA_C with CLA_B, and CR_B with CR_C, and then comparison between the two different routes. Since during the low concentration method takes place without any pyrolysis step, and the powders are calcined at 700^{o}C, while the citrate route is more violent due to the pyrolysis step, and the calcination takes place at 850^{o}C.

These factors are important to take in account for the possibility of scaling up one of the fabrication methods. Fabrication of thin films using the low complexation method with HNO_3 and electrochemical characterization of the films, will give a clearer view of the role of HNO_3 during the fabrication of the precursor powder, when they will be compared pellets prepared without HNO_3.

References

[1] E. Barsoukov, J. Ross Mcdonald, *Impedance Spectroscopy, Theory, Experiment and Applications,* 2nd Ed, Wiley, 2005

[2] B. A. Boukamp, B. A. van Hassel, I. C. Vinke, K. J. de Vries, A. J. Burggraaf, *Electrochimica Acta,* **38** (1993) 1817-1825

[3] B. A. Boukamp, *J. Electrochem. Soc.* **142** (1995) 1885-1894

[4] B. A. Boukamp, *Solid State Ionics,* **20** (1986) 31-44

[5] T.S. Zhang, J. Ma, Y.Z. Chen, L.H. Luo, L.B. Kong, S.H. Chan, *Solid State Ionics,* **177** (2006) 1227-1235

[6] Da Yu Wang, A. S. Nowick, *Journal of Solid State Chemistry,* **35** (1980) 325-333

[7] T.S. Zhang, J. Ma, L.H. Luo, S.H. Chan, *Journall of Alloy Compounds,* **422,** (2006) 46-52

[8] Y.-M. Chiang, E.B. Lavik, I Kosacki, H.L Tuller, J.Y. Ying, *Appl. Phys. Lett.* **69** (2), (1996) 185-187

[9] B.C.H. Steele, *Solid State Ionics,* **129** (2000) 95-110

[10] R.Gerhardt-Anderson, *Solid State Ionics,* **5** (1981) 547

[11] C.R. Xia, M.L. Liu, *Solid State Ionics,* **152** (2002) 423-430

[12] A.Giesbers, *M. Sc. Thesis University of Twente*, 2004

[13] William D. Callister, *Material Science and Engineering an Introduction*, 7th Edition, Wiley 2007

A: Pure CGO
B: Addition of 0.5 Fe at % by ball milling
C:Additionof0.5Feat%*"insitu"*

Appendix A-Overview Table

Synthesis	Citrate Route			Complexation Low [C]						Complexation High [C]			
Description	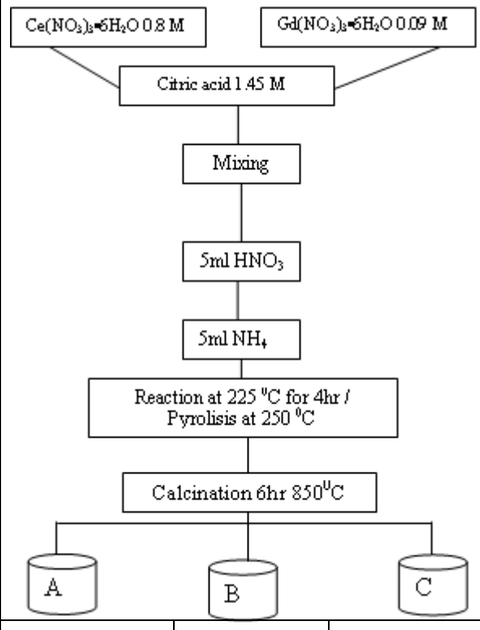			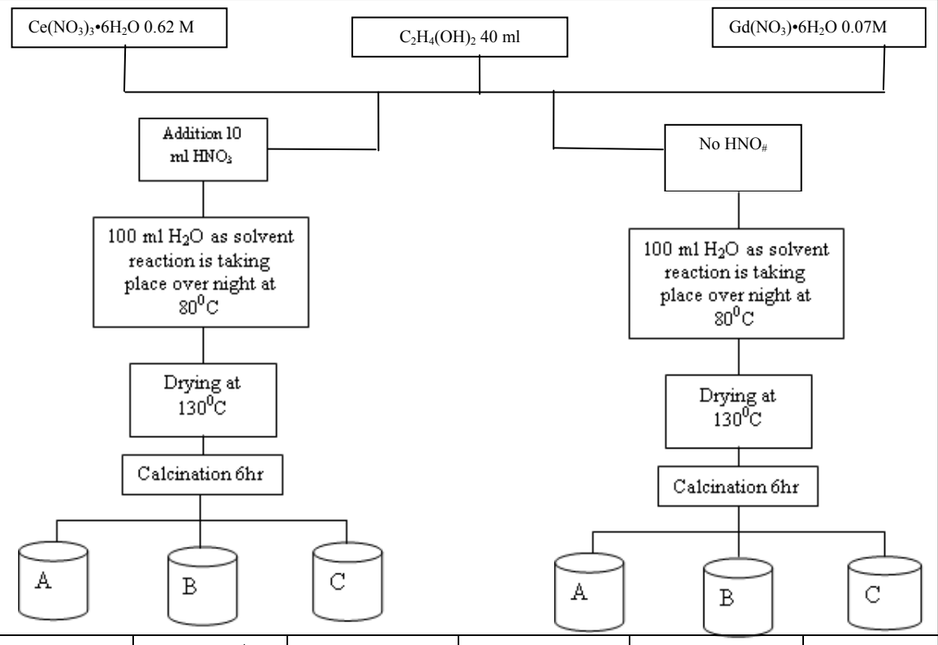						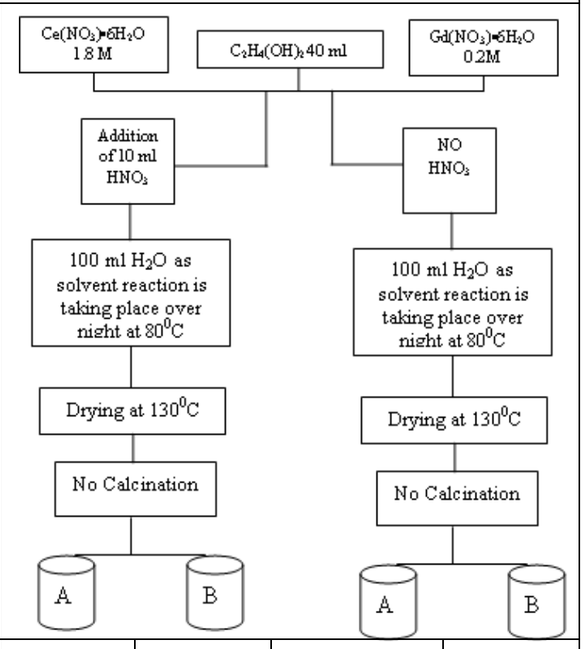	
Characterization													
Name	CR_A	CR_B	CR_C	CLA_A*	CLA_B*	CLA_C	CLN_A	CLN_B	CLN_C	CHA_A	CHA_B	CHN_A	CHN_B
Crystallite size nm	20	20	25	29	6	13	5	5	13	29	30	29	29
Particle size µm	0.5	0.14	0.5	0.5	0.18	0.4	0.2	0.12	0.18	0.5	0.15	0.4	0.3
Sintering **T in ^{0}C**	1500	1200	1200	1300	1200	1200	1300	1200	1100	1300	1200	1500	1200
Sintering **Rel. Density**	95%	97%	98%	100%	100%	100%	95%	94%	97%	97%	99%	94%	94%
Grain Size µm	2.2 µm	0.9 µm	0.46 µm	0.4 µm	0.46 µm	0.45 µm	0.38 µm	<<0.38 µm	<<0.38 µm	0.51 µm	0.81 µm	1.4µm	no sample
E_{total} (kJ/mol)	86.7	74.3	72.7	Cracks no measurement	Cracks no measurement	72.8	72.1	122	73.7	72.6	82.6	105.1	86
σ_{total} (S/cm) at 600^{0}C	6×10^{-3}	8.76×10^{-3}	7.82×10^{-3}	Cracks no measurement	Cracks no measurement	0.014	0.013	2.3×10^{-3}	0.012	0.02	0.016	3.7×10^{-3}	3.17×10^{-3}

* Both CLA_A and CLA_B revealed cracks after sintering

Appendix B-Normalized Impedance Spectra

Citrate Route

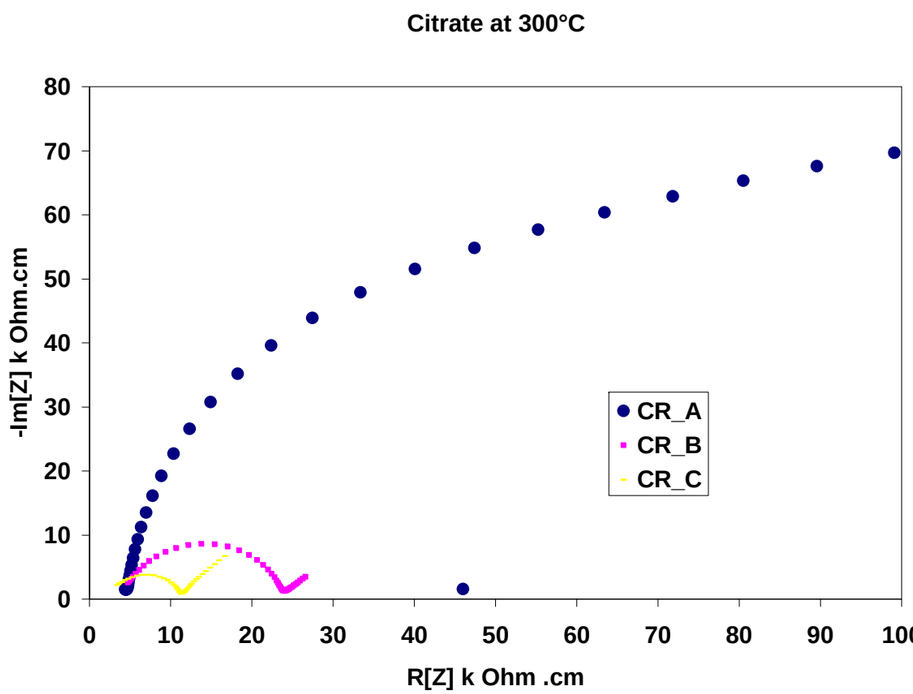

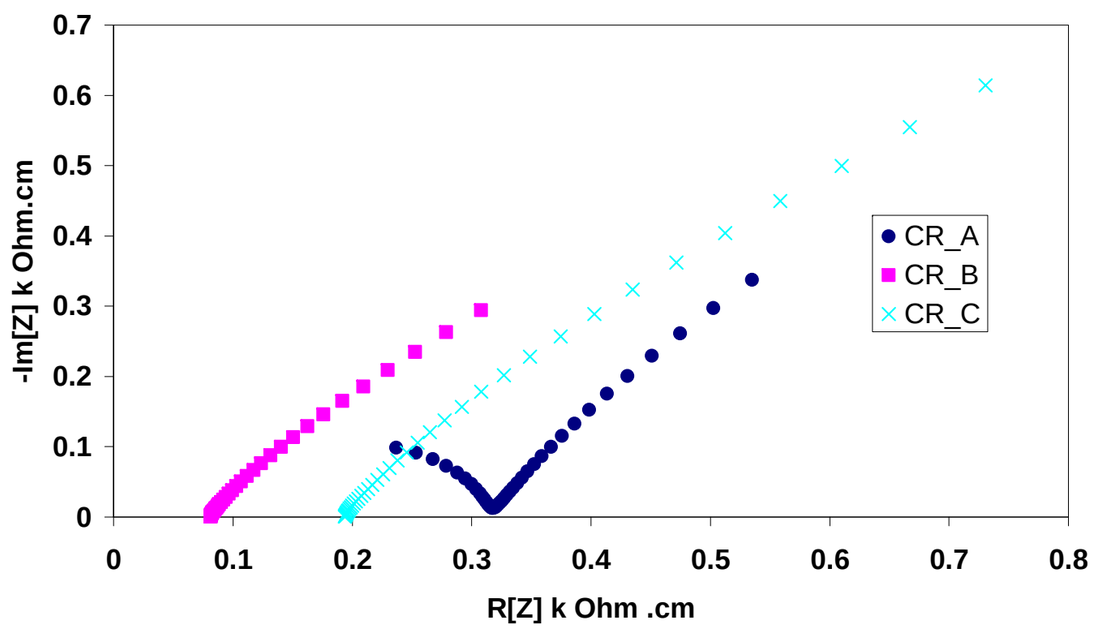

Low Concentration Complexation

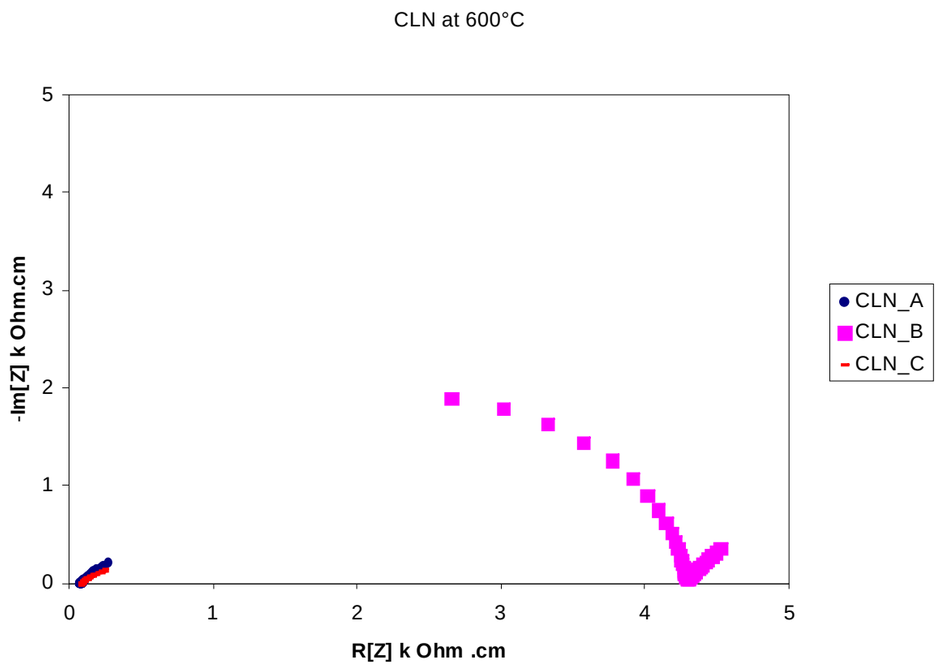

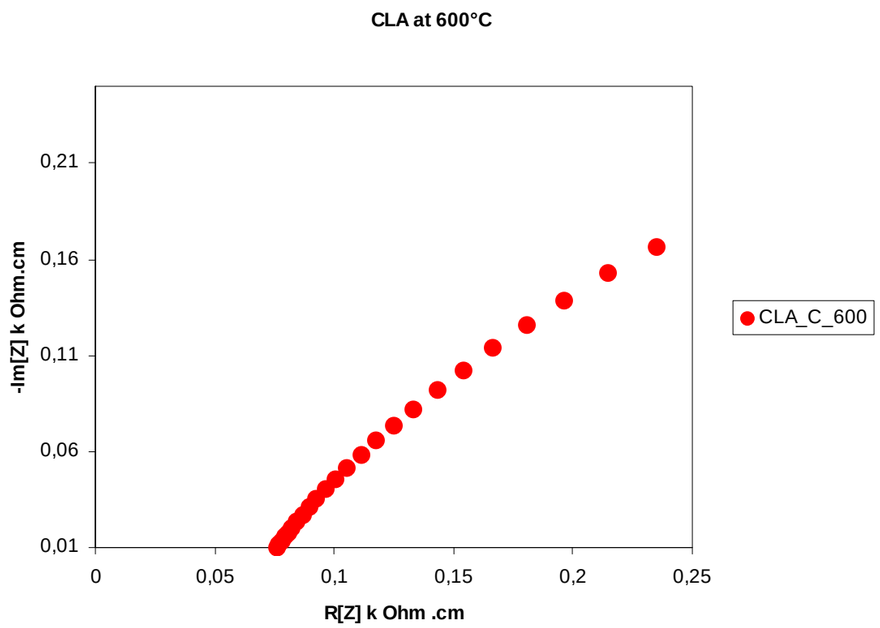

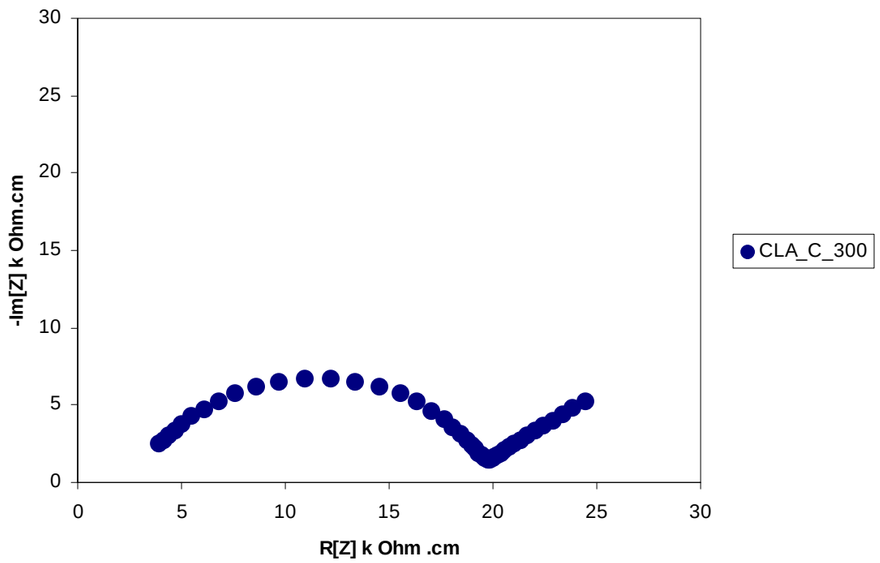

High Concentration Complexation

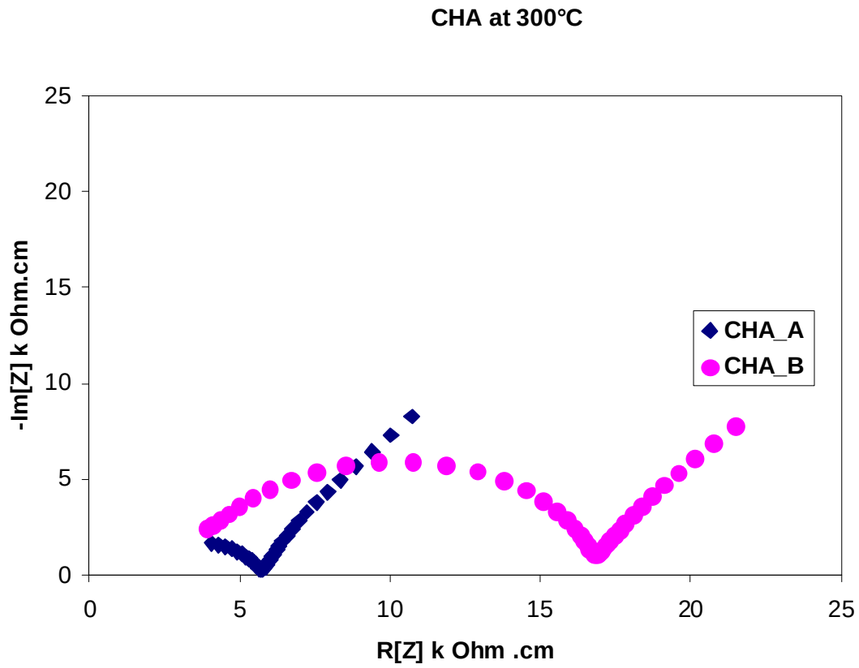

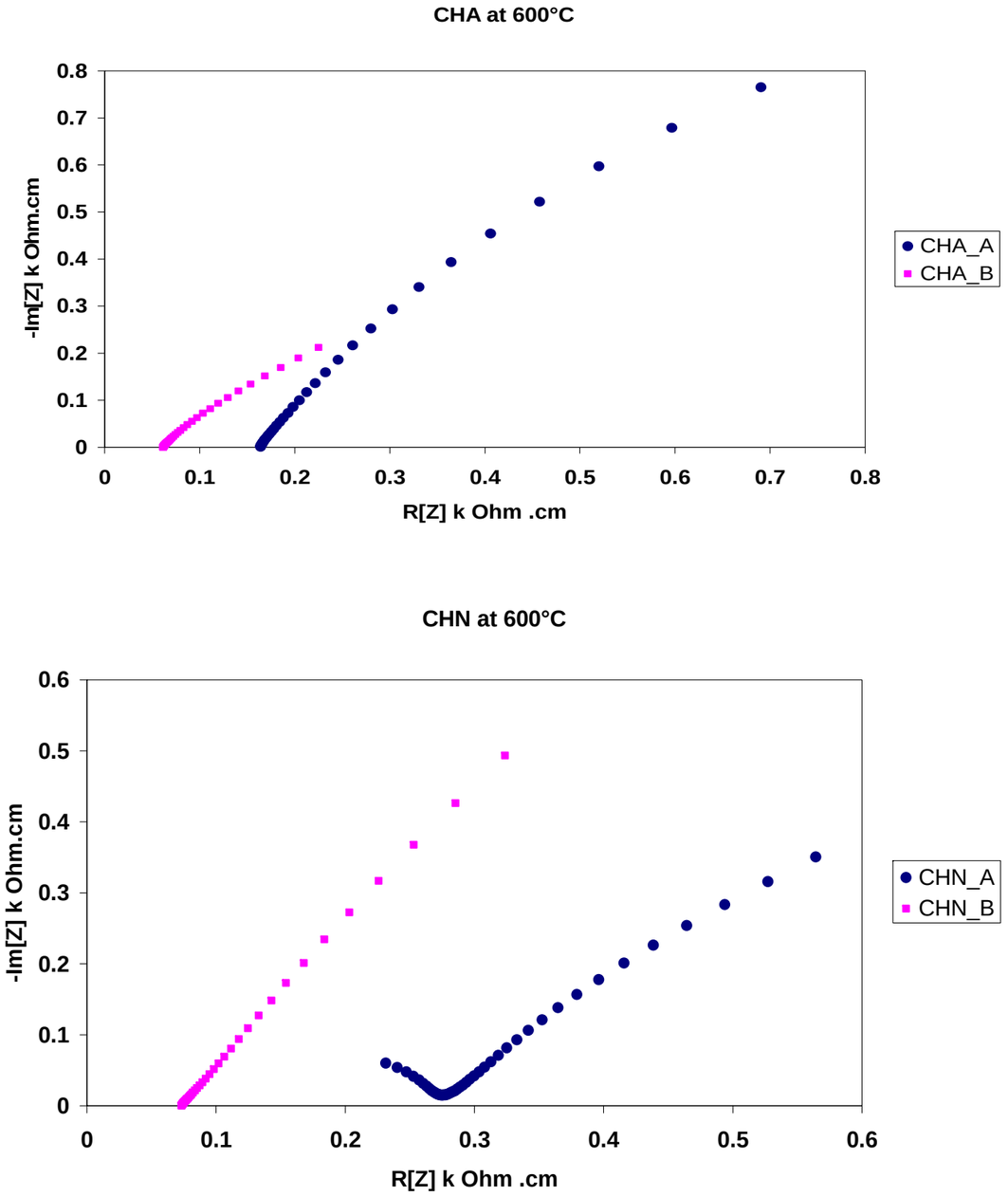

Appendix C

Citrate Route

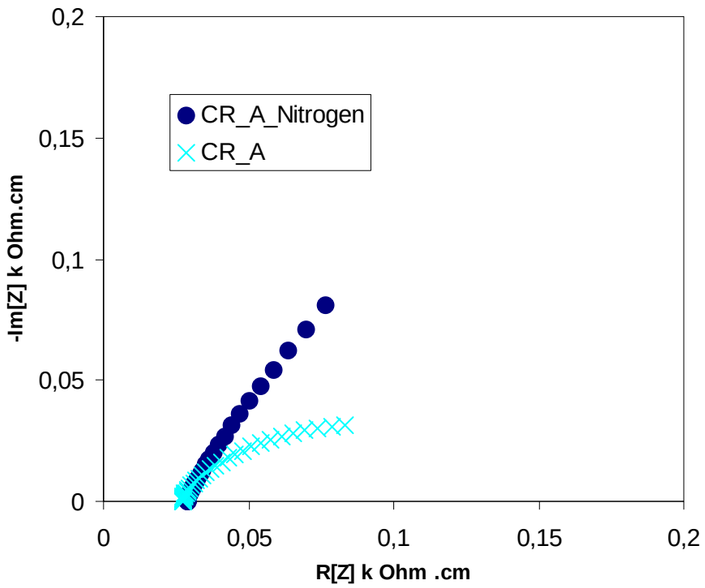

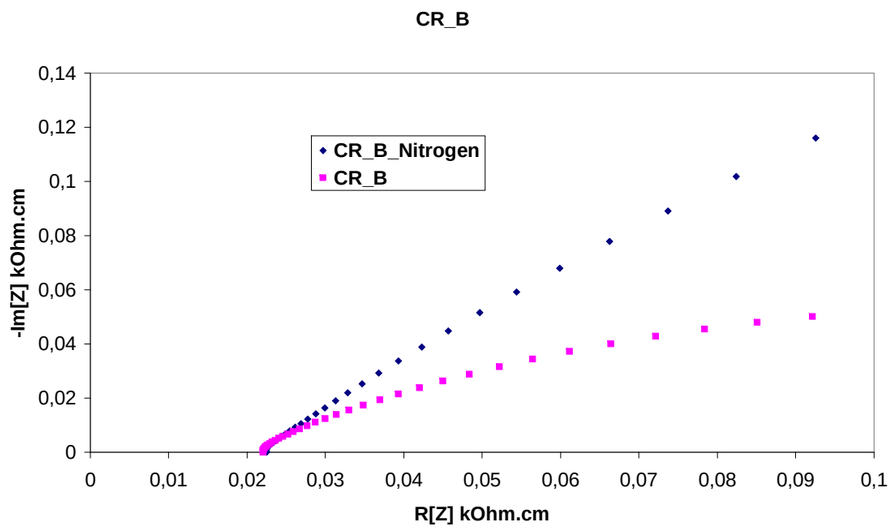

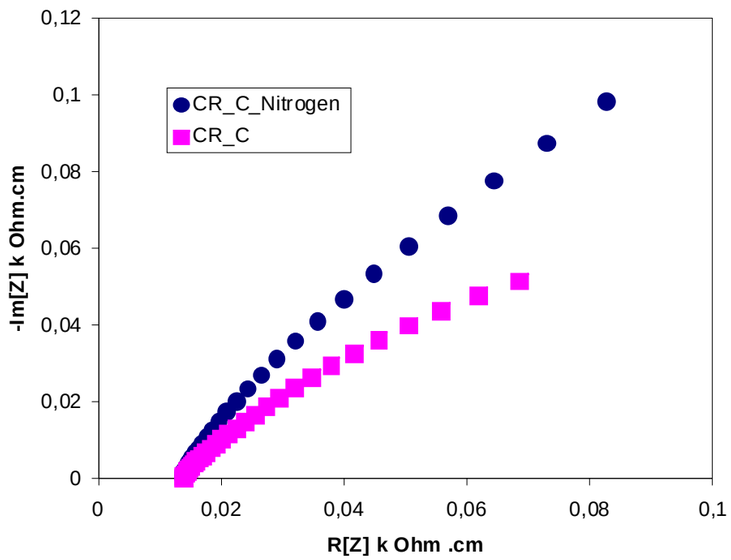

Complexation Low Concentration Addition of HNO_3

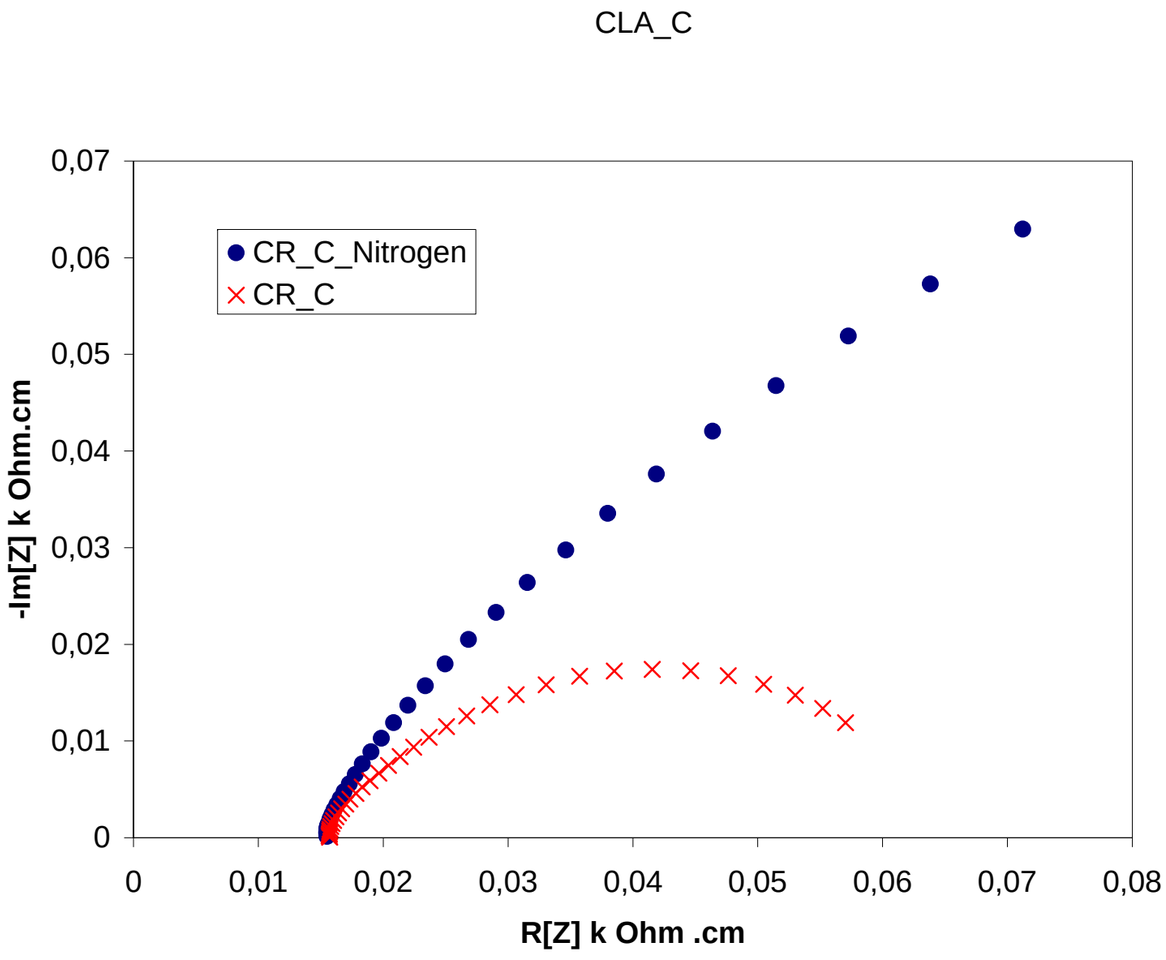

Complexation Low Concentration Without HNO_3

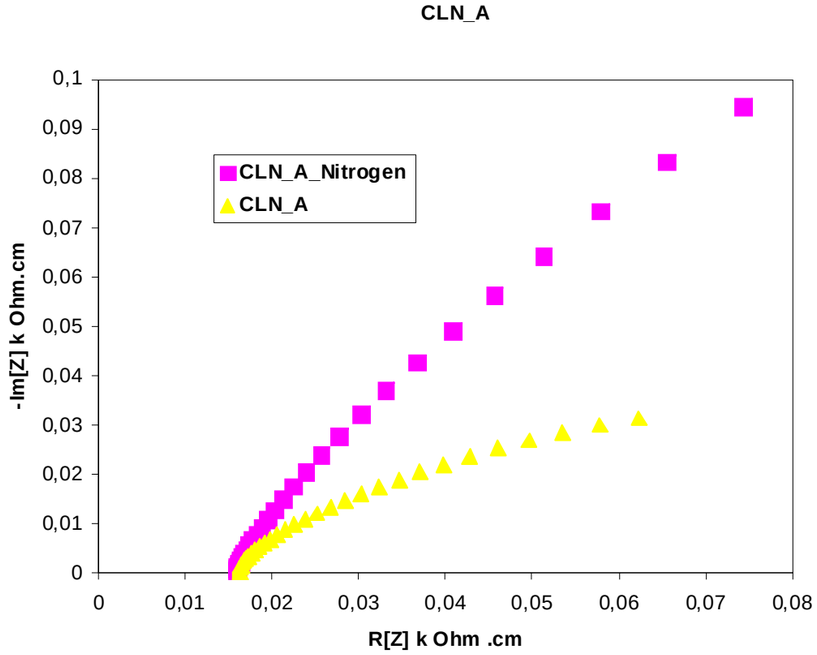

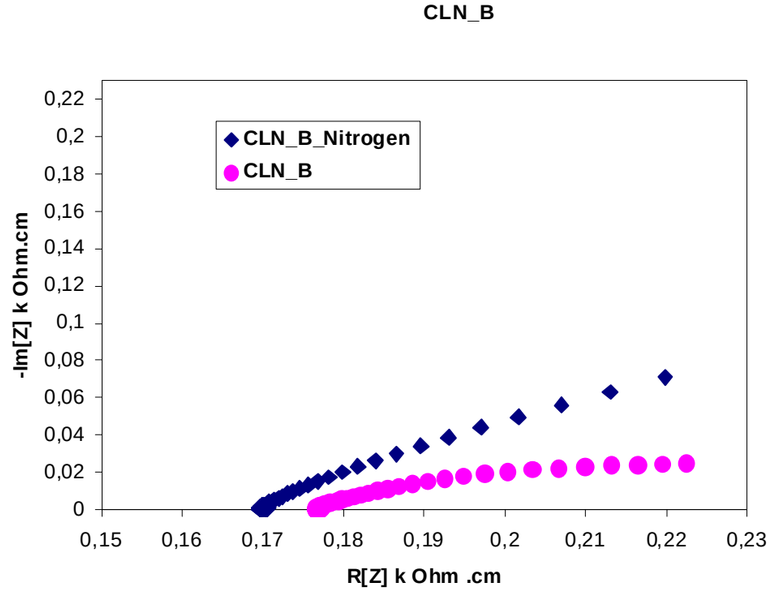

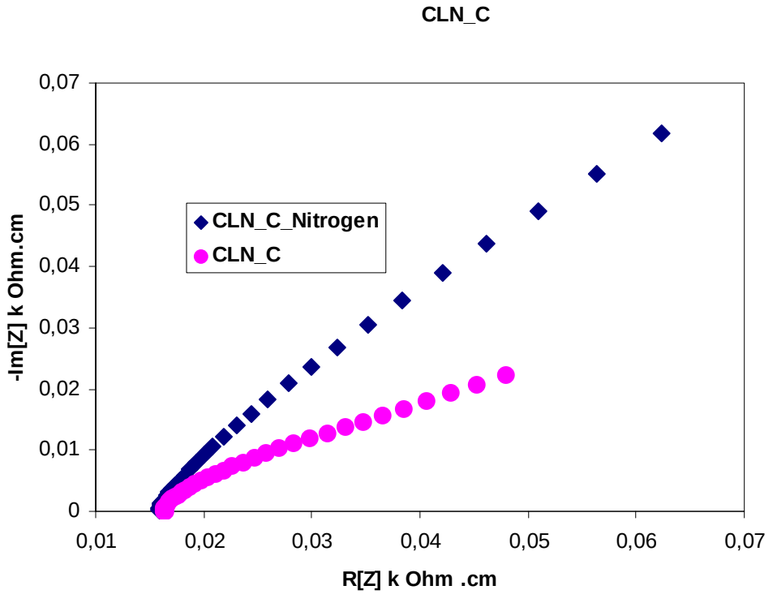

Complexation High Concentration Addition of HNO_3

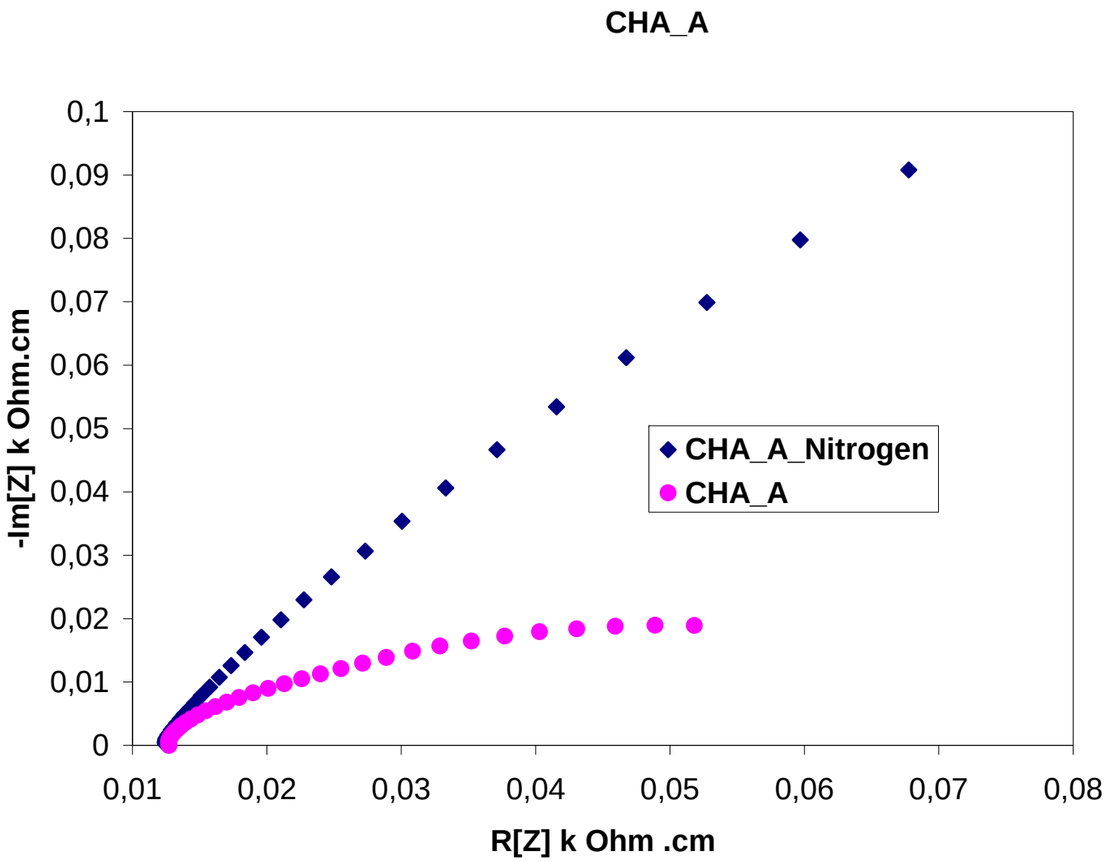

Complexation High Concentration Without HNO_3

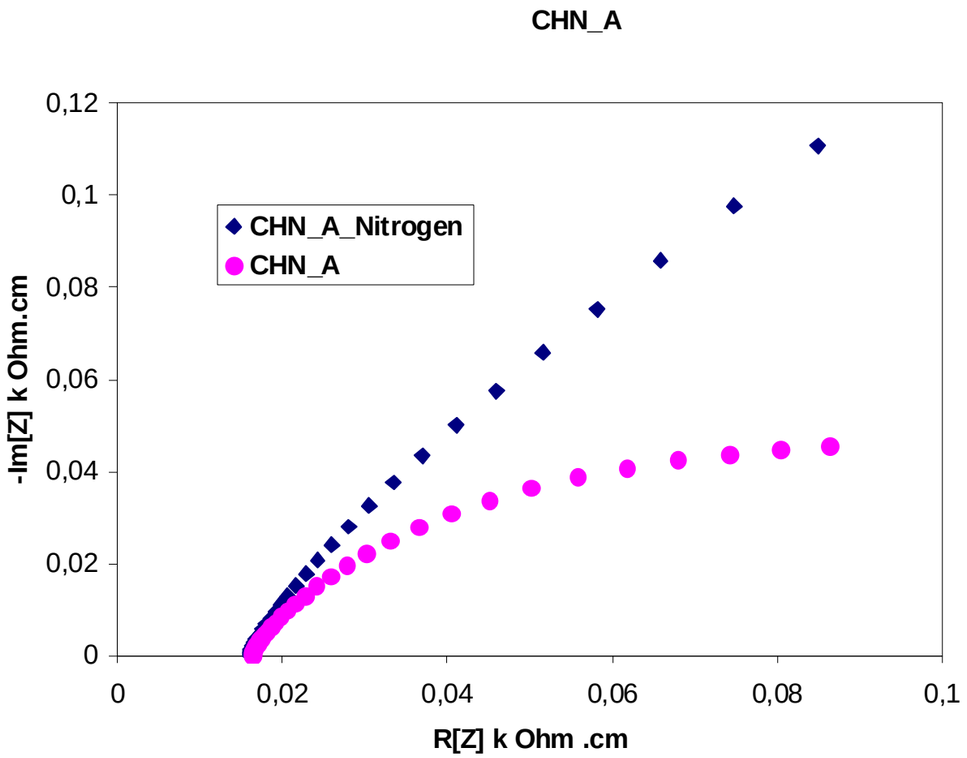

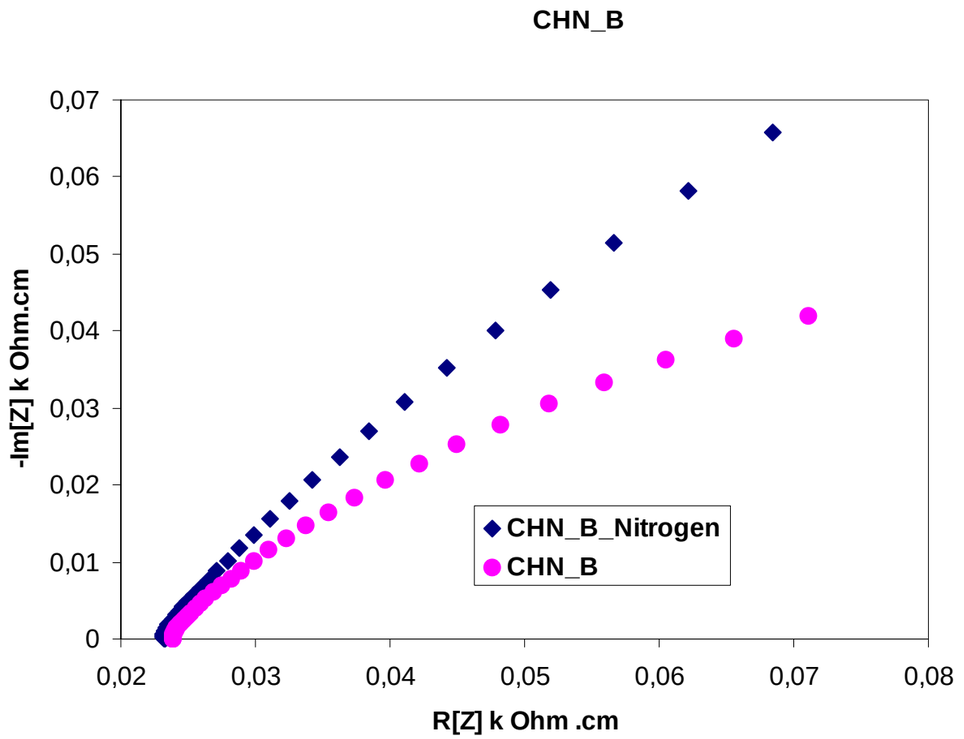

Acknowledgments

At the end of this thesis I would like to acknowledge all the people who where by my side all this years during my stay in The Netherlands.

Primarily I would like to thank Dr. Bernard Boukamp for his supervision during my master thesis work and as a mentor during my studies. Additionally I would like to thank Professor Dave Blank for hosting me in his research group. Of course I can not forget the help and the useful remarks of Dr. Louis Winnubst during my research. Last but not least with the respect to the scientific committee of my research, I would like to thank my co-supervisor M.Sc. Nicolas Hildenbrand for his daily support and encouragement when everything seemed impossible.

Additionally I would like to thank my supervisors in Greece Dr. G. Marnellos and Dr. C. Athanasiou for encouraging me to pursue a master's degree in the Netherlands. I would also like to thank Mr. Rik Akse for his help and support in all practical and administration problems that I faced.

Apart from the scientific aspect of my studies there is the other aspect the everyday life aspect, which is the boost for a clear mind. In that manner I would like to thank all my friends in Enschede (Hichem, Paul, Didem, Semih, Jon) for making my stay as pleasant as possible. My friends in Greece (Nikos, George, Jimakos, Manos, Popi, Elena) for the endless talks through skype and support. Of course I would like to thank my office mates (Xin, Indu, Luc, Gerard) for standing me, and especially Gerard for his joyful conversations.

Last but not least I would like to thank my Uncle George and my family; mother and sister, the women of my life. Without their help, support, and of course love definitely I would not write these lines today, *Σας αγαπώ!*

Vasilis